Precision Mechanical Rotation Sensors for
Terrestrial Gravitational Wave Observatories

M.P. Ross

A dissertation
submitted in partial fulfillment of the
requirements for the degree of

Doctor of Philosophy

University of Washington

2020

Reading Committee:

Jens Gundlach, Chair

Eric Adelberger

Sanjay Reddy

Program Authorized to Offer Degree:
Physics

University of Washington

Abstract

Precision Mechanical Rotation Sensors for Terrestrial Gravitational Wave Observatories

M.P. Ross

Chair of the Supervisory Committee:
Professor Jens Gundlach
Physics

The LIGO gravitational-wave observatories are comprised of 4-km long dual-recycled Fabry-Perot Michelson interferometers. Each observatory deploys a multi-stage seismic isolation system to isolate from terrestrial seismic motion. These systems use seismometers to measure motion at a wide range of frequencies.

Seismometers are inherently susceptible to contamination due to tilts arising from wind acting on the walls of the observatory. This contamination dominates seismometer readings at low frequency which limits the performance of LIGO's seismic isolation. We developed low-frequency inertial rotation sensors to subtract this tilt-contamination from ground seismometers. These sensors were deployed at both LIGO observatories which allowed the observatories to operate during high wind speeds.

In addition, a compact inertial rotation sensor was developed with the capability of being deployed on the LIGO seismic isolation platforms. A prototype was built and tested. A theoretical control model was designed to exploit this novel sensor. This model predicts a significant decrease in control-noise leakage in the gravitational wave frequency band.

These sensors have found application in a number of auxiliary fields. The ground rotation sensors have allowed for novel seismological studies while the compact rotation sensor has been applied to the study of Newtonian noise.

TABLE OF CONTENTS

LIST OF FIGURES

LIST OF TABLES

DEDICATION

To my wife, Grace

without her love and support

this work would not have been possible

ACKNOWLEDGMENTS

The list of people who influenced this research could fill volumes. I would particularly like to thank: the entire Eöt-Wash group for their many contributions, especially Charlie Hagedorn for the countless conversations and mentorship; Jim Warner, Hugh Radkins, Arnaud Pele, and Eyal Schwartz for caring for our temperamental devices; the LIGO seismic team for constructing and maintaining beautiful seismic isolation systems, especially Brian Lantz and Jeff Kissel for their insightful inputs and coordination; the entire LIGO scientific collaboration for its welcoming culture and intellectual prowess; the CENPA community for making tough work enjoyable; the CENPA machine shop for the precise machining even when our schematics were subpar; my mom, Sharon Powers, for instilling in me a reverence for Nature; the many professors and teachers that steered me towards physics, especially C.D. Hoyle, Erik Kramer, and Steve Hoffman; Pippin, Bjorn, Olive, and Toph for their constant distractions and companionship; and, again, my amazing wife, Grace Rotwein, for the love and support throughout my years of study and travel including my extended trips to the deserts of Washington and the swamps of Louisiana.

Much of the work presented here is open-source. The BRS image analysis software can be found here: `https://github.com/mpross/BRSReadout`. The BRS controls software can be found here: `https://github.com/mpross/BRS-Controls`. The CAD models of the BRS can be found here: `https://github.com/mpross/BRS-Schematics`. The CAD model of the autocollimator can be found here: `https://github.com/mpross/Autocollimator-Schematics`.

The CAD models of the cBRS can be found here: `https://github.com/mpross/cBRS-Schematics`. The readout and controls software for the cBRS can be found here: `https://github.com/mpross/cBRS_Controls`.

The first observation showed ... that owing to the extreme sensitiveness of the instrument to vibrations, the work could not be carried on during the day. The experiment was next tried at night. ... so extraordinarily sensitive was the instrument that the stamping of the pavement, about 100 meters from the observatory, made the fringes disappear entirely!
If this was the case with the instrument constructed with a view to avoid sensitiveness, what may we not expect from one made as sensitive as possible!

Albert A. Michelson
"The Relative Motion of the Earth and the Luminiferous Ether"

Chapter 1

INTRODUCTION

1.1 Gravitational Wave Theory

1.1.1 Linearized General Relativity

In the early twentieth century, the theory of General Relativity supplanted the static space-time, in which all prior physics was formulated, with a deformable space-time yielding a geometric explanation for gravity. This space-time is described by a unitless tensor field, $g_{\mu\nu}$, called the metric. The deformation of this metric follows the Einstein equation [1]:

$$R_{\mu\nu} - \frac{1}{2}R\, g_{\mu\nu} + \Lambda g_{\mu\nu} = \frac{8\pi G}{c^4}T_{\mu\nu} \tag{1.1}$$

where $R_{\mu\nu}$ is the Riemann tensor, R is the Ricci scalar, Λ is the cosmological constant, G is the gravitational constant, c is the speed of light, and $T_{\mu\nu}$ is the stress energy tensor.

If one focuses on a locally-flat region of space which is much smaller than the scale of the universe, then the cosmological constant term is negligible and the metric can be approximated via [2]:

$$g_{\mu\nu}(\vec{x},t) \approx \eta_{\mu\nu}(\vec{x},t) + h_{\mu\nu}(\vec{x},t) \tag{1.2}$$

where $\eta_{\mu\nu}$ is the flat Minkowski metric and $h_{\mu\nu}$ is a small perturbation[1], $|h_{\mu\nu}| \ll 1$. Applying the Einstein equation and transferring to a transverse-traceless coordinate system yields the wave equation [4]:

$$\Box h_{\mu\nu} = -\frac{16\pi G}{c^4}T_{\mu\nu} \tag{1.3}$$

For a complete derivation see Reference [2]. Vacuum solutions propagating along the

---

[1]The largest amplitude of gravitational wave strain measured thus far is on the order of $|h_{\mu\nu}| \approx 10^{-21}$[3]

z-axis can readily be found as:

$$h_{ij}(\vec{x}, t) = \begin{pmatrix} h_+ & h_\times & 0 \\ h_\times & -h_+ & 0 \\ 0 & 0 & 0 \end{pmatrix} cos(\omega t - \kappa z) \tag{1.4}$$

where h_+ and $h_\times$ are the amplitudes in the "plus" and "cross" polarizations[2], ω is the angular frequency of oscillation, and κ is the wavenumber. Here i and j run from 1 to 3 and correspond to the the three spatial coordinates. The time components are suppressed as the $h_{0\nu}$ components are zero due the coordinate choice and h_{00} is zero outside the source.

In the long wavelength limit, a source of gravitational waves (GW) can be decomposed into a sum of momenta of the stress-energy tensor:

$$h_{ij}(\vec{x}, t) = \frac{1}{r}\frac{4G}{c^4}\Lambda_{ij,kl}\left(S^{kl} + \frac{1}{c}n_m\dot{S}^{kl,m} + \frac{1}{2c^2}n_m n_p \ddot{S}^{kl,mp} + ...\right)_{\text{ret}} \tag{1.5}$$

where $\Lambda_{ij,kl}$ is the projection from the source frame to transverse-traceless coordinates and the momenta are defined as:

$$S^{ij}(t) = \int T^{ij}(t, \mathbf{x})d^3x \tag{1.6}$$

$$S^{ij,k}(t) = \int T^{ij}(t, \mathbf{x})x^k d^3x \tag{1.7}$$

$$S^{ij,kl}(t) = \int T^{ij}(t, \mathbf{x})x^k x^l d^3x \tag{1.8}$$

with the subscript "ret" denoting the evaluation at retarded time. The leading term of Equation 1.5 can be expressed in terms of the mass quadrupole moment of the source, Q_{ij}, as:

$$h_{ij}(\vec{x}, t) = \frac{1}{r}\frac{2G}{c^4}\ddot{Q}_{ij}(t - r/c) \tag{1.9}$$

---

[2]A massless graviton is assumed. A massive graviton would yield five polarizations instead of two. Current graviton mass constraints are $m_g \leq 4.7 \times 10^{-23} eV/c^2$ [5]

Thus the emission of gravitational waves is primarily driven by time varying quadrople moments. Varying higher order moments will also emit gravitational waves but are subdominant in most natural systems. [3]

1.1.2 Compact Binary Coalescence

As of writing, the only systems that have been observed to emit gravitational waves are composed of two compact[4] astrophysical objects orbiting a common center of mass, so-called compact binaries. These objects could be neutron stars, as with the Hulse-Taylor binary pulsar [7], GW170817 [8], and GW190425 [9], or black holes like GW150914 [3] and most events in the GWTC-1 [10].

Such a system can be approximated as two point masses, $m_{1,2}$, in a Keplerian orbit which decays due to the emission of gravitational waves. This approximation is only valid during the inspiral phase of the merger when the distance between the two objects is much larger than the size of the objects. For a complete simulation of the gravitational wave emission during a merger, one must numerically compute the evolution of the space-time around the objects. [11]

The gravitational waves emitted under the point-mass approximation follow:

$$h_+(t) = \frac{4}{r}\left(\frac{GM_c}{c^2}\right)^{5/3}\left(\frac{\pi f}{c}\right)^{2/3}\frac{1+\cos^2\theta}{2} \ \cos(\omega t + \phi) \tag{1.10}$$

$$h_\times(t) = \frac{4}{r}\left(\frac{GM_c}{c^2}\right)^{5/3}\left(\frac{\pi f}{c}\right)^{2/3}\cos\theta \ \sin(\omega t + \phi) \tag{1.11}$$

where $M_c = (m_1 m_2)^{3/5}/(m_1 + m_2)^{1/5}$ is the "chirp mass", r is the distance from the observer to the center of mass of the source, θ is the viewing angle with respect to the axis of the

---

[3]GW190412 [6], a high mass-ratio binary system, is the only observation to contain contributions from higher moments.

[4]Compactness signifies that the object is much more dense than ordinary stellar matter. The compactness of the objects is of importance only to satisfy a point-mass approximation and to allow observation in current instruments. Non-compact objects will emit gravitational waves in their inspiral phase but merge long before entering the frequency band accessible today.

orbital plane, $f = \omega/2\pi$ is the frequency of oscillation, and ϕ is the initial phase of the system.

The emission of gravitational waves carry energy away from the system and thus the orbit must decay. As the radius of the orbit decreases, the frequency of oscillation must grow due to Kepler's law. This then causes the amplitude of the emitted gravitational waves to grow and the decay of the orbit to quicken. The frequency change during this runaway process follows:

$$\dot{f} = \frac{96}{5}\pi^{8/3}\left(\frac{GM_c}{c^3}\right)^{5/3}f^{11/3} \tag{1.12}$$

This process produces a characteristic "chirp" signal which begins at low frequency and low amplitude then grows in amplitude while shifting to higher frequency. The signal culminates in a final sharp increase in both frequency and amplitude before the objects merge. This can be seen in Figure 1.1 which shows a spectrogram of the observed strain at the LIGO observatories of the binary neutron star merger GW170817 [8].

Although binary systems are the topic of choice here, many other systems should theoretically emit gravitational waves. These can range from asymmetric spinning stars [12] and supernovae [13] to cosmic strings [14] and density perturbations in the early universe [15]. With the measurement of gravitational waves, humankind has technologically expanded our senses to include the faint vibrations of space-time. This ability has allowed the study of new types of astronomical systems and may one day allow further insight into the beginning of the universe and the nature of gravity.
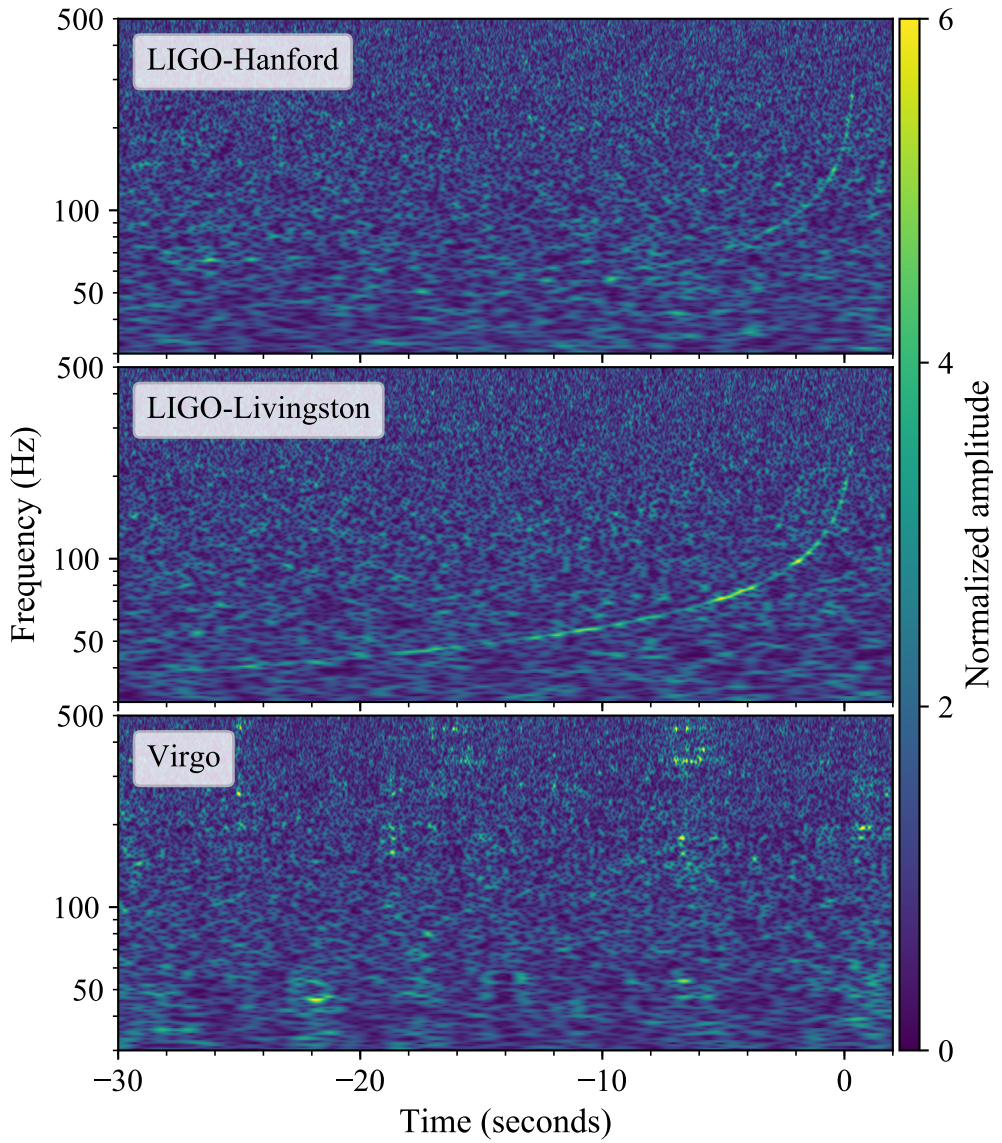
Figure 1.1: Spectrogram of the strain caused by a binary neutron star merger as seen at the LIGO Hanford Observatory, LIGO Livingston Observatory, and the Virgo Observatory [19]. A clear chirp signal can be seen starting at ~40 Hz which rises in both frequency and amplitude. The origin of the time axis is the time at which the neutron stars merge. The differing amount of signal in the three detectors is due to the alignment of their respective antenna-patterns with the source location. Reprinted from [8].

1.2 LIGO

1.2.1 Sensitivity

The Laser Interferometer Gravitational-wave Observatory (LIGO) [16] is a pair of 4-km-long L-shaped interferometric gravitational wave detectors, one located in Hanford, Washington (LHO) and the other in Livingston, Louisiana (LLO). Each observatory is a dual-recycled Fabry-Perot Michelson interferometer, shown in Figure 1.2, which measures the differential strain between its two arms formed by pairs of partially reflective mirrors, also called test masses.

Each test mass is housed in its own building (end station) while the rest of the optics are held in another building (corner station). The end stations are connected to the corner station by orthogonal 4-km-long vacuum tubes to form the "X-arm" and "Y-arm" of the interferometer. This lends a convenient coordinate system, used throughout, with the x-axis running along one arm, the y-axis along the other, and the z-axis along local vertical.

As a gravitational wave passes the observatory, the arms experience strains that follow [2]:

$$h_{xx} = h_+ \left(\cos^2 \theta \ \cos^2 \phi - \sin^2 \phi \right) + 2 \ h_\times \ \cos \theta \ \sin \phi \cos \phi \qquad (1.13)$$

$$h_{yy} = h_+ \left(\cos^2 \theta \ \sin^2 \phi - \cos^2 \phi \right) - 2 \ h_\times \ \cos \theta \ \sin \phi \cos \phi \qquad (1.14)$$

$$h = \frac{1}{2} \left(h_{xx} - h_{yy} \right) = \frac{1}{2} h_+ \left(1 + \cos^2 \theta \right) + h_\times \ \cos \theta \ \sin 2\phi \qquad (1.15)$$

where h_{xx} and h_{yy} are the strains along the x and y arms respectively, θ and ϕ are the polar and azimuthal angles of the direction of propopation, and h is the differential strain measured by the observatory. Here the polarizations are defined in the source frame.

The series of optics allows the observatory to measure differential strains down to 5×10^{-24} at 200 Hz. Noise curves for the observatories are shown in Figure 1.3 where one can see that the sensitive band of the observatory runs from 20 Hz up to 7 kHz. At low frequencies the noise is dominated by residual control noise, discussed in Section 3.1, while at high it is
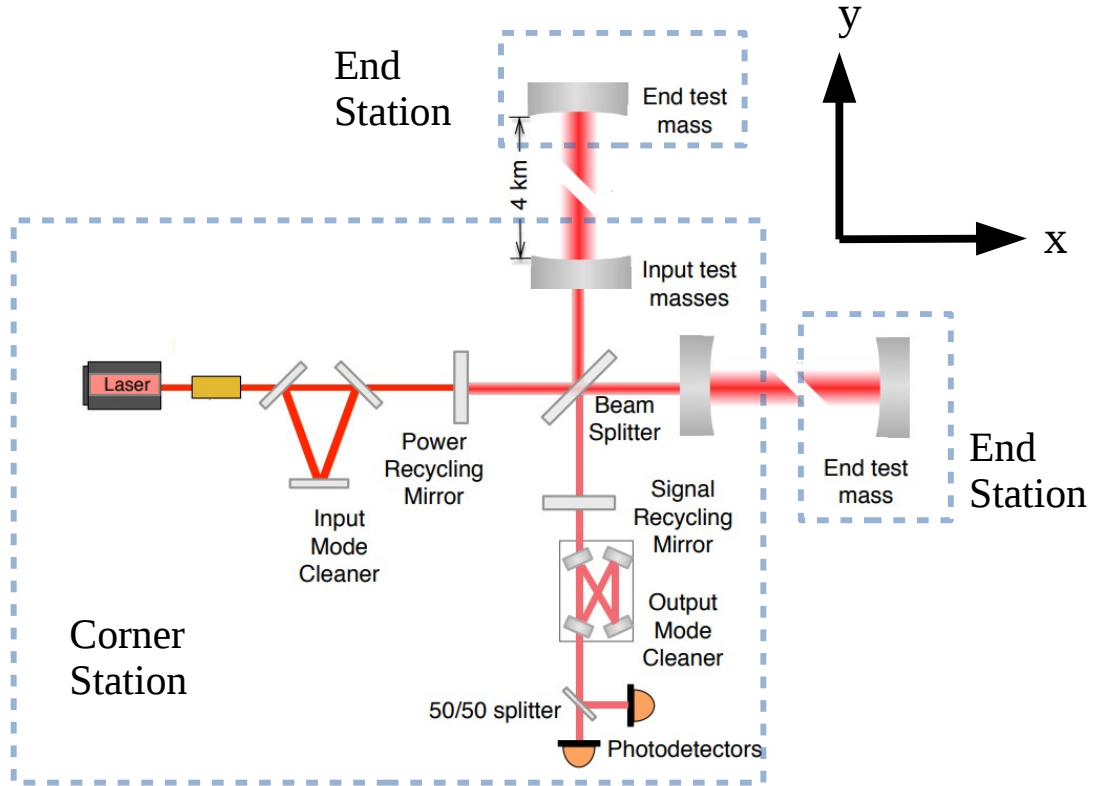
Figure 1.2: Optical layout of the LIGO interferometers. Each test mass is housed in its own building (End Station) while the rest of the optics are held in another building (Corner Station). Adapted from [17]. Copyright 2016 by the American Physical Society.

dominated by noise caused by quantum fluctuations. [21]

1.2.2 Events

With LIGO's current sensitivity, the primary systems of interest are compact binaries, discussed in Section 1.1.2, which merge within the band of interest. A equal mass 50 $M_\odot$ binary black hole system would merge at ∼22 Hz while a 1.4 $M_\odot$ binary neutron star system merges
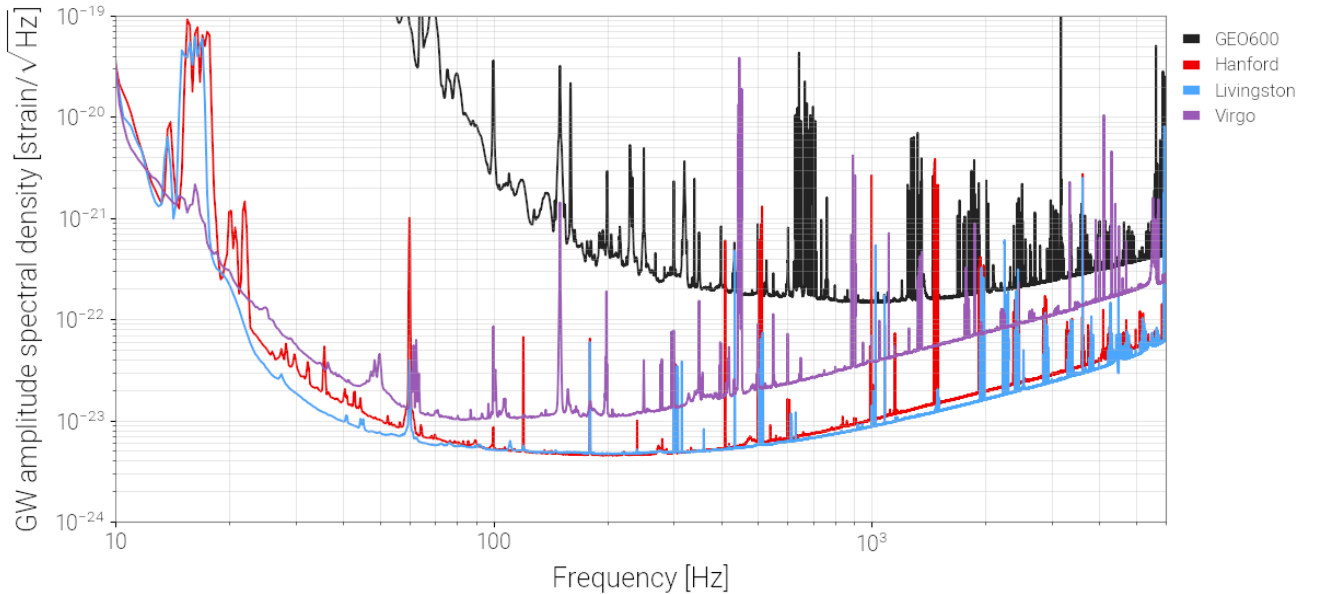
Figure 1.3: Differential strain sensitivity of the LIGO Observatories during the third observing run. [16] Also shown are the sensitivities of the Virgo [19] and GEO600 [20] observatories. Reprinted from [18].

at ~800 Hz yet emits appreciably while sweeping through the LIGO band.

During the first and second observing runs of LIGO, ten binary black hole systems and one binary neutron star merger were detected with high significance. [10] The black hole binaries ranged in total mass from 18.6 $M_\odot$ to 84.4 $M_\odot$ and merged at distances from 320 Mpc to 2.8 Gpc. The neutron star binary had component-masses of 1.27 $M_\odot$ and 1.46 $M_\odot$ and merged at 40 Mpc. These systems are tabulated in Table 1.1.

The recently completed third observing run has had 56 significant candidates. [22] Although most of these candidates have not been verified to be true gravitational wave events, they show a significant increase in rate of detection due to both the decreased noise and increased duty cycle achieved for the third observing run. Two of these candidates have been confirmed to be true gravitational wave events: GW190412 [6] a binary black hole merger

Event Name	m_1 $(M_\odot)$	m_2 $(M_\odot)$	M_f $(M_\odot)$	d (Mpc)	z
GW150914	$35.6^{+4.7}_{-3.1}$	$30.6^{+3.0}_{-4.4}$	$63.1^{+3.4}_{-3.0}$	440^{+150}_{-170}	$0.09^{+0.03}_{-0.03}$
GW151012	$23.2^{+14.9}_{-5.5}$	$13.6^{+4.1}_{-4.8}$	$35.6^{+10.8}_{-3.8}$	1080^{+550}_{-490}	$0.21^{+0.09}_{-0.09}$
GW151226	$13.7^{+8.8}_{-3.2}$	$7.7^{+2.2}_{-2.5}$	$20.5^{+6.4}_{-1.5}$	450^{+180}_{-190}	$0.09^{+0.04}_{-0.04}$
GW170104	$30.8^{+7.3}_{-5.6}$	$20.0^{+4.9}_{-4.6}$	$48.9^{+5.1}_{-4.0}$	990^{+440}_{-430}	$0.20^{+0.08}_{-0.08}$
GW170608	$11.0^{+5.5}_{-1.7}$	$7.6^{+1.4}_{-2.2}$	$17.8^{+3.4}_{-0.7}$	320^{+120}_{-110}	$0.07^{+0.02}_{-0.02}$
GW170729	$50.2^{+16.2}_{-10.2}$	$34.0^{+9.1}_{-11.1}$	$79.5^{+14.7}_{-10.2}$	2840^{+1400}_{-1360}	$0.49^{+0.19}_{-0.21}$
GW170809	$35.0^{+8.3}_{-5.9}$	$23.8^{+5.1}_{-5.2}$	$56.3^{+5.2}_{-3.8}$	1030^{+320}_{-390}	$0.20^{+0.05}_{-0.07}$
GW170814	$30.6^{+5.6}_{-3.0}$	$25.2^{+2.8}_{-4.0}$	$53.2^{+3.2}_{-2.4}$	600^{+150}_{-220}	$0.12^{+0.03}_{-0.04}$
GW170817	$1.46^{+0.12}_{-0.10}$	$1.27^{+0.09}_{-0.09}$	≤ 2.8	40^{+7}_{-15}	$0.01^{+0.00}_{-0.00}$
GW170818	$35.4^{+7.5}_{-4.7}$	$26.7^{+4.3}_{-5.2}$	$59.4^{+4.9}_{-4.8}$	1060^{+420}_{-380}	$0.21^{+0.07}_{-0.07}$
GW170823	$39.5^{+11.2}_{-6.7}$	$29.0^{+6.7}_{-7.8}$	$65.4^{+10.1}_{-7.4}$	1940^{+970}_{-900}	$0.35^{+0.15}_{-0.15}$
GW190412	$29.7^{+5.0}_{-5.3}$	$8.4^{+1.7}_{-1.0}$	$37.0^{+4.1}_{-3.9}$	730^{+140}_{-170}	$0.15^{+0.03}_{-0.03}$
GW190425	$1.60 - 1.87$	$1.46 - 1.69$	$3.4^{+0.3}_{-0.1}$	159^{+69}_{-71}	$0.03^{+0.01}_{-0.02}$

Table 1.1: Confirmed gravitational wave events along with the parameters of each system where m_1 and m_2 are the primary and secondary component masses, M_f is the mass of the post merger object, d is the distance to the system, and z is the cosmological redshift of the system.

with asymmetric component-masses and GW190425 [9] a binary merger with total mass of ~ 3.4 $M_\odot$

Observation of gravitational waves has led to further understanding of a variety of phenomena including the nature of the neutron star composition [23], the source of heavy elements [24], and black hole populations [10]. Additionally, they have allowed model independent measurements of Hubble's constant [25, 26] and have set restrictive constraints on alternative theories of gravity [27].

1.3   Seismic Isolation

1.3.1   LIGO Isolation Scheme

To operate interferometric observatories that are sensitive to the strains of space-time, one must isolate the instrument from all other sources of differential displacement. As the observatories are located on the surface of the earth, the dominant source of such noise is ambient seismic motion.

The ambient seismic wave-field, measurements of which are shown in Figure 1.4, is continuously excited across a wide frequency range. Between 50 mHz and 1 Hz the ambient spectrum is dominated by the "microseism", an always-present feature sourced by the Earth's oceans. [28] Above 1 Hz, the dominant source of seismic motion at the observatories is due to local activity. Yet, even in locations without anthropogenic sources the ground moves at these frequencies. Without isolation, this motion would dominate any measurements with the interferometer and, more practically, would disrupt any attempt to operate the interferometer at its ideal alignment. This ideal alignment is referred to as having the interferometer "locked".

The LIGO observatories solve this issue by employing a multi-stage seismic isolation system formed of both passive and active stages, shown in Figure 1.5. [29] First from the ground is the Hydraulic External Pre-Isolation (HEPI) system which is formed by four hydraulic actuators. This provides a factor of $\sim$100 isolation at high frequencies and allows for correction of tidal effects. Suspended from this is the Internal Seismic Isolation (ISI) system[5], described in Section 1.3.2. The ISI is a dual-stage six-degree active isolation system and is the primary broad-band isolation. From the second stage of the ISI is hung a quadruple pendulum, at the bottom of which is a test mass. This pendulum provides high frequency passive isolation that attenuates the motion of the test mass by $1/f^8$, where f is the frequency of the motion.

---

[5]LIGO employs two versions of the ISI: the HAM-ISI for the auxiliary optics and the BSC-ISI for the core optics. Here ISI refers to the BSC-ISI as rotation sensors have only been deployed on BSC-ISIs.
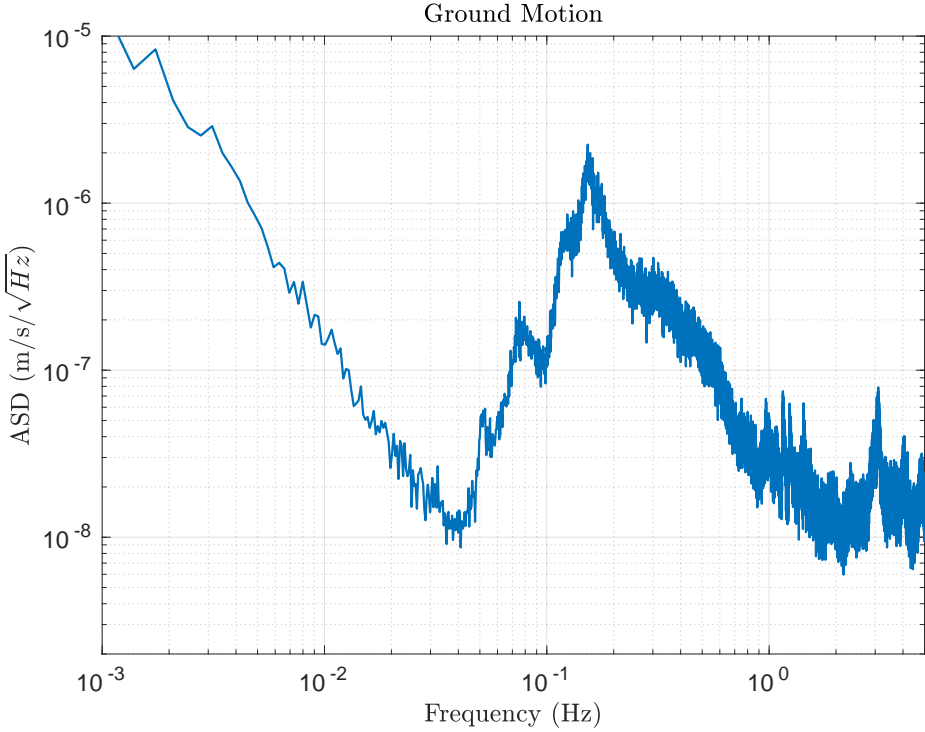
Figure 1.4: Example ambient, horizontal ground motion spectrum recorded at the End-X station of the LIGO Hanford Observatory. From 40 mHz to 1 Hz the spectrum is dominated by the oceanic microseism while above 1 Hz the seismic motion is sourced by local anthropogenic activity. Below 40 mHz, the instrument is dominated by tilt contamination described in Section 2.1.1

1.3.2   Internal Seismic Isolation

The ISI is comprised of two similar stages each suspended from steel blade springs and wires. The first (Stage 1) is suspended from HEPI (Stage 0) and the second (Stage 2) from the first. Each stage is controlled by a set of six magnetic actuators whose feedback signal is comprised of a collection of sensors. Noise curves for the sensors used in the seismic isolation system are shown in Figure 1.6. The motion of the table is sensed with a series of seismometers which are sensitive to motion with respect to an inertial frame. On the first stage, two separate models of seismometers are combined to obtain the lowest noise in a given frequency band.
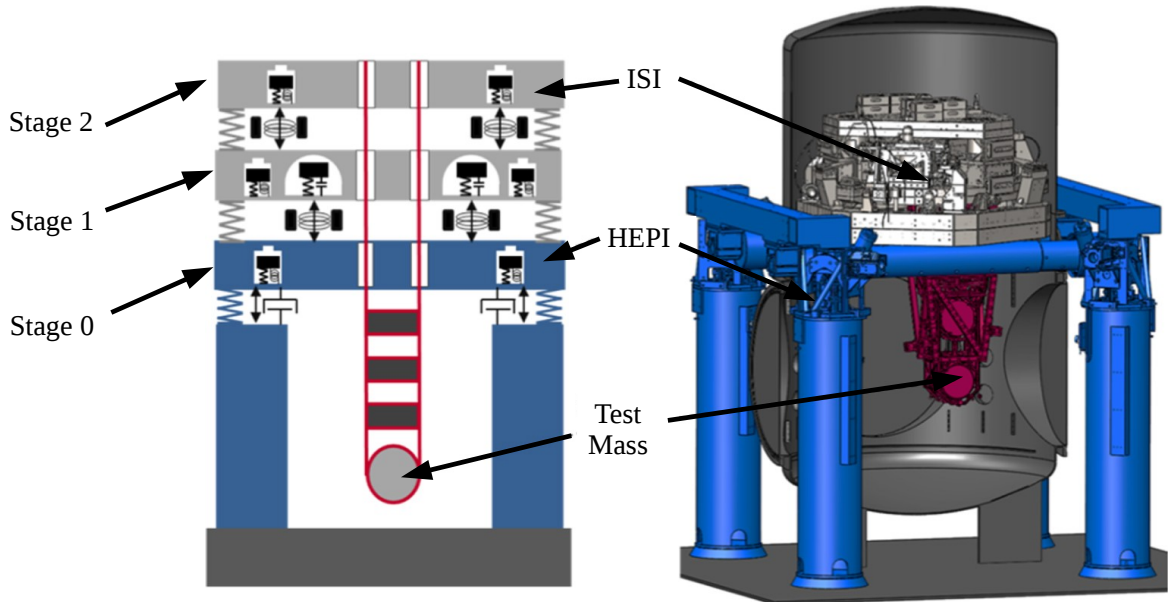
Figure 1.5: Schematic of the LIGO seismic isolation system. On the left is a cartoon showing the three stages of isolation while on the right is a CAD rendering of the seismic isolation system and vacuum chamber. Adapted from [29].

Sarcelles L4Cs are used above 0.5 Hz, while below this Trillium T240s are employed. These two sensors are "blended" together by sending the T240 through a low pass filter and the L4C through a high pass. The filtered signals are added together to form a low-noise broadband inertial sensor combination. The second-stage utilizes Geotech GS13s as its inertial sensors.

The inertial motion of the platform is sensed in all six degrees of freedom using three independent seismometers of each type located 1-meter apart. The three translational signals are composed from the average of the corresponding seismometer signals, while the three rotational degrees are sensed using the difference of the motion divided by the separation.
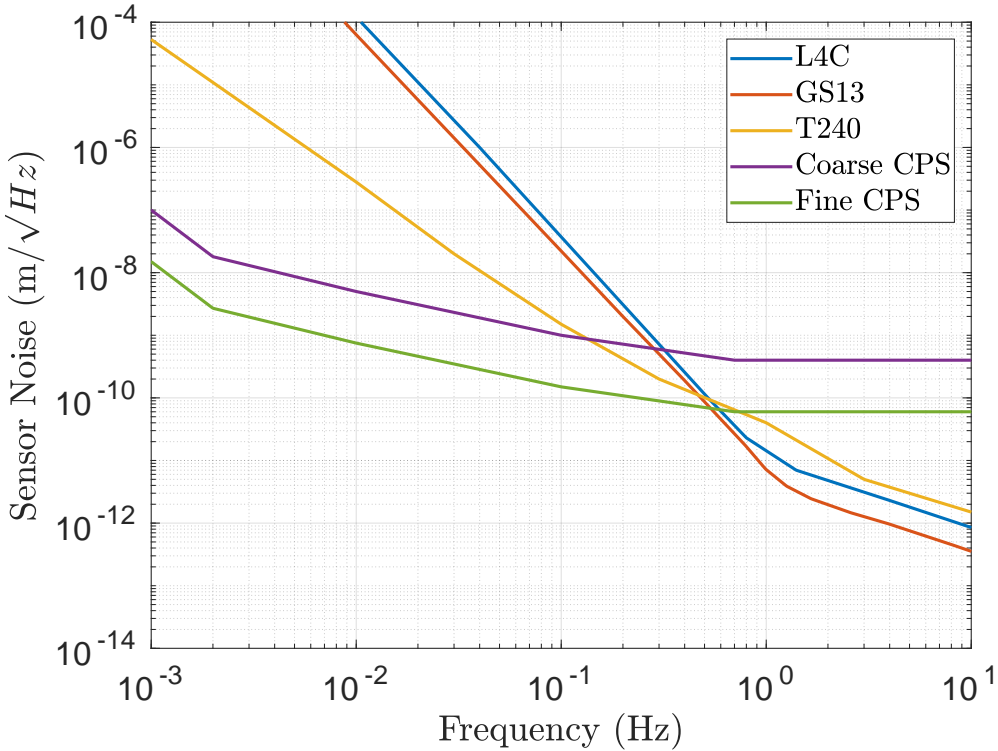
Figure 1.6: Sensor noise for the collection of sensors used on the ISI. The L4C, GS13, and T240 are seismometers while the Coarse CPS and Fine CPS are position sensors. The isolation system blends the relevant sensors together to achieve the lowest possible noise.

Due to the increased noise in seismometers at low frequency, a set of Capacitive Position Sensors (CPS) are deployed to detect the relative motion between either Stage 0 and the first ISI stage or the two stages of the ISI. This is then used as the control signal at low frequencies yielding a control for Stage 1 that follows:

$$x_{\mathrm{cont}} = F_{LP}\ (x_{\mathrm{p}} - x_{\mathrm{g}})_{,\mathrm{CPS}} + F_{BP}\ x_{\mathrm{p,\ T240}} + F_{HP}\ x_{\mathrm{p,\ GS13}} \tag{1.16}$$

where x_{cont} is the control signal, $x_{\mathrm{p,i}}$ is the platform motion sensed by the respective sensor, x_{g} is the ground motion, and F_{LP}, F_{BP}, F_{HP} are respectively a low-pass, band-pass, and high-pass filter. When this signal is utilized in feedback, the residual motion of the platform

can be approximated by:

$$\tilde{x}_p(\omega) \approx F_{LP} \left(\tilde{x}_g(\omega) + \tilde{n}_{\mathrm{CPS}}(\omega)\right) + F_{BP}\ \tilde{n}_{\mathrm{T240}}(\omega) + F_{HP}\ \tilde{n}_{\mathrm{GS13}}(\omega) \qquad (1.17)$$

where $\tilde{n}_i(\omega)$ is the sensor noise spectrum for the relevant sensor. This approximation ignores tilt-to-horizontal coupling which is addressed in Section 2.1.

1.3.3 Sensor Correction

The isolation can be further improved with the addition of a three-axis seismometer, in this case a Struckheisen STS-2, placed on the floor of the observatory. This measures the ground motion and can be used to do "sensor correction". Sensor correction is the procedure of subtracting the ground contribution of the CPS signal to recover the low frequency platform motion. The CPS signal in this case becomes:

$$x_{CPS} = F_{LP}\ (x_p - x_g) + F_{SC}\ x_g \qquad (1.18)$$

where F_{SC} is the "sensor correction" filter which has a pass-band that overlaps the CPS low pass filter. This can be rearranged to give:

$$x_{CPS} = \bar{F}_{LP}\ (x_p - x_g) + \bar{F}_{HP}\ x_p \qquad (1.19)$$

where the bars denote the relevant combination of F_{LP} and F_{SC} that yield effective low-pass and high-pass filters. This scheme allows for isolation down to 100 mHz and decreases the bleed-through of the ground motion due to the CPS low-pass filter's finite roll-off. Below 10 mHz, both the ground and platform seismometers are dominated by tilt contamination which is addressed in Section 2.1. The performance of the seismic isolation system can be seen in Figure 1.7.
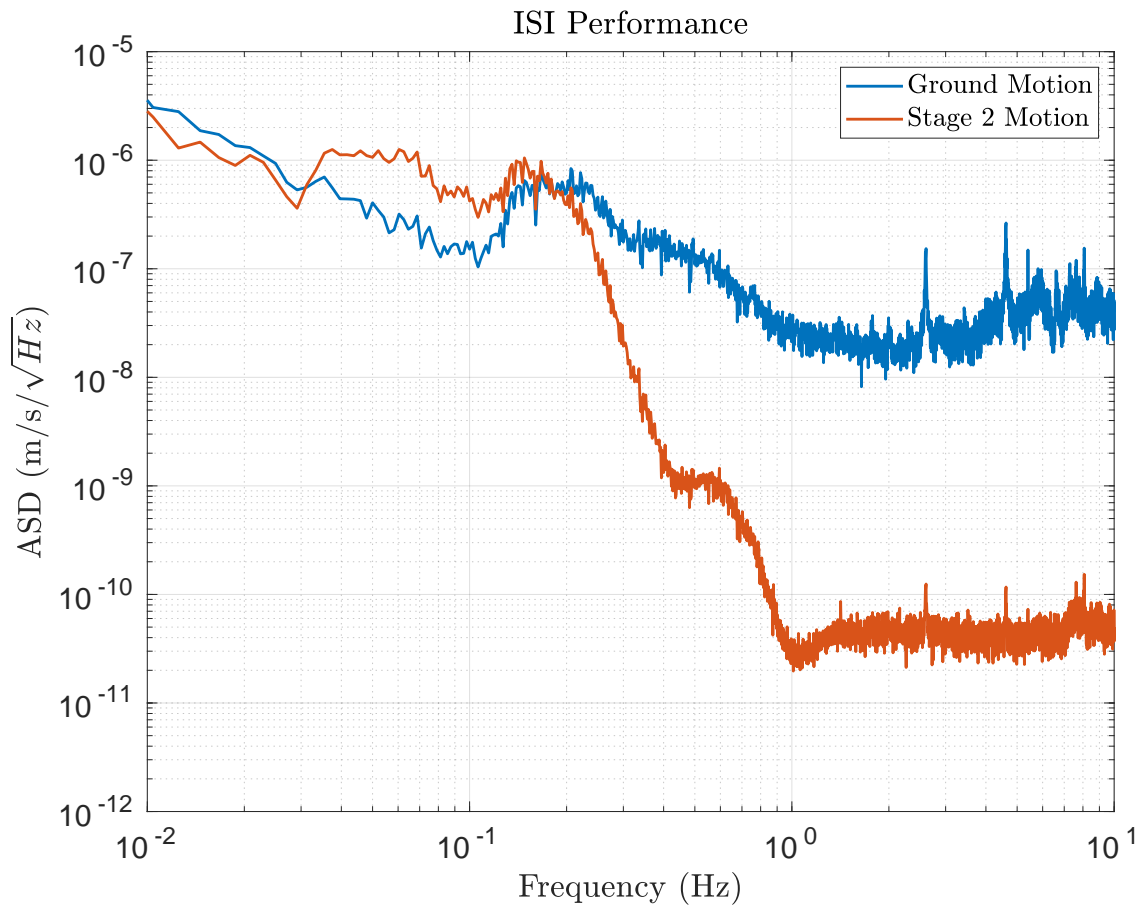
Figure 1.7: Performance of the ISI as measured by the GS13 installed on Stage 2. A factor of ~1000 reduction in motion is achieved above 1 Hz. Below which sensor noise and residual ground motion limit the performance.

Chapter 2

GROUND ROTATION SENSORS

2.1 Ground Tilt

2.1.1 Tilt Contamination

At their core, seismometers are low frequency spring-mass systems that measure the difference in motion between the casing and the device's proof mass. Above the resonant frequency of the spring-mass system, this difference measures the motion of the casing with respect to an inertial frame. Over the past century this technology has produced devices that are sensitive to ∼0.1 nm/s down to ∼10 mHz. However, these systems are intrinsically susceptible to any stray forces that act on the proof mass.

Of interest here is the contamination due to the rotation of the device within a external gravitational field, namely the field caused by the Earth. The rotation with respect to a fixed gravitational force will be referred to as "tilt".[1] From the proof mass's frame, a tilt is equivalent to a rotation of the gravitational force. This yields a horizontal acceleration of:

$$a = g \sin(\theta)$$

where g is the gravitational acceleration on the surface of the earth and θ is the angle by which the device is tilted. This acceleration adds a second term to the seismometer's output shown below for small angles and in the Fourier domain:

$$\tilde{x}_{seis}(\omega) = \tilde{x}_{trans}(\omega) + \frac{g}{\omega^2}\tilde{\theta}(\omega)$$

---

[1]Although a subtle difference, the distinction would be of great consequence if the local gravitational field were to vary rapidly. In that case the sensors described in Sections 2.2 and 3.2 would be of little use as they sense inertial rotations not tilts with respect to gravity.

where $\tilde{x}_{seis}$ is the seismometer's output in displacement units, $\tilde{x}_{trans}$ is the translational motion of the device, and ω is the angular frequency.

With this additional contribution, it is clear that, for a given amplitude of tilt, the contamination term contributes more at lower frequencies and can readily dominate the translational signal. In the context of the ground seismometers at the observatory, the tilt signal exceeds the translational component below $\sim$100 mHz. Above this frequency, the seismometer signal is dominated by the ever-present oceanic microseism. This can be seen in Figure 2.1 which shows the translation amplitude spectral density measured by a horizontal ground seismometer at LHO during both low and high wind conditions.
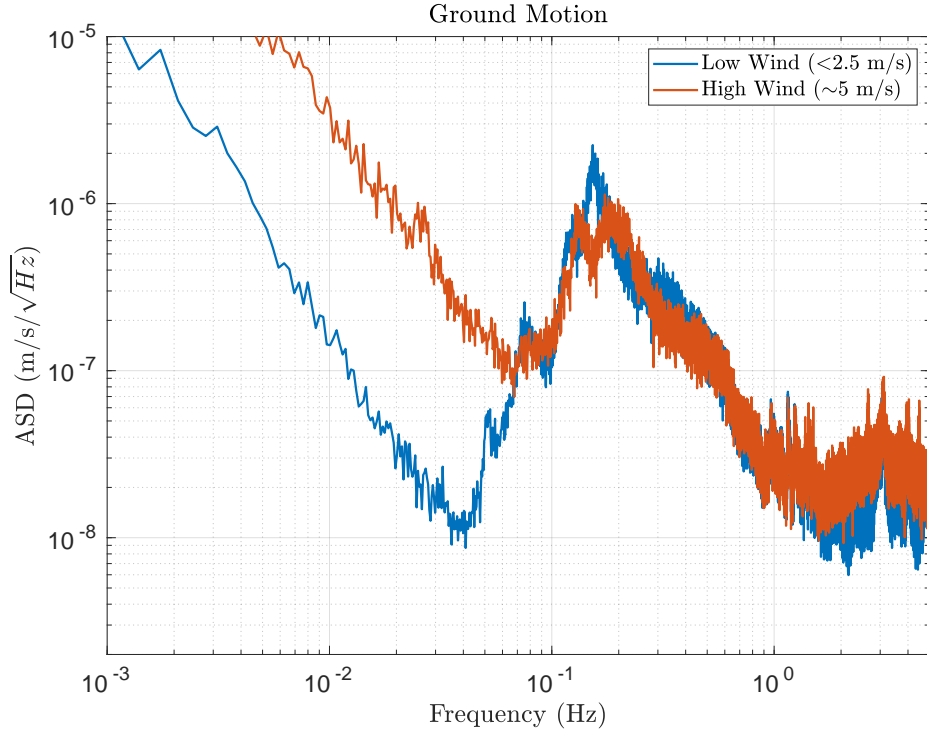
Figure 2.1: Horizontal ground motion spectra recorded at the End-X Station of the Hanford Observatory during low and high winds. Below 100 mHz, wind driven tilts become dominant during high winds. From 100 mHz to 1 Hz the spectra are dominated by the oceanic microseism while above 1 Hz the seismic motion is sourced by local anthropogenic activity.

The dominant driver of ground tilts at the observatories is wind acting on the walls of the building. Although one might naively assume that wind would rigidly rotate the building, the true mechanism is deformation of the concrete slab caused by differential pressure on the walls of the building. This increases the noise seen by the ground seismometer during high winds. The primary consequence of this excess is that the interferometer could not remain locked during high wind speeds. Additionally, due to nonlinear deformation of the floor, tilts measured in one location can not be simply extrapolated from the tilts measured at a different location.

2.1.2 Sensor Correction with Tilt Subtraction

Several different schemes, in principle, can combat such a contamination. The most straight-forward is to decrease the effect of wind by designing buildings that interact with the wind less or by installing wind blocks such as wind fences or earthen berms. Both of these options require significant construction and, for the case of LIGO, tilt contamination was not addressed in the observatory's architecture. Another option is to build seismometers that are suspended in such a way that they do not experience tilts. This is an active area of research and may one day yield tilt-free seismometers. [30]

The approach that will be explored here is to measure the tilt with an independent inertial rotation sensor, described in Section 2.2, and subtract the wind-driven contribution. This would then yield a corrected channel with the following form:

$$\tilde{x}_{seis}(\omega) = \tilde{x}_{trans}(\omega) + \frac{g}{\omega^2}\tilde{\theta}(\omega) \tag{2.1}$$

$$-\frac{g}{\omega^2}\tilde{\theta}_{meas}(\omega) \tag{2.2}$$

where $\tilde{\theta}_{meas}$ is the tilt seen by the rotation sensor. Given a subtraction factor of α between the tilt component of the seismometer and rotation sensors this yields the following:

$$\tilde{x}_{seis}(\omega) = \tilde{x}_{trans}(\omega) + \frac{g}{\omega^2}(1-\alpha)\tilde{\theta}(\omega)$$

Current installations have yielded an $\alpha \approx 0.9$. This yields a ground motion measurement with low tilt contamination which can be used within the seismic isolation system. As this correction decreases noise primarily at low frequencies, the feedback filters deployed within the isolation system can be tuned to cross over at a lower frequency away from the microseism. At the cross-over frequency, the filters have large gain and phase changes that degrade performance. Placing this cross-over below the microseism frequencies decreases the effects of this "gain peaking" and allows for isolation at lower frequencies. For more details see Reference [31].

2.2 Beam Rotation Sensors

2.2.1 Mechanical System

A Beam Rotation Sensor (BRS) is a beam-balance based inertial rotation sensor comprised of a 1-m long aluminum beam suspended by two 10-15 μm-thick beryllium-copper flexures. Details of the flexure design can be found in Section 2.2.2. The beam has a 1.7-kg brass mass attached to each end. These increase the moment of inertia to $I = 0.51$ kg m^2. Figure 2.3 shows a CAD model of the beam-balance.

The balance is stiff in all degrees of freedom except rotation about the horizontal axis that intersects the two pivot-points. The BRS can be described as a system consisting of two elementary subsystems: a rotational spring-mass system formed by the torsional stiffness of the flexures, and a simple gravitational pendulum due to the offset between the pivot point and the beam's center of mass. It is then described by the following equation of motion: [32]

$$I\ddot{\theta} + \gamma\dot{\theta} + \kappa(1 + \frac{i}{Q})(\theta - \theta_p) + Mg\delta\theta + M\delta\ddot{x}_p = \tau_{ex} \qquad (2.3)$$

where θ and θ_p are, respectively, the angles of the beam and the platform with respect to gravitational vertical, τ_{ex} is the sum of all exterior torques, I is the beam's moment of inertia, Q is the intrinsic quality factor, γ is the velocity damping factor, κ is the spring constant of the flexures, M is the mass of the balance, g is the gravitational acceleration, δ is the
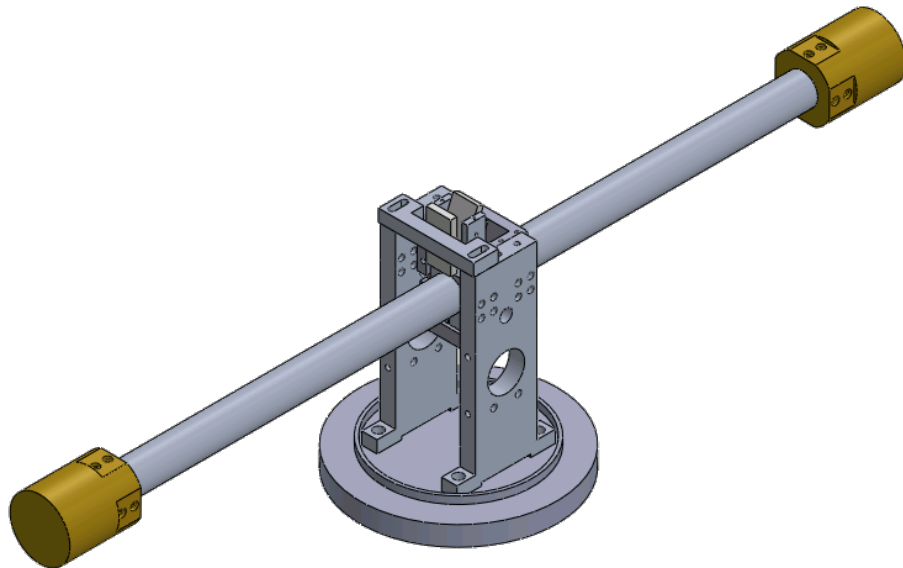
Figure 2.2: CAD rendering of the BRS with the vacuum and optical readout systems omitted. The beam with its two brass end masses can be seen along with its attached mirrors and support structure.
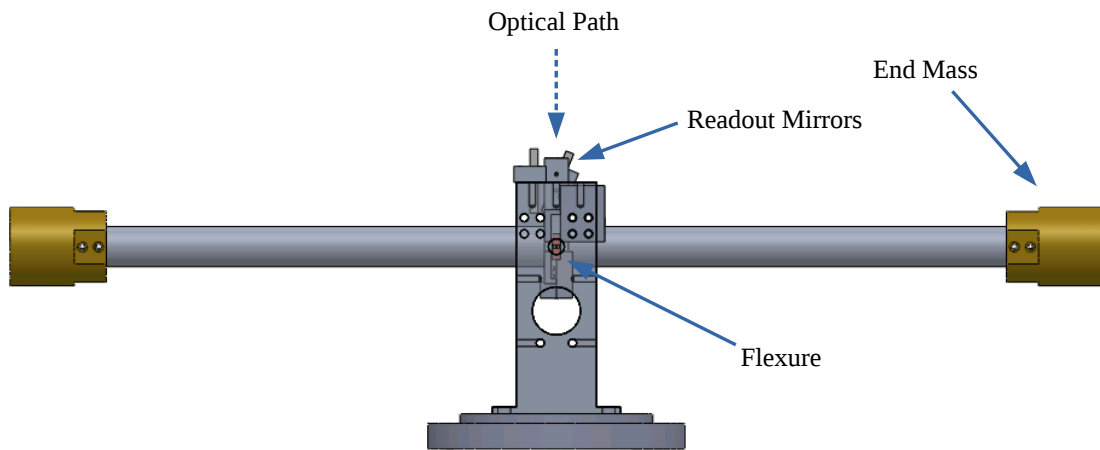
Figure 2.3: Side view of a CAD rendering of the BRS. At center, one of the small copper-colored flexures can be seen. The other is mounted on the opposite side.

vertical distance from the center of mass to the pivot point, and x_p is the translation of the platform. Equation 2.3 can be rearranged to yield:

$$\tilde{\theta} = -\frac{\tilde{\tau}_{ex} + \omega^2 M \delta \tilde{x}_p + \kappa(1 + i/Q)\tilde{\theta}_p}{I\omega^2 - i\gamma\omega - i\kappa/Q - \kappa - Mg\delta} \tag{2.4}$$

where ω is the angular frequency of motion and tildes denote spectral amplitudes. For the BRS, the measured quantity is not the angle of the beam but the difference in angle between the beam and the platform. Thus the angle recorded by the readout, θ_a, follows:

$$\tilde{\theta}_a = \tilde{\theta} - \tilde{\theta}_p \tag{2.5}$$

$$= -\frac{\tilde{\tau}_{ex} + \omega^2 M \delta \tilde{x}_p - (I\omega^2 - i\gamma\omega - Mg\delta)\tilde{\theta}_p}{I\omega^2 - i\gamma\omega - i\kappa/Q - \kappa - Mg\delta} \tag{2.6}$$

This equation can be broken into three distinct terms: the angular motion due to external torques, θ_τ, due to translational coupling, θ_x, and due to rotation of the platform, θ_s.

$$\tilde{\theta}_a = \tilde{\theta}_\tau + \tilde{\theta}_x + \tilde{\theta}_s \tag{2.7}$$

$$\tilde{\theta}_\tau = -\frac{\tilde{\tau}_{ex}}{I}\frac{1}{\omega^2 - i(\omega_0\omega/q + \omega_0^2/Q) - (\omega_0^2 + \omega_g^2)} \tag{2.8}$$

$$\tilde{\theta}_x = -\tilde{x}_p\frac{M\delta}{I}\frac{\omega^2}{\omega^2 - i(\omega_0\omega/q + \omega_0^2/Q) - (\omega_0^2 + \omega_g^2)} \tag{2.9}$$

$$\tilde{\theta}_s = -\tilde{\theta}_p\frac{\omega^2 - i\omega_0\omega/q - \omega_g^2}{\omega^2 - i(\omega_0\omega/q + \omega_0^2/Q) - (\omega_0^2 + \omega_g^2)} \tag{2.10}$$

where $\omega_0 = \sqrt{k/I}$ is the resonant frequency, $\omega_g = \sqrt{Mg\delta/I}$, and q is the quality factor due to velocity damping. These equations show that the beam has a resonance at $\omega = \sqrt{\omega_0^2 + \omega_g^2}$ and $\tilde{\theta}_s$ has a minimum at $\omega = \omega_g$.

To obtain high fidelity rotation sensing, the translational coupling must be negligible. To achieve this, the magnitude of δ must be minimized. This is accomplished through the design of the beam's suspension which places the center of mass close to the pivot point.
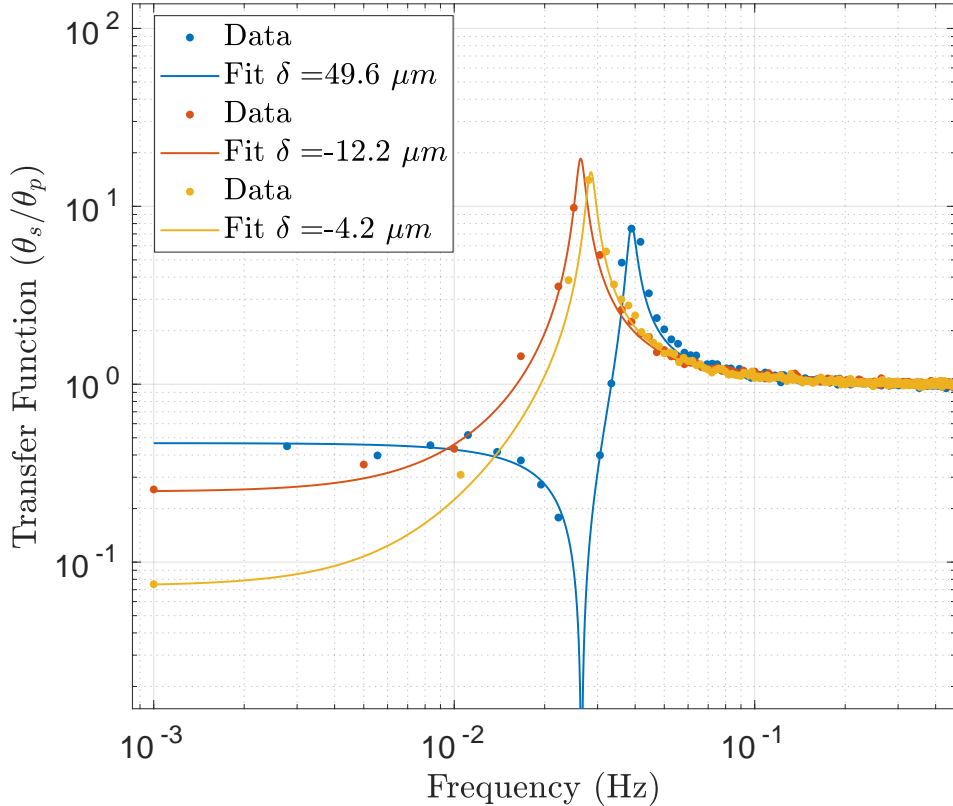
Figure 2.4: Measurements of the transfer function from platform tilt to measured tilt for the compact-BRS, described in Chapter 3, along with fits to Equation 2.10. After each measurement mass was added or removed from the top of the proof mass in order to shift the vertical position of its center of mass.

Fine adjustments are then made by adding mass to the beam above or below the pivot. These adjustments are guided by measurements of the $\tilde{\theta}_s$ transfer function, Equation 2.10. Figure 2.4 shows this for the compact-BRS, described in Chapter 3. The amount of tuning that was achieved differed for each device deployed at the observatories due to scheduling constraints. The lowest translation coupling was achieved at the LHO End-Y BRS which had $\delta < 0.5$ μm yielding a translational coupling of $< 10^{-6}$ rad/m.

2.2.2 Flexures

The flexures that suspend the proof mass were cut from $1/4'' \times 1/4'' \times 7/8''$ blocks of beryllium-copper by wire electrical-discharge machining to yield the shape shown in Figure 2.5. Circular cuts were used to achieve a well-defined pivot point. The opening gaps on either side were restricted to act as mechanical stops for ease of handling and transportation.

Due to machining variation in the width of flexure, batches of flexures were assayed via a microscope to determine the width of each flexure and to identify flexures that were damaged during machining and transportation. Pairs of flexures with similar widths were installed together, one on each side of the beam. Each flexure has one half clamped to the support and the other attached to the beam, as shown in Figure 2.6. This provides a suspension which is stiff in all degrees of freedom except rotation about the axis intersecting the two pivot points.

The stiffness of the flexure increases with thickness. Thus, the flexure width was minimized to decrease the resonant frequency of the beam balance. This was limited practically by the motion of the machining wire to yield flexures with widths of 10-15 μm. Although, flexures thinner than 10 μm could be achieved, the finished pieces contained irregular holes laterally through the flexure. These flexures would have lower breaking-strength and would degrade the performance if installed in a BRS.

2.2.3 Vacuum System

To decrease the effects of air currents and gas damping, each BRS is placed into its own vacuum chamber that emulates the outline of the device, shown in Figure 2.7. This chamber is initially evacuated to $\sim \mu$Torr pressures using a roughing pump and turbomolecular pump. After which, the vacuum is maintained by a 10 l/s ion pump which further decreased the pressure to $\sim$0.1 μTorr.
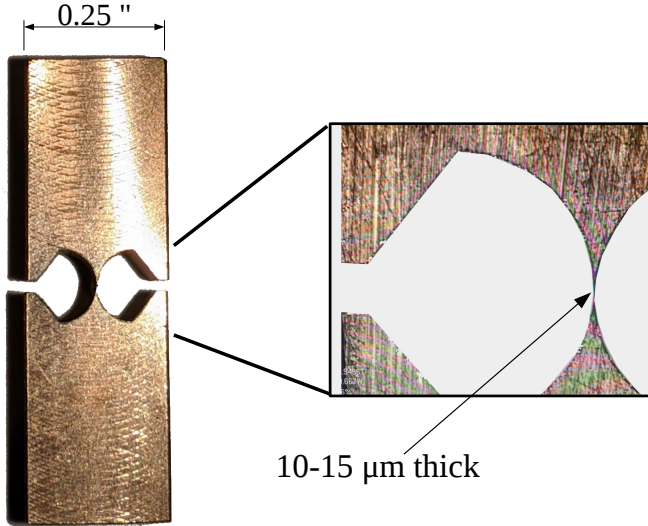
Figure 2.5: Image of a flexure used to suspend the beam balance with detail showing a microscope image of the flexure point.

2.2.4 Multi-Slit Autocollimator Readout

The angular deflection is measured by a multi-slit autocollimator [33] that can be viewed as an improved optical lever.

Optical levers are simple optical angular readouts that exploit the law of reflection to measure angular deflections of a mirror by observing the displacement of a reflected beam of light. The angle of the mirror is described as:

$$\theta_s = \frac{x_{\text{reflected}}}{2d} \tag{2.11}$$

where θ_{mirror} is the angle of the mirror, $x_{\text{reflected}}$ is the displacement of the reflected beam, and d is the distance between the optical system and the mirror. This allows one to increase
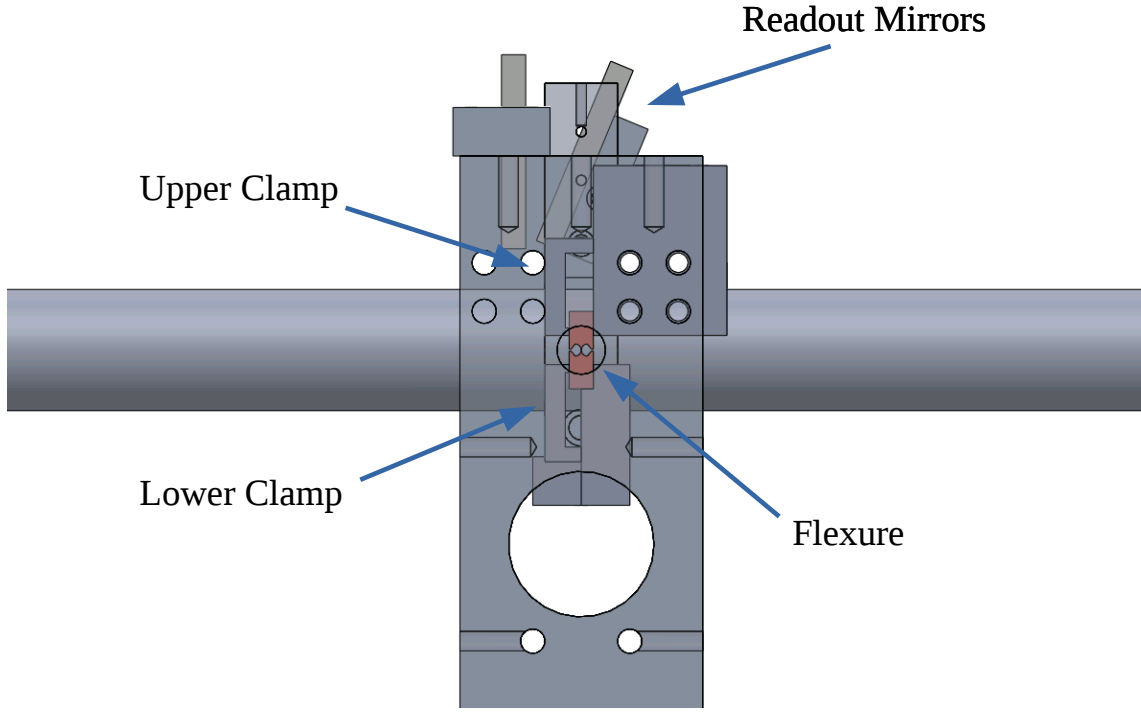
Figure 2.6: Close-up view of the center of the CAD rendering of the BRS. One of the copper colored flexures can be seen at center along with its clamps. The two gray blocks at the top are mirrors for optical sensing, one fixed to the support the other attached to the beam.

the precious of the angular measurements arbitrarily by increasing d. However, with this comes the disadvantage that the effective gain of the sensor depends on d which may not be well known and may vary in time.

An autocollimator [33] adds a lens located one focal-length from both the light source and the detector. This effectively replaces the distance dependence with the focal length of the lens. Thus the system, to first order, is only sensitive to the angular motion of the mirror.

To improve this system further, a partially-reflective mirror can be placed in between the
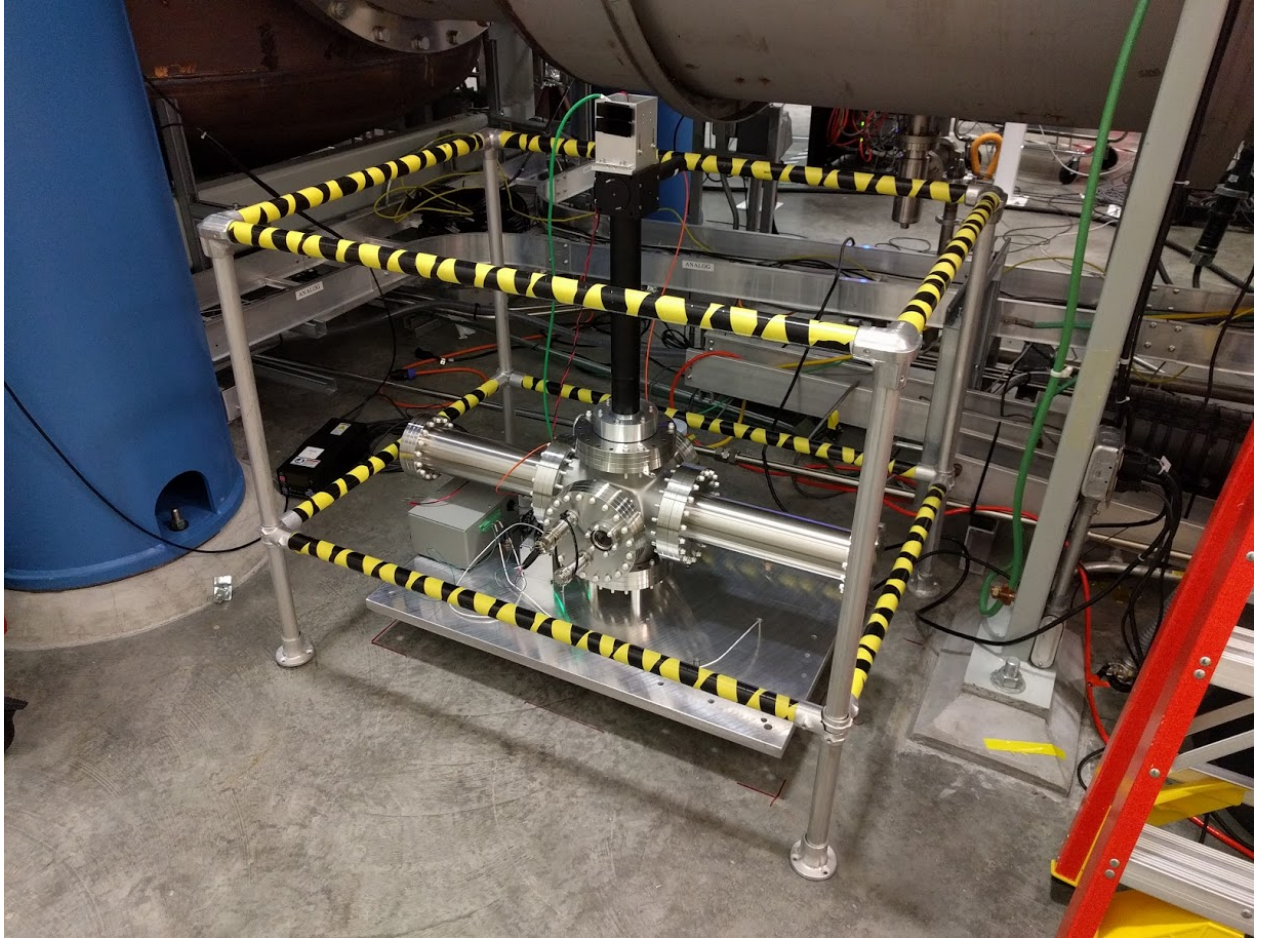
Figure 2.7: Picture of the BRS installed at LIGO Livingston Observatory End-Y before the installation of the thermal insulation.

autocollimator and the main mirror to act as a reference. This allows for the subtraction of any perceived motion that is not due to motion of the main mirror. The angular readout is then described by:

$$\theta_s = \frac{x_{\text{main}} - x_{\text{reference}}}{2f} \tag{2.12}$$

where f is the focal length of the lens and $x_{\text{reference}}$ is the location of the beam-spot from the reference mirror.

For the BRSs, high angular sensitivity was achieved by employing a multi-slit autocol-
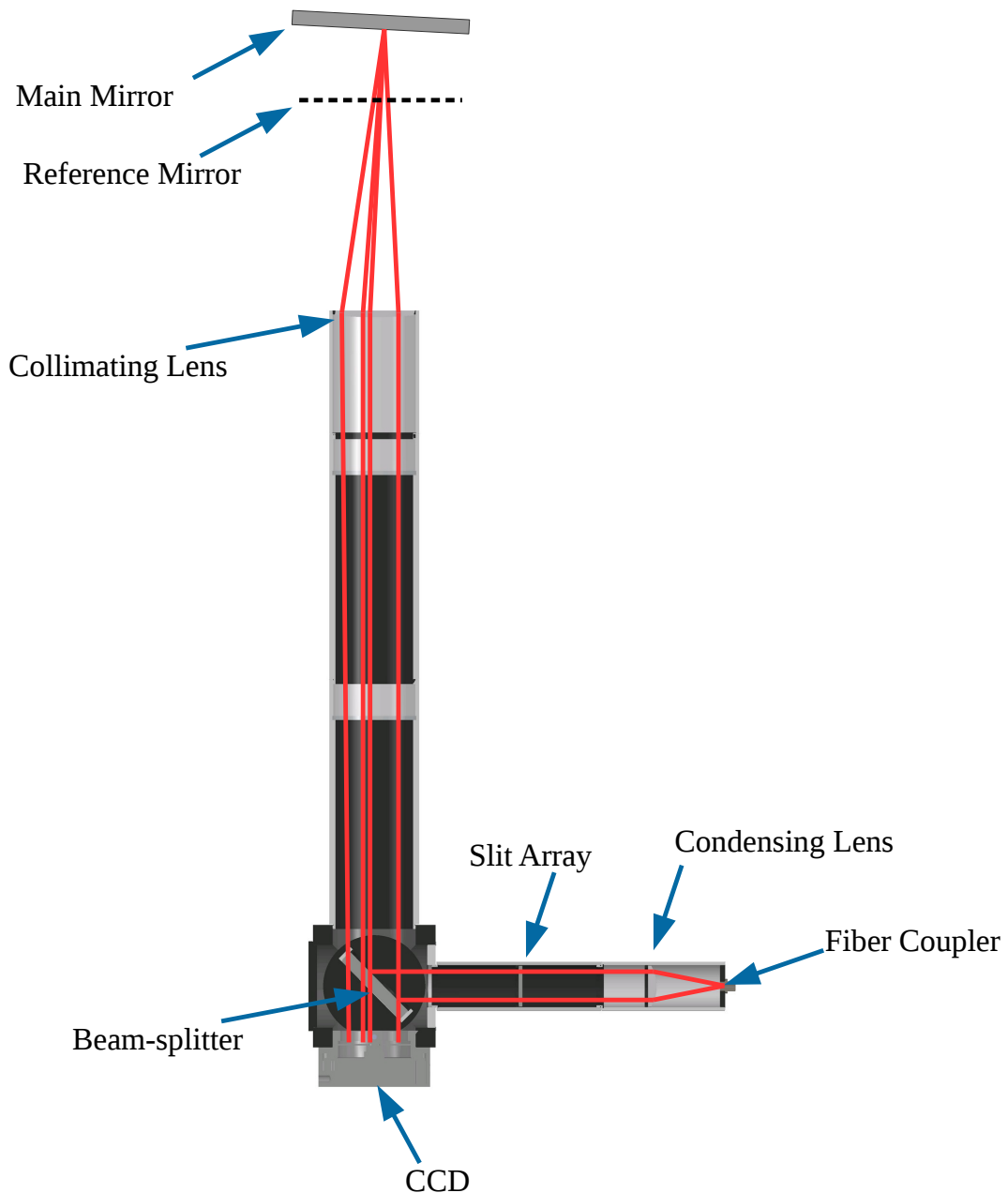
Figure 2.8: Schematic of a multi-slit autocollimator used as the angular readout of the BRSs. The light enters through the fiber coupler, is collimated by the condensing lens, and images the slit array. This image is then partially reflected by the beam-splitter, focused onto the main mirror by the collimating lens, and returns through the collimating lens to be imaged on the CCD. A second pattern is made by the partial reflection off the reference mirror and is also imaged on the CCD. CAD rendering originally created by Erik Shaw.

Parameter	Value
CCD	Balser Racer raL4096-24 gm
Pixel Number	4096
Pixel Size	7 μm $\times$ 7 μm
Pixel Depth	12 bits
Light Source	Fiber coupled LED
Wavelength	455 nm
Condensing lens focus	50 mm
Collimating lens focus	500 mm
Number of slits	38
Slit size	$\sim$0.127 mm

Table 2.1: Parameters of the BRS multi-slit autocollimators.

limator [33], shown in Figure 2.8. This consists of an autocollimator with the light source replaced by a illuminated photomask of a number of thin slits. The pattern is then reflected off a set of reference and main mirrors and imaged by a line CCD camera. Table 2.1 displays the parameters used for the BRS autocollimators. These images are then analyzed to measure the distance between them to yield a measurement of angle. This image analysis is achieved using custom software. [34]

To extract the distance between the patterns, the image goes through a series of steps to convert from a vector of pixel intensities to a single angular output. When the software begins, the first frame is saved. All future frames are split into two, with one part representing the reference mirror and the other the main mirror. A cross-correlation is then taken between each part and its matching section of the first frame. This gives a curve with a maximum located at the pixel number corresponding to the separation between the pattern in the current frame and the first frame, which can be seen in Figure 2.9. The points of this curve
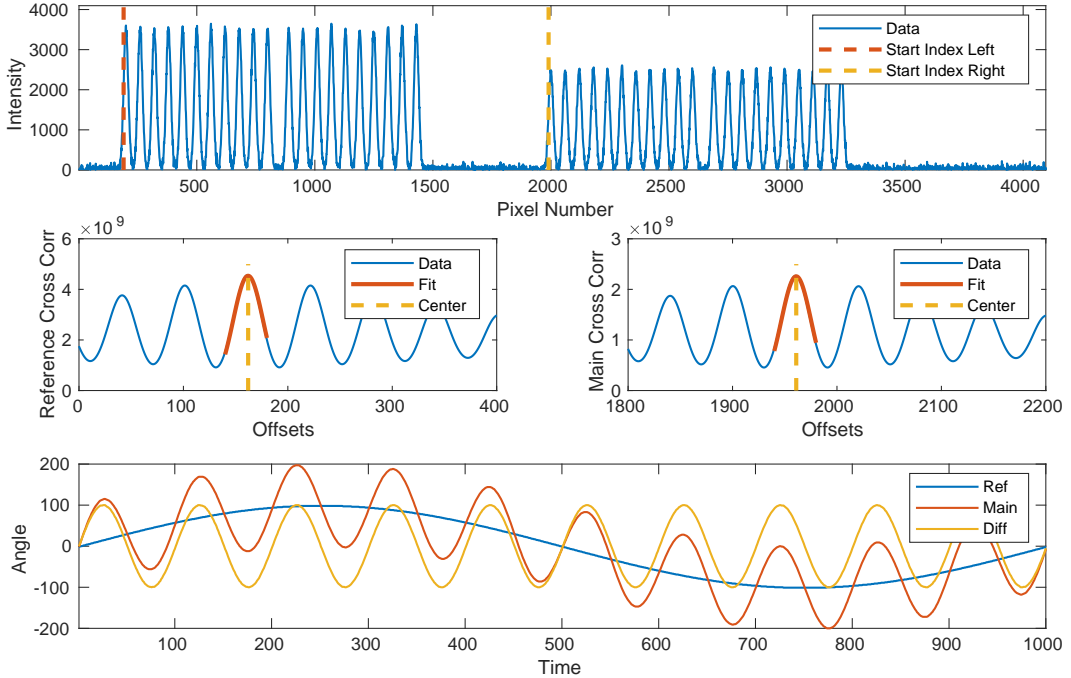
Figure 2.9: Simulation of the BRS image-analysis algorithm. The top pane shows a simulated frame of the fringes as seen by the CCD, the middle panes show the cross-correlation and fit from the two patterns, and the bottom shows the output of the algorithm for each pattern and the difference of the two. For this simulation the main pattern was modulated at both 1 mHz and 10 mHz while the reference was at 1 mHz.

nearest to the maximum are then fit to a Gaussian which gives the location of the peak with sub-pixel resolution. This process is done for each pattern separately after which the difference between the reference pattern location and the main pattern location is taken. The difference is then proportional to the change in angle between reference mirror and main mirror following Equation 2.12.

Compared to previous image analysis algorithms [33], this algorithm is computationally efficient while also being less susceptible to variations in the pattern image due to dust particulate, incorrect focusing, or beam clipping. A sensitivity of ~ 0.3 nrad/$\sqrt{\text{Hz}}$ at 0.1 Hz

was achieved with this autocollimator design and image analysis algorithm.

2.2.5 Controls

As the BRSs are installed in active lab spaces, anthropogenic activity and environmental disturbances apply torques to the beam-balance through mechanical and gravitational coupling. These torques can cause the motion at the resonant frequency to rise to undesirable amplitudes. As the beam motion increases so does the noise and the effects of non-linearities of the readout. In addition, some disturbances can cause the amplitude to exceed the dynamic range of the autocollimator readout system.

The alleviate this issue, we installed capacitor plates underneath each end of the beam-balance to act as actuators. Neglecting edge effects, the force between the two parallel capacitor plates is:

$$F = \frac{\epsilon A V^2}{2d^2} \tag{2.13}$$

where ϵ is the permittivity of the volume between the plates, A is the area of the plate, V is the voltage applied to the plates, and d is the distance between the plates. The plates under the beam are connected to a digital-to-analog converter while the beam is electrically grounded so that a controlled actuation torque can be applied to the beam.

The feedback signal sent to the capacitors was the angular velocity of the beam, band-passed between 2 mHz and 20 mHz to include only motion at frequencies near the resonance. The feedback is applied with low gain to only increase the loss of the system as compared to strong feedback where all of the motion is absorbed into the controls. This arrangement is implemented with two gain levels, a "low amplitude" level, which is always on and yields an observed quality factor[2], Q_{obs}, of 10-15, and a "high amplitude" level, which is triggered if the amplitude rises above a threshold that is set based on the properties of the given device and gives a Q_{obs} of 5-10.

---

[2]The observed quality factor was obtained by measuring the ring down of excited resonant motion. This quality factor is due to the combination of intrinsic and external losses.
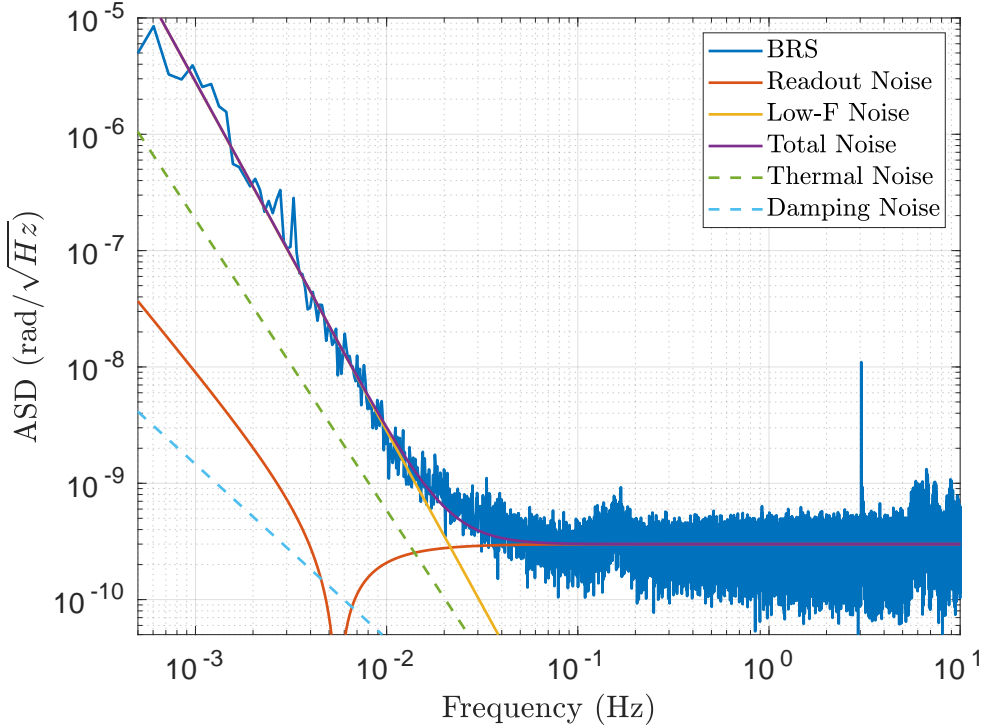
Figure 2.10: Noise budget for the Beam Rotation Sensors where the blue curve shows the performance at a quiet time, in red is a model of the readout noise, yellow shows an estimate of the low-frequency noise, purple shows the sum of these, and cyan and green show upper limits of the thermal and damping noise. The low-f noise is thought to be due to residual temperature variations.

2.2.6   Noise Performance

In addition to the 0.3 nrad/$\sqrt{\mathrm{Hz}}$ frequency-independent noise of the autocollimator readout, the BRSs have a collection of mechanical noise sources, especially temperature variations and thermal motion of the flexures.

Although the exact physical mechanism is unknown, it has been observed that variations in the exterior temperature cause shifts in the instrument's equilibrium position. Furthermore, temperature gradients across the instrument emanating from unbalanced heat sources and air currents can cause time-varying noise. To alleviate this issue, the instrument's vac-

uum chamber and optics are wrapped in multiple alternating layers of packing foam and aluminum foil. The entire apparatus is placed inside a large double walled insulation box to further decrease any temperature variation. These improvements decrease these effects yet temperature noise is believed to limit the performance below 20 mHz.

More fundamental is the noise due to thermal excitations of the flexure. At non-zero temperature, a portion of the thermal energy of the flexures excites mechanical motion. This causes a fundamental stochastic noise floor that follows [35]:

$$\tilde{\theta}_T(\omega) = \sqrt{\frac{4k_B T \omega_0^2}{I\omega Q\big((\omega^2 - \omega_0^2)^2 + \omega_0^4/Q^2\big)}} \tag{2.14}$$

where k_B is Boltzmann's constant and T is the temperature.

To limit the influence on the performance of the device, the resonant frequency of the spring-mass system is pushed to the lowest feasible frequency. This is the fundamental noise of the instrument, independent of readout and environmental effects.

One further noise source comes from voltage noise on the capacitive actuators. The force follows Equation 2.1. Assuming a voltage noise on the capacitors of 0.1 V/$\sqrt{\text{Hz}}$, larger than expected with the installed electronics, the corresponding torque noise is 4.3×10^{-13} N/$\sqrt{\text{Hz}}$. This then leads to an angle noise that is ~100 times below the measured noise.

The noise budget for the LHO End-X BRS is shown in Figure 2.10. It shows that the device is readout dominated above ~20 mHz and below is dominated by unknown noise thought to be sourced by temperature variations. The peaks at 150 mHz, 3 Hz, and 6 Hz arise from the rotational microseism, torsion mode of the beam-balance, and motion due to nearby instrumentation, respectively.

2.3   Results

2.3.1   Hanford Installation

A BRS was installed at each of the end stations of the LIGO Hanford Observatory (LHO) between the first (O1) and second (O2) observing runs. Each device was used to correct
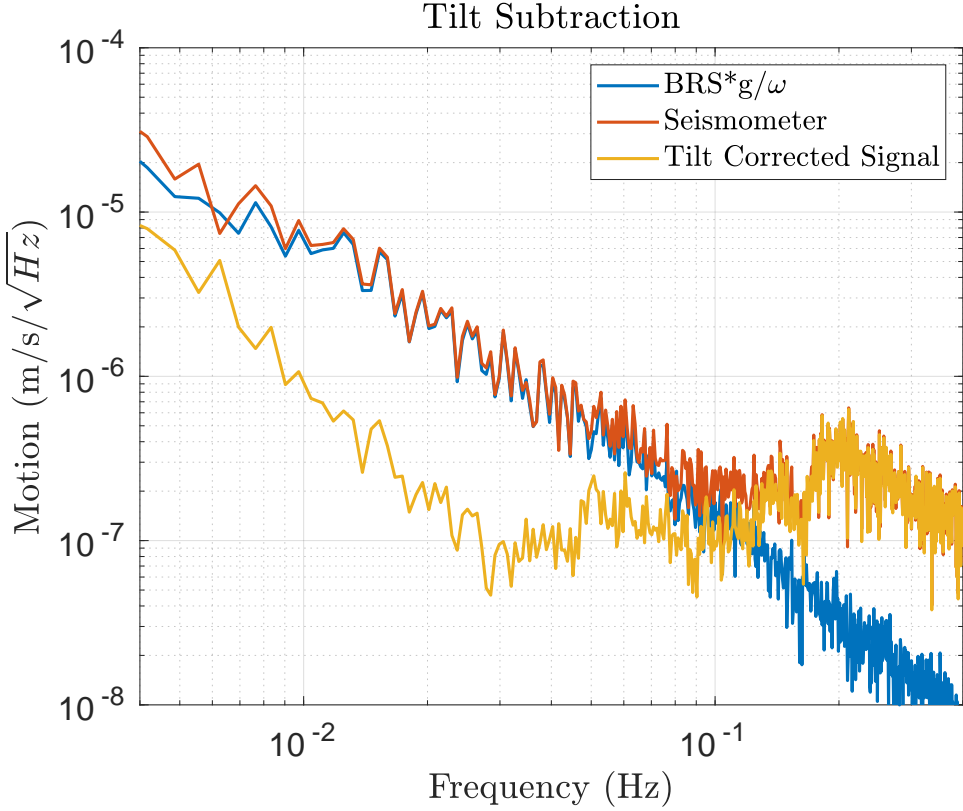
Figure 2.11: Representative amplitude spectral density showing the tilt subtraction during ~11 m/s winds achieved at End-X of LHO where blue is the BRS signal multiplied by g/ω, red is the raw seismometer signal, and yellow is the tilt corrected signal. Similar perform has been achieved by all of the deployed BRSs.

the translation along the respective arm of the interferometer.[3] Although one would expect that the corner station seismometers would also need to be corrected, a location was found within the corner station building which exhibited low tilt.[4] As such no BRS was necessary to achieve low tilt contamination.

The tilt subtraction performance achieved with these devices can be seen in Figure 2.11

---

[3]Motion orthogonal to the interferometer arms couples only indirectly through pathways such as defects of the test masses and mechanical cross couplings. Thus this coupling is significantly suppressed compared to motion along the arms.

[4]This location had low tilt because of its distance from the walls of the building.

where it is evident that the system achieves tilt subtraction from around 6 mHz to 50 mHz. Above 50 mHz the seismometer signal is dominated by the oceanic microseism and the tilt contribution is negligible. Below 6 mHz, the BRS signal becomes overwhelmed by instrumental noise. This performance can also be seen in Figure 2.12 which shows a example time series of the tilt subtraction where suppression of a handful of transients, likely due to wind gusts, can be seen.
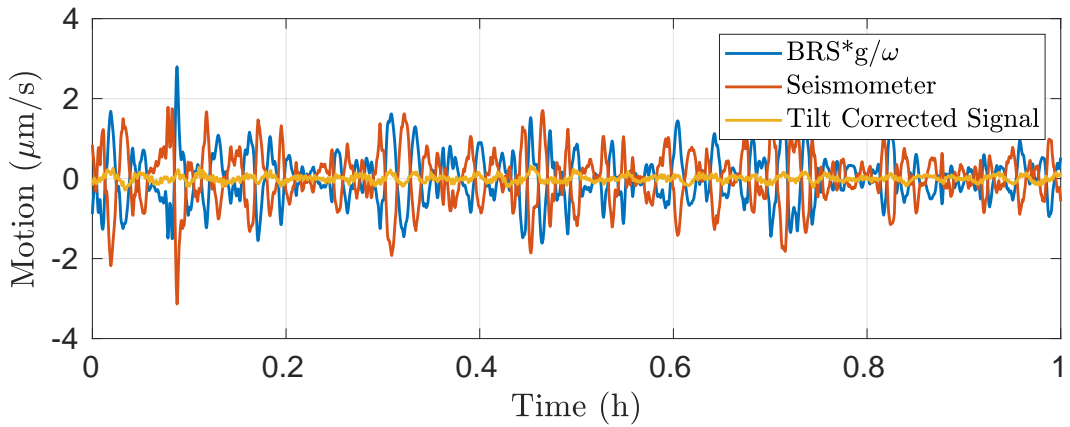
Figure 2.12: Time series showing the tilt subtraction at End-X of LHO where blue is the BRS signal multiplied by g/ω, red is the raw seismometer signal, and yellow is the tilt corrected signal. All channels are band-passed from 10-100 mHz. As can be seen, the tilt subtraction removes a collection of transients, likely due to the gusts of wind.

This tilt-subtracted channel, rather than the raw seismometer, was then used as the ground signal for the isolation system's sensor correction, described in Section 1.3.3. The primary effect on the interferometer of using this channel is a decrease in the differential motion between pairs of platforms which form the arms of the interferometer. Figure 2.13 shows that the differential motion was decreased by a factor of ∼3-4 between 20-100 mHz. This increases the ability to lock the interferometer by decreasing the demand on the downstream control systems.
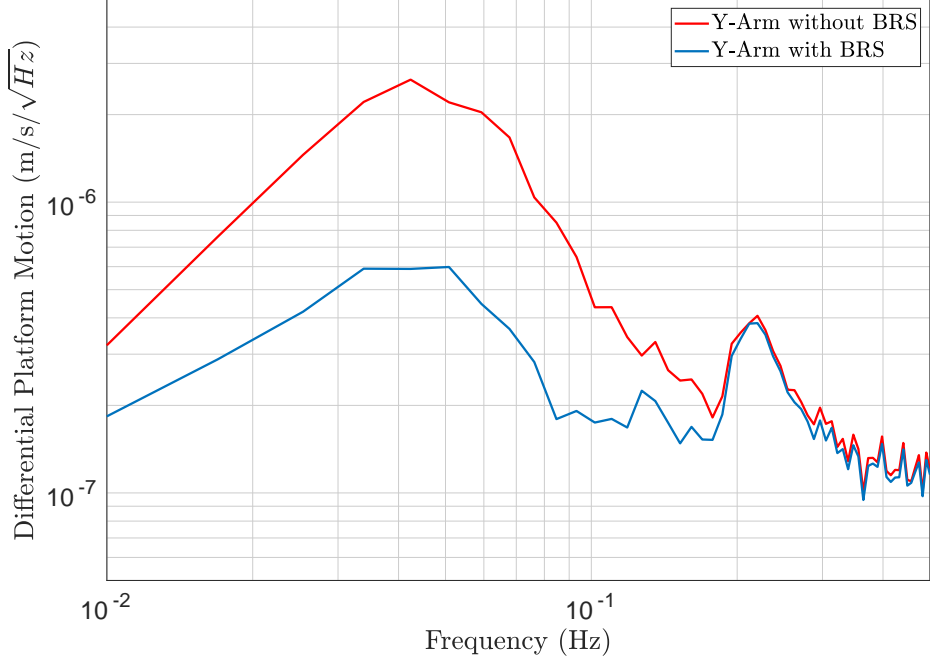
Figure 2.13: Differential platform motion as measured by the capacitive position sensors (CPS) for the Y-Arm of LHO with and without the BRSs installed. Below ∼30 mHz, the CPS reading is driven to zero by the control system. Adapted from [31].

2.3.2 Livingston Installation

After the success of the Hanford BRS installation, four devices were installed at the LIGO Livingston Observatory (LLO) between the second and third (O3) observing runs. Due to differences in the size and shape of the corner station building at LLO, a low tilt location was not found. Therefore BRSs were installed near the input test masses along with one at each end station. Each device corrected the seismometer readings along the corresponding interferometer arm.

All four devices achieved comparable tilt-subtraction as the Hanford installation and were implemented in a similar fashion.

2.3.3   Ground Tilt Model

As mentioned in Section 2.1.1, the primary driver of ground tilts at the observatories is wind acting on the building's walls. This deforms the concrete floor in a non-trivial manner. Thus modeling the ground tilt spectrum for a given wind speed from first principals is intractable. However, with observations made by the installed BRSs, an empirical model can be readily constructed.

To achieve this, hour long spectra of the LHO End-X BRS readings during O3a were sorted into a collection of bins corresponding to the average wind speed during that hour. Each bin was then averaged to yield a representative spectrum for each wind speed. These averages were fit to an empirically determined model, Equation 2.15, containing two terms: the first capturing the broad behavior of the spectrum and a second which enhances the high frequency motion at high wind speeds. The parameters of these terms were then fit vs wind speed to yield a tilt spectrum vs wind speed model.

$$\tilde{\theta} = \frac{x_1}{(f/1 \text{ Hz})^{2/3}(1 + f/f_1)} + \frac{x_2}{1 + (f/f_2)^3} , \tag{2.15}$$

$f_1 = 0.2$ Hz

$f_2 = (0.1 \ (s/1 \text{ m/s}) - 0.25)$ Hz if $s > 2.5$ m/s else $f_2 = 0$

$x_1 = (1.4 \times 10^{-11} \ (s/1 \text{ m/s})^2 + 5.7 \times 10^{-11} \ (s/1 \text{ m/s}) + 6.4 \times 10^{-11}) \text{ rad}/\sqrt{\text{Hz}}$

$x_2 = (1.8 \times 10^{-10} \ (s/1 \text{ m/s})^2 - 7.6 \times 10^{-10} \ (s/1 \text{ m/s}) + 1.2 \times 10^{-9}) \text{ rad}/\sqrt{\text{Hz}}$

where s is the wind speed, f is the frequency, and $\tilde{\theta}$ is the tilt spectral density. This model is compared to data in Figure 2.14. There is good agreement between the modeled and measured tilt at most wind speeds. Below 1 m/s, the tilt due to the microseismic motion and the sensor noise dominate above 100 mHz. The data between 1-2 m/s were corrupted by local anthropologic activity above $\sim$50 mHz. This model can be utilized to calculate the
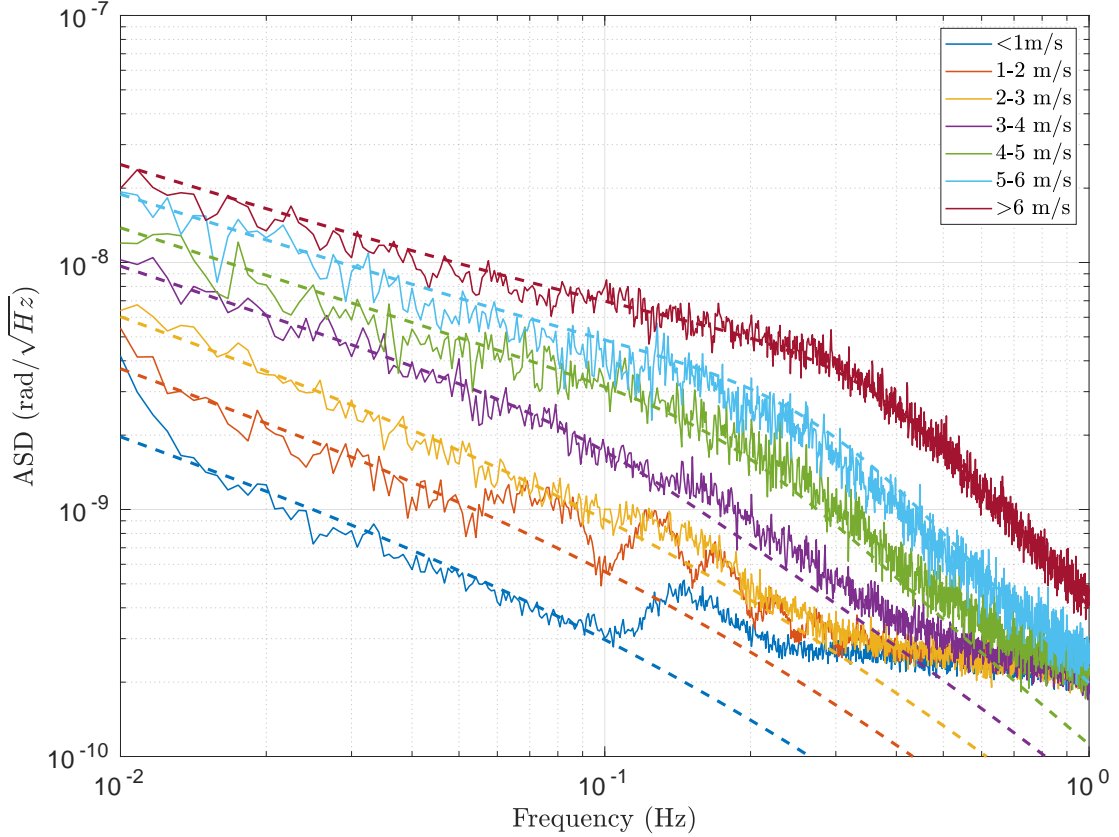
Figure 2.14: Observed and modeled tilt at various wind speeds for LHO End-X BRS. The solid lines are the measured ground tilt while the dashed are the model. At low wind speeds, the BRS noise and the microseism dominate at high frequencies.

theoretical performance of the seismic isolation, as is done in Section 3.3.1.

2.3.4   Duty Cycle Improvements

The figure of merit which most clearly displays the improvements in duty cycle with the inclusion of the BRSs in the seismic isolation system is the empirical probability of having the interferometer locked at a given wind speed during the three observing runs. This is shown in Figures 2.15 and 2.16 for LHO and LLO, respectively. Note that BRSs were

implemented at Hanford for both O2 and O3a while Livingston was only for O3a.
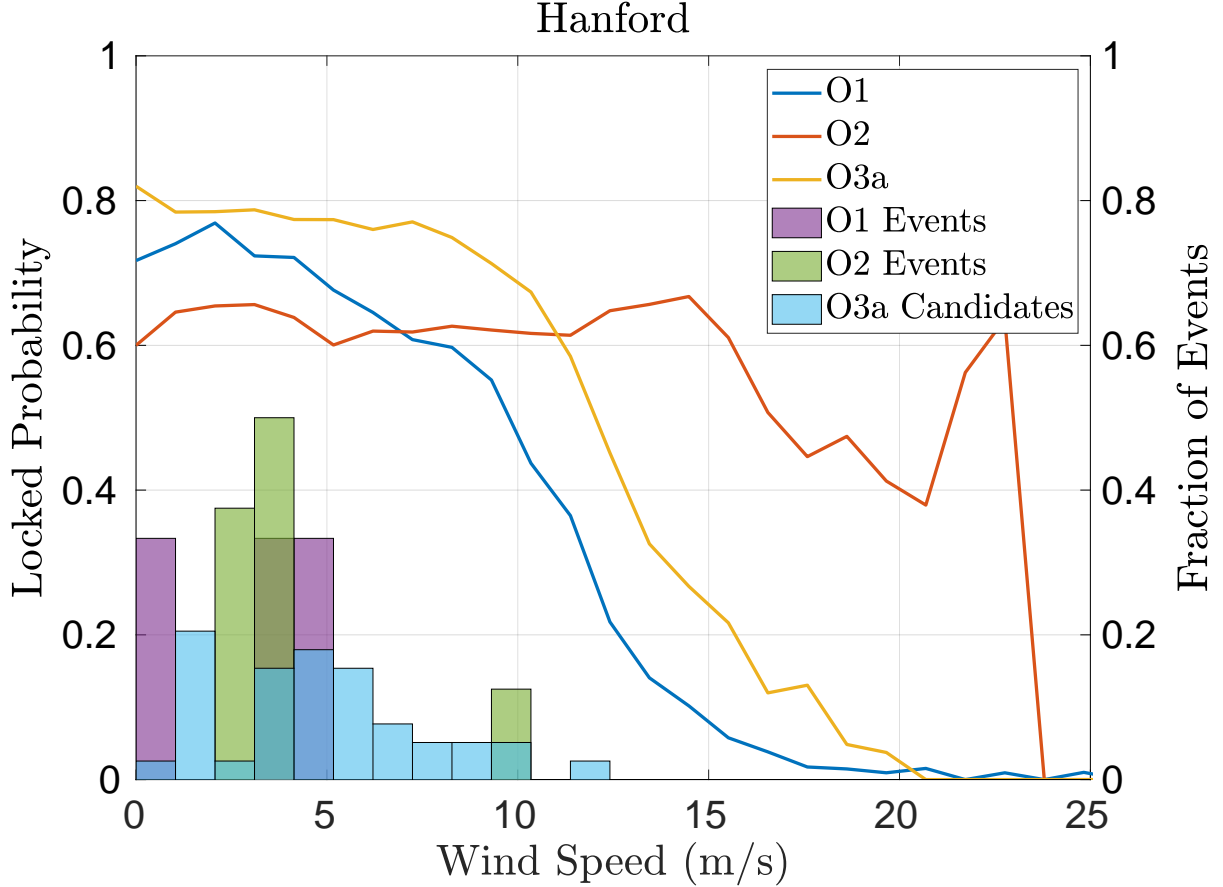
Figure 2.15: Duty cycle improvements for the LIGO Hanford Observatory along with distribution of observed events vs. wind speed.

The benefit of the tilt subtraction scheme can clearly be seen for Hanford between O1 and O2. During O1 the locked probability fell monotonically with wind speed, while for O2 the probability stayed relatively constant up to 15 m/s, above which it fell steadily. For O3a, Hanford saw a clear decrease in performance at high wind speeds yet still out performed the O1 scheme. This performance loss is likely due to the interferometer's Y-arm beam-spot being displaced away from the center of the test masses to avoid point absorbers on the Input-Y test mass. Displacements of the beam-spot are known to increase coupling between

the angular motion of the test mass and the length measured by the interferometer. This extra coupling increases the actuation needed to keep the interferometer locked, and thus increases the susceptibility of the system to seismic motion.

The decreased duty cycle of O2 at low wind speed is due to effects unrelated to seismic isolation or wind. If one applies a fudge factor to the O2 duty cycle in order to match the low wind speed performance of O1 and O3a, then this duty cycle equates to an observing time increase of 13.1 days per year between O1 and O2 and a decrease of 2.9 days/year between O2 and O3a.
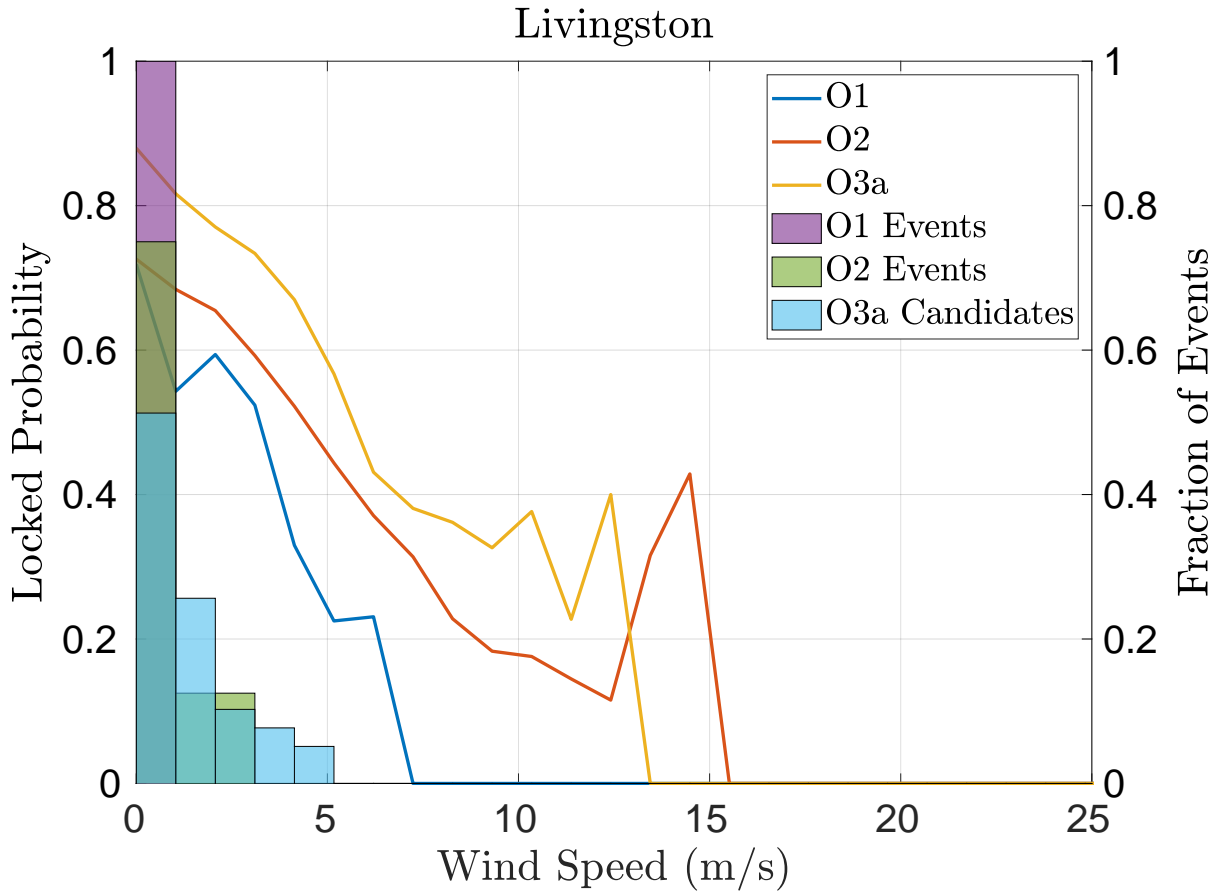
Figure 2.16: Duty cycle improvements for the LIGO Livingston Observatory along with distribution of observed events vs. wind speed.

Additionally, Figure 2.15 shows the fraction of the GW events or candidates detected during O1, O2, and O3a as a function of wind speed demonstrating that a collection of GW events were observed whose detection probability was enhanced by the increased duty cycle at higher wind speeds. Namely, GW170104 was measured at $\sim$11 m/s which had an increase in duty cycle of $\sim$20 % between O1 and O2. Additionally, a number of O3a candidates have been detected above $\sim$5 m/s at where the probability of being locked is increased by $\sim$20 %.
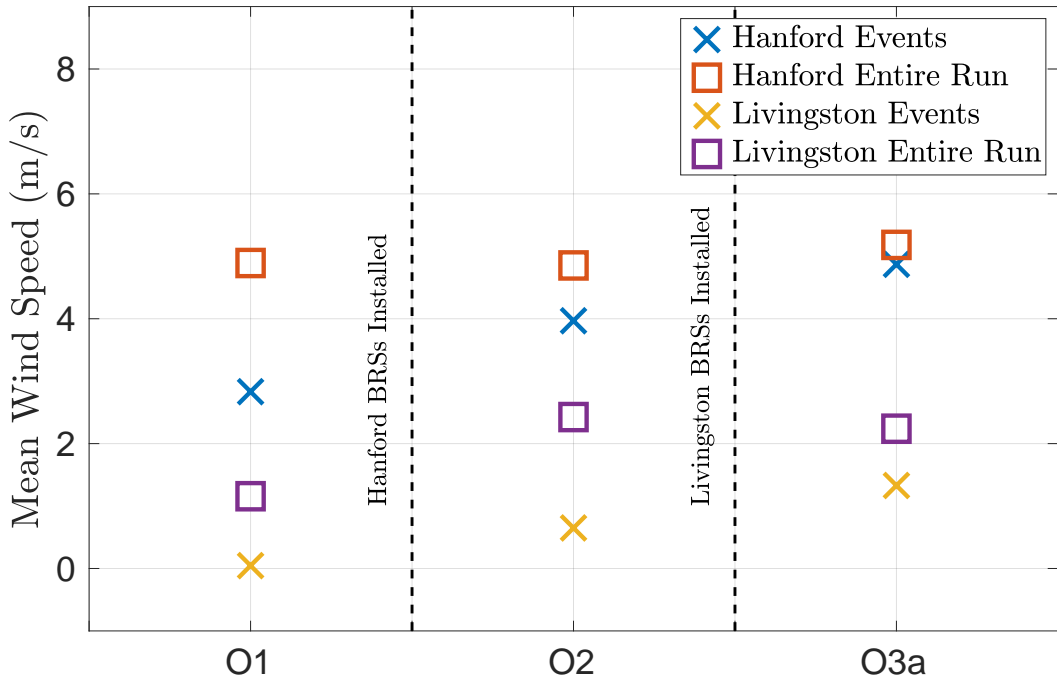
Figure 2.17: Mean wind speed during gravitational wave events and for each entire observing run.

At Livingston, the improvements at increased wind speeds, Figure 2.16, was less dramatic. Although between O1 and O2 tilt subtraction was not implemented, a increase in duty cycle was achieved by implementing a single seismometer for sensor correction for all of the corner station platforms. This change decreased the differential motion at higher wind speeds and

thus made the interferometer lock more robust. An additional increase in performance can be seen between O2 and O3a due to the deployment of tilt subtraction. However, the probability of being locked still dropped monotonically with wind speed, similar to the O1 performance of Hanford.

Despite this, there is a collection of O3a candidates detected between 3-6 m/s which were between 10-15% more probable with the increased robustness against wind speed. The enhanced duty cycle equates to an observing time increase of 13.9 days per year between O1 and O2 and 6.9 days/year between O2 and O3a for LLO.

An additional metric that quantifies the improved robustness of the interferometer is the mean wind speed during gravitational wave events. In the limit that the detection likelihood is independent of wind speed, one would expect that the mean wind speed during events would match that of the entire run. Figure 2.17 shows that each site approaches this limit with the installation of the BRSs.

Chapter 3

PROTOTYPE ON-BOARD ROTATION SENSOR

3.1   Angular Controls

To operate the LIGO interferometers in their optimal configuration, the relative angular motion of the test masses must be under 1 nrad RMS [36]. Although the seismic isolation system greatly attenuates the effect of ground motion, additional controls are needed to meet this requirement. The angular sensing and control system (ASC) consists of a number of optical sensors that are fed back to actuators on the quadruple pendulum. [36]

The rotational performance of the current seismic isolation system is limited at ∼0.2 Hz by the sensor noise of the seismometer pair that forms the isolation platform's angular sensors [31]. This couples into the residual translational motion due to tilt contamination as described in Section 2.1.1. To stop this motion from reaching the test masses, high-gain feedback loops are required on the downstream ASC system. These systems are limited by their respective sensor noise above ∼3 Hz. This left-over noise leaks into the gravitational wave band between 10 - 55 Hz due to the inability to sharply roll-off the sensor noise without interfering with the control at lower frequencies.

A model of the current ASC system is shown in Figure 3.1. This model combines modeled seismic platform motion, sensor noise spectra, transfer functions, and control loops to predict the residual angular motion of the test mass.[1] [37] The unity gain frequency (UGF) of the control is optimized to minimize residual angular motion above ∼10 Hz while maintaining RMS motion of 1 nrad/$\sqrt{\text{Hz}}$ at 10 mHz.

The compact Beam Rotation Sensor (cBRS), described in the following, was designed to be an alternative angular sensor for the seismic isolation system with ∼100-1000 times

---

[1]Model originally developed by Hang Yu. [37]
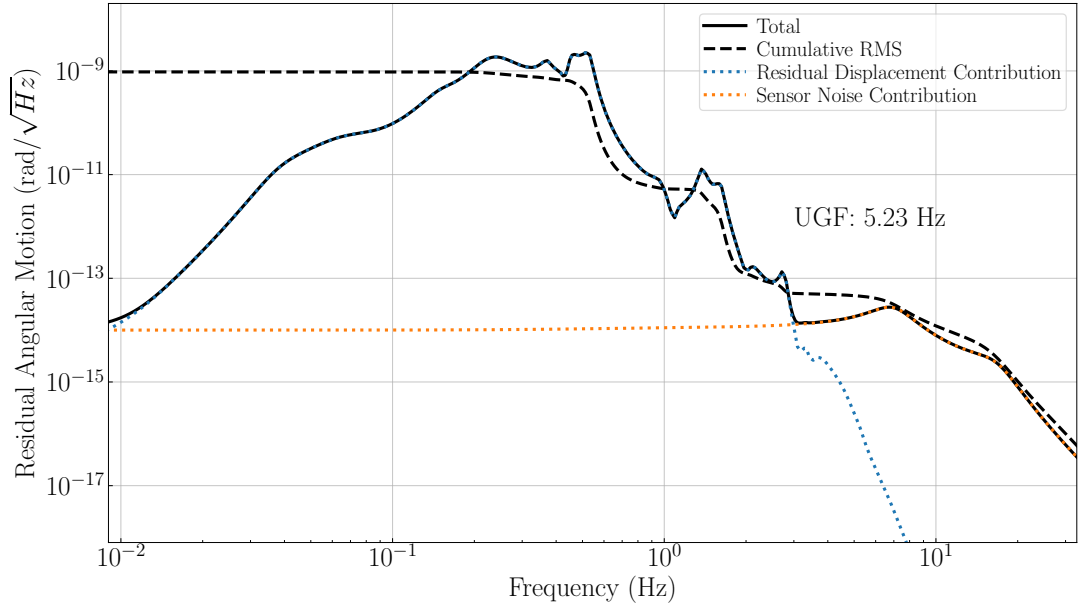
Figure 3.1: A model of the performance of the current angular sensing and control system. This model optimizes the unity gain frequency (UGF) of the ASC loop to maximize performance above ∼10 Hz while maintaining the low frequency RMS at 1 nrad/$\sqrt{\text{Hz}}$.

lower noise than the current sensors. Design sensitivity of the cBRS and the current angular sensor, a pair of GS13 seismometers, are shown in Figure 3.12. With a lower noise rotational sensor, the seismic isolation performance can be significantly increased in both the rotational and translational degrees of freedom. The angular performance couples to the translational through tilt contamination described in Section 2.1.1. Details of expected performance enhancement follow in Section 3.3.1. A decrease in residual angular motion would allow the ASC feedback to be retuned, specifically decreasing the UGF. This retuning is expected to decrease the ASC sensor noise leakage in the gravitational wave band.

Additional benefits are also expected to accompany the improved seismic isolation. These include decreased effects of scattered light and increased robustness against environmental
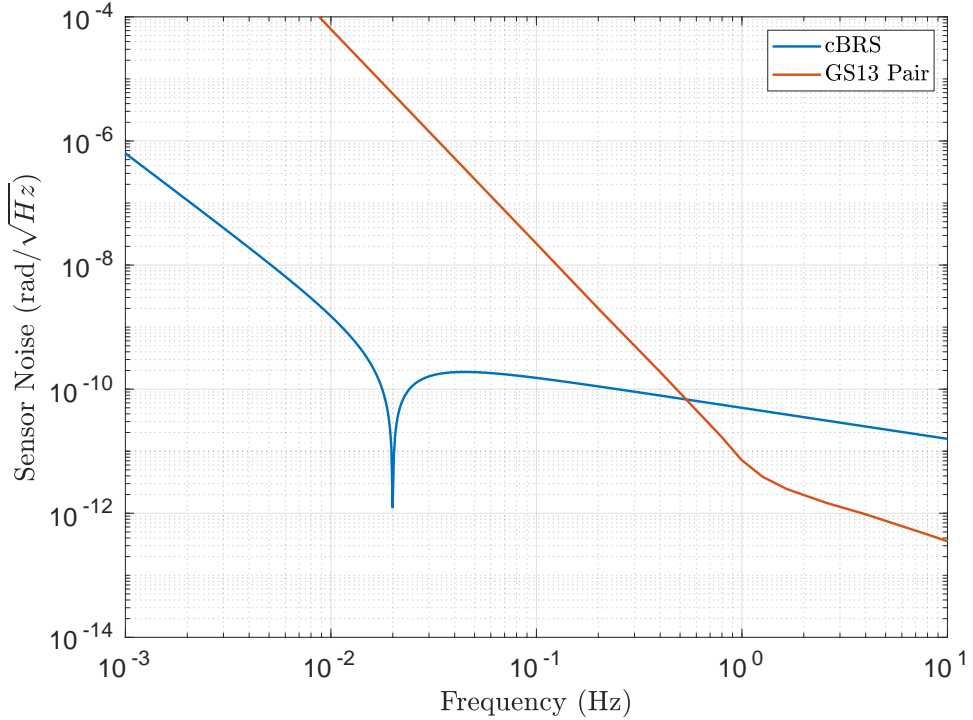
Figure 3.2: Theoretical sensor noise for the cBRS and seismometer pair located 1-m apart.

effects. A priori modeling of these effects is intractable but will be studied in detail with future installations.

3.2 Compact Beam Rotation Sensor

3.2.1 Mechanical System

The compact Beam Rotation Sensor (cBRS), shown in Figure 3.3-3.4, consists of a 30-cm long cross hung from 10-15 μm thick beryllium-copper flexure. It uses the same operating principle as the BRS: above the resonant frequency the balance acts as an inertial reference whose angle is measured with respect to the support. Thus Equations 2.7-2.10 also govern its mechanics. The cross shape of the balance decreases the sensitivity of the device to gradients in the local gravitational field while allowing for increased moment of inertia compared to a

similarly sized beam.

This design yields a moment of inertia of $I = 0.085$ kg m^2 and a resonant frequency of $\sim$20 mHz which limits the use of the device with high fidelity to frequencies above this. This resonant frequency does not allow this device to be used for ground tilt subtraction since the relevant ground tilts happen below 40 mHz.
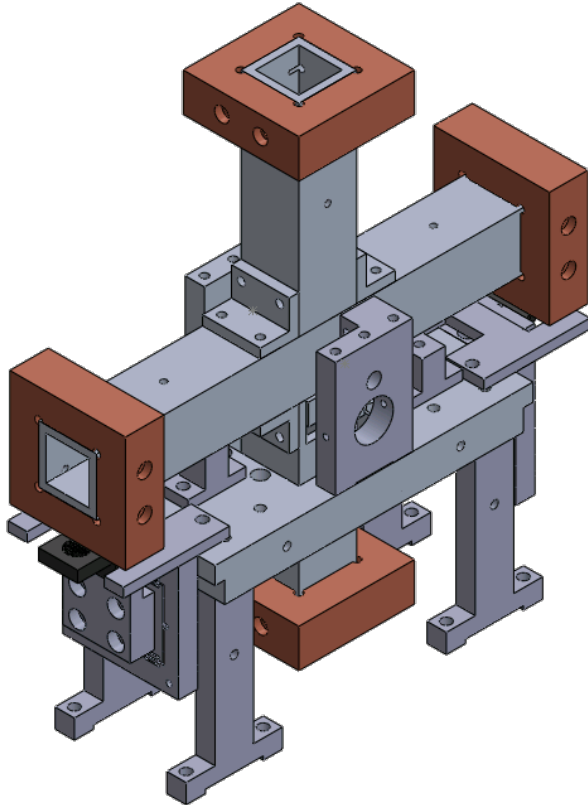
Figure 3.3: CAD rendering of the compact BRS (cBRS) showing the cross with its copper end masses which is hung from the flexures from the surrounding support structure. The translation stages which hold the fiber interferometer readouts can be seen on either end of the support below the two horizontal end masses.
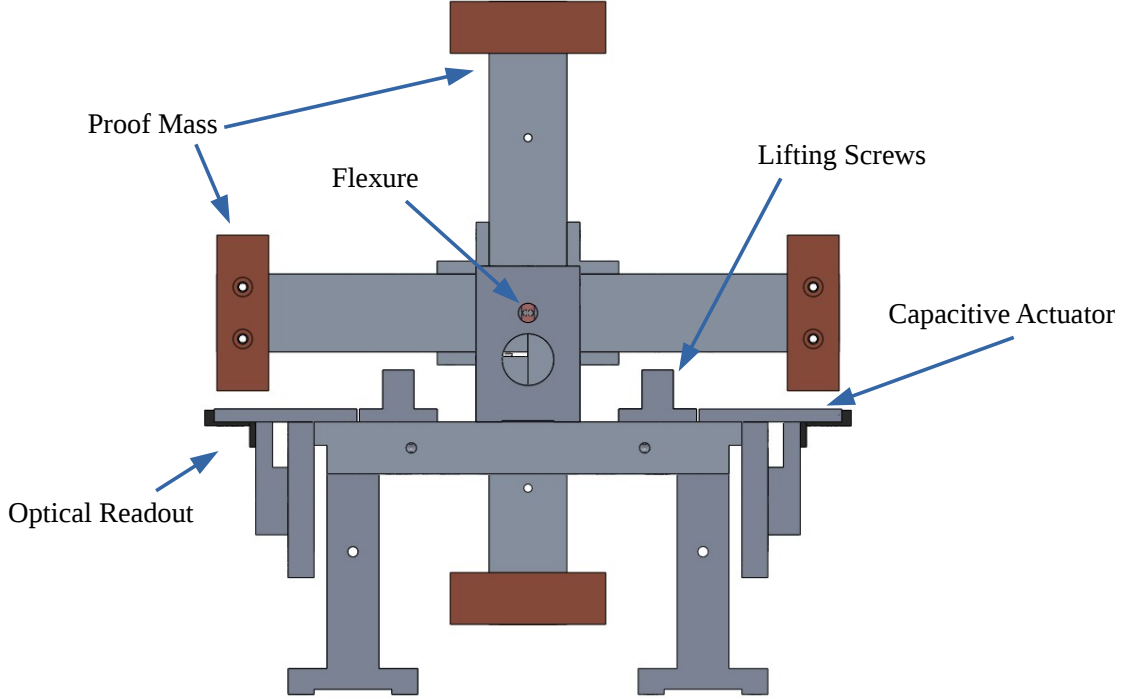
Figure 3.4: CAD rendering of the compact BRS (cBRS) showing the cross with its copper end masses which is hung from the flexures from the surrounding support structure. The translation stages which hold the fiber interferometer readouts can be seen on either end of the support below the two horizontal end masses.

3.2.2 Kinematic Mount

The proof mass is suspended via a kinematic mount, shown in Figure 3.5, to allow for ease of installation. The mount consists of three titanium spheres which are attached to the proof mass's horizontal beam and three pairs of titanium cylinders attached to the seat. This seat is suspended by flexures, described in Section 2.2.2. The spheres and cylinders are epoxied

in place to form an equilateral triangle.

This design allows clamping of the flexures, a delicate procedure, to be done with only the seat in place. After the seat is suspended the proof mass is lowered onto the seat by three lifting screws. The matching sets of spheres and cylinders define the proof mass's position relative to the flexures without over-constraining.
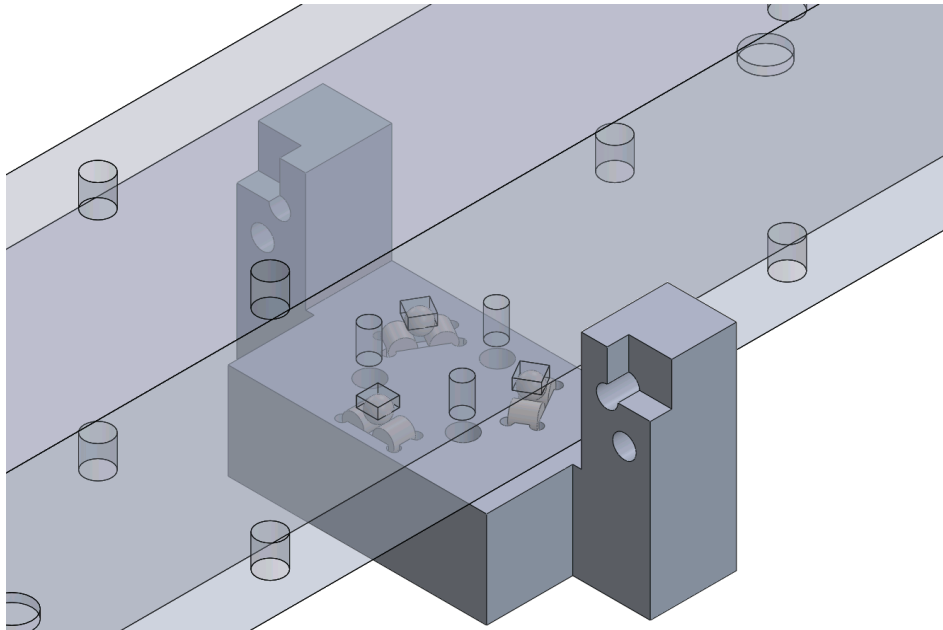
Figure 3.5: CAD rendering of the kinematic seat with the proof mass's horizontal beam transparent. The sets of spheres and cylinders which define the proof mass's position can be seen in the center of the seat. The flexures attach to the cut-outs on either side of the beam.

3.2.3   Interferometric Readout

An interferometric readout was developed in order to minimize the size of the device and to decrease readout noise. This system consists of a pair of Fabry-Perot cavities formed by a beamsplitter-coated optical-fiber and a full-reflecting mirror placed on the bottom of the balance's end masses, shown in Figure 3.6. The reflectance of this cavity is monitored by

employing a circulator to separate the ingoing and outgoing rays. The readout optics are schematically shown in Figure 3.7.
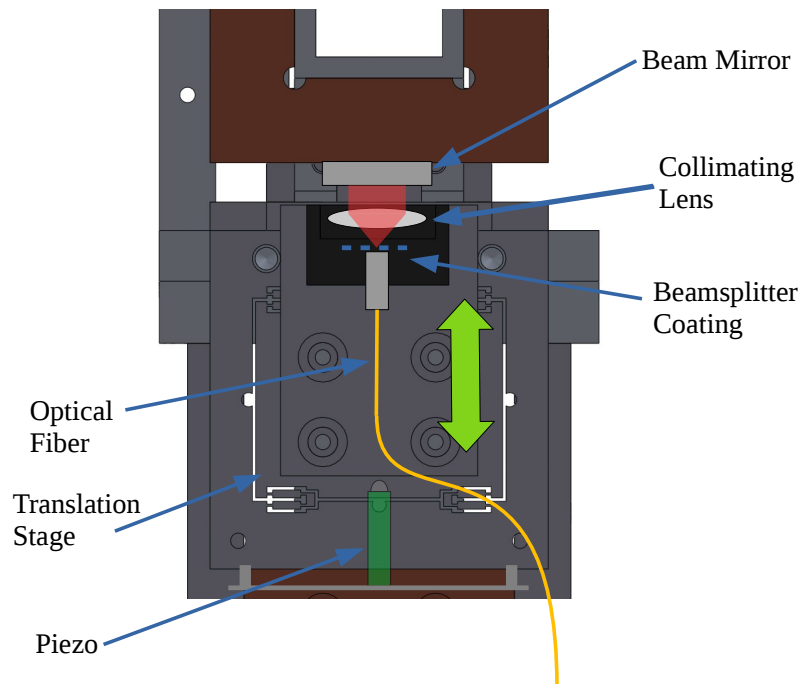
Figure 3.6: Diagram of the cBRS fiber interferometer read-head. The beamsplitter-coated optical fiber and collimating lens are attached to a translation stage. This stage is actuated by a piezo to maintain the length of the cavity.

As the cavity length changes the reflectence undergoes an interference pattern described by:

$$R = \frac{F \sin^2(2\pi nx/\lambda)}{1 + F \sin^2(2\pi nx/\lambda)} \tag{3.1}$$

where R is the reflectance, F is the finesse of the cavity, x is the length of the cavity, n is the index of refraction within the cavity, and λ is the wavelength.
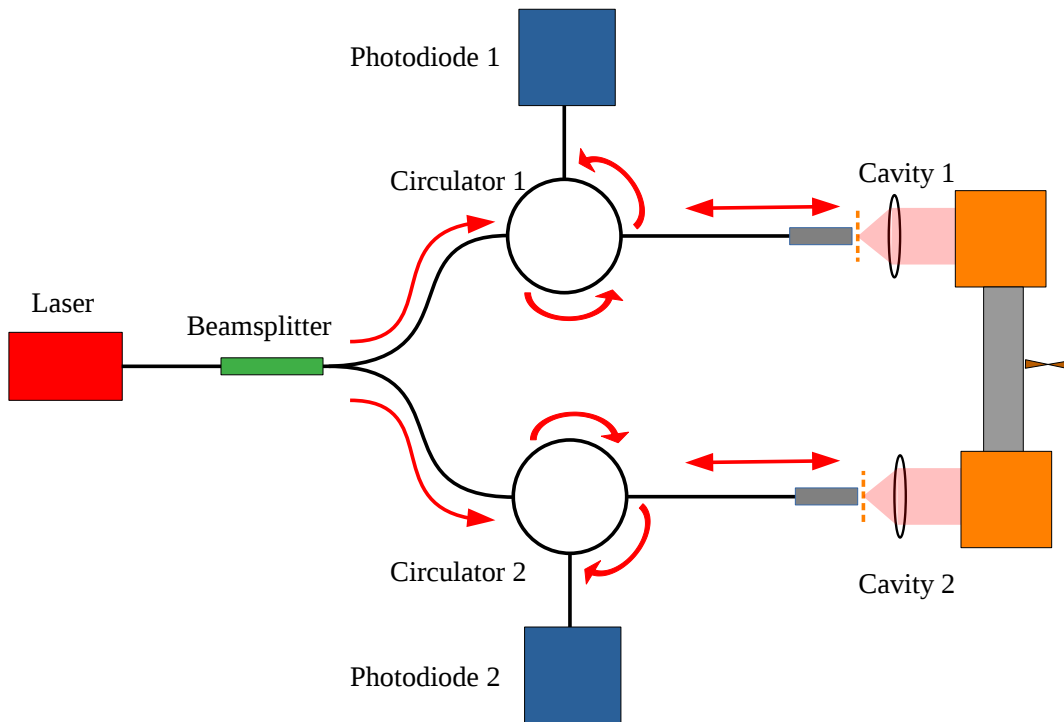
Figure 3.7: Layout of the cBRS readout optics. The light is emitted from a single fiber-coupled laser before being split into two paths. Each path consists of circulator, Fabry-Perot cavity, and a photodiode. The circulator sends light from the laser to the cavity and sends light returning from the cavity to the photodiode.

Parameter	Value
Laser	QPhotonics QDFBLD-1300-10
Wavelength	1310 nm
Fiber beamsplitter	Thorlabs TWQ1300HA
Circulator	Thorlabs CIR1310-APC
Fiber-tip beamsplitter	Thorlabs SMF28ER 50/50 FC/PC
Collimating focus	2.75 mm
Photodiode	Thorlabs PDA10CS InGaAs
Piezo	Tokin AE0505D16F
Piezo Max Range	17.4 μm at 150 V
Piezo Driver	PDu150 150 V

Table 3.1: Parameters of the cBRS interferometric readout.

The optical fiber tip and collimating lens are placed on a translation stage that is driven by a piezo stack. The intensity of the reflected light measured by the photodiode is fed back to the piezos using a PID loop. This feedback holds the cavity at fixed length allowing the system to be seperated into two linear readouts: the measured reflectance of the cavity for small ranges above the UGF of the loop and the displacement of the piezos for large motions below the UGF. The output of the readout is then the sum of these two channels.

In theory the angle of the beam can be measured with a single interferometer. However, two readouts are deployed, one at each end of the proof mass, in order to suppress common mode noise. The signal seen in each readout is described by:

$$\theta_1 = \theta_s + x_1/L + x_1\delta_\lambda/\lambda^2 + n_c + n_1 \tag{3.2}$$

$$\theta_2 = -\theta_s + x_2/L + x_2\delta_\lambda/\lambda^2 + n_c + n_2 \tag{3.3}$$

where $\theta_{1,2}$ are the angle equivalent signal seen in readout 1 and 2, θ_s is the sensed angle, $x_{1,2}$ are the length of the respective cavities, L is the arm length of the beam, δ_λ is the change in wavelength of the laser, λ is the wavelength of the laser, n_c is the sum of all unmodeled common noises, and $n_{1,2}$ represent any unmodeled noise that appears in one readout but not the other.

Since the angle of the beam appears with opposite sign in the two readouts, the difference between the two, Equation 3.4, contains the angle while suppressing common noise. The most notable source of common noise is frequency fluctuations of the laser. This couples to the angular readout through the mismatch in the average cavity lengths which are matched to within 1 mm. On the other hand, the sum of the two channels, Equation 3.5, contains no contribution from the angle but is comprised of only noise sources. This channel allows for the in-situ estimate of the sum of noises.

$$\Delta\theta = 2\theta_s + (x_1 - x_2)\delta_\lambda/\lambda^2 + n_1 - n_2 \tag{3.4}$$

$$\Sigma\theta = (x_1 + x_2)/L + (x_1 + x_2)\delta_\lambda/\lambda^2 + 2n_c + n_1 + n_2 \tag{3.5}$$

3.2.4   Calibration

The two readouts are calibrated independently to account for differences in piezo calibration and amplifier gains. The calibration is done by driving the piezo linearly through its entire range while the beam is mechanically locked. During this drive the interference pattern wraps through multiple fringes as the cavity length is decreased. The minima of these fringes are separated by $\lambda/2$ which allows for the voltage across the piezo to be converted into displacement. The region around the 50% reflectance point, which is the operating point of the interferometer, is then fit to a linear function of displacement to yield a conversion from reflectance intensity to displacement.

This calibration scheme requires independent determination of the wavelength of the light which is specified by the laser manufacturer to be 1310 nm $\pm$ 0.01 nm. Additionally, the pattern seen at the photodiode must be the interference due to the Fabry-Perot cavity
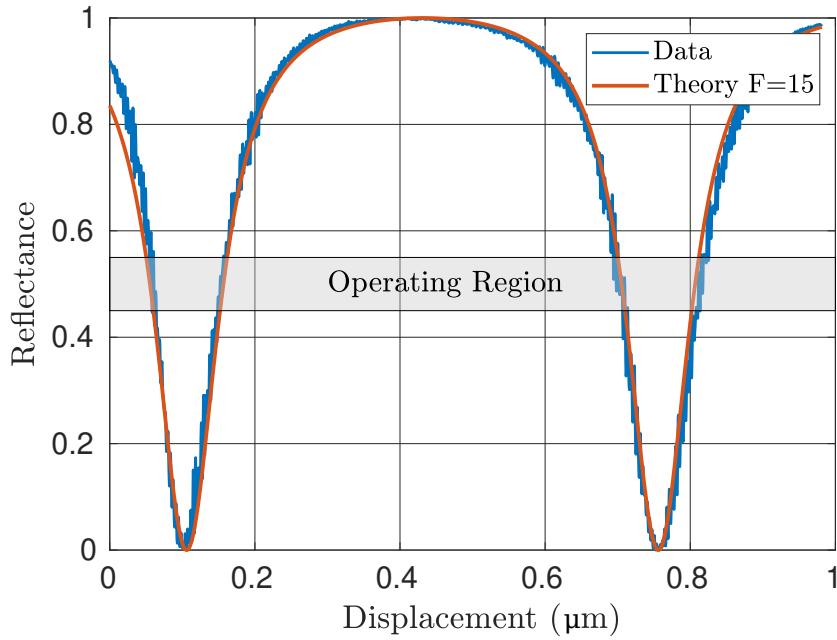
Figure 3.8: Interference pattern of a cBRS fiber interferometer vs cavity length. The gray region is where the device is operated in normal conditions. Within this region the reflectance is approximately linear verse displacement.

and not due to parasitic interference. A comparison of the reflectance measurements and the theory for a can be seen in Figure 3.8 which verifies that the interference is due to the Fabry-Perot cavity.

3.2.5 Mass Adjustment

Both the BRSs and the cBRS can undergo long term drifts of the equilibrium position that can drive the beam-balance past the dynamic range of the readout. To counteract this, mass on the balance can be moved or added to shift the horizontal center of mass. The change in equilibrium angle due to the shifting of a small mass follows:

$$\Delta\theta = \frac{g}{\kappa}m\Delta r \tag{3.6}$$

where $\Delta\theta$ is the change in equilibrium angle, g is the gravitational acceleration, κ is the spring constant of the flexure, m is the shifted mass, and Δr is the change in horizontal distance.
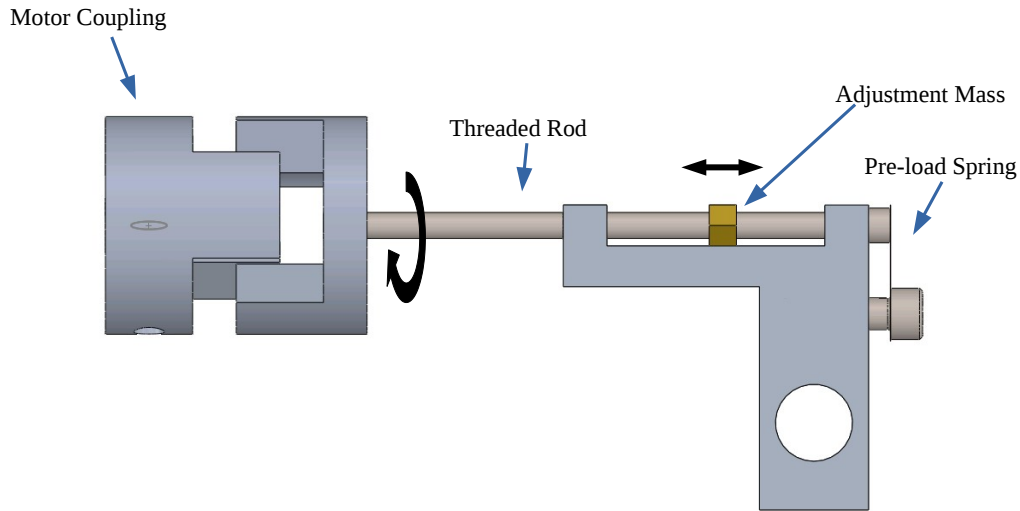
Figure 3.9: CAD rendering of the cBRS mass adjuster. When the center of mass needs to be adjusted a motor can rotate the threaded rod which shifts the mass horizontally. Once the mass adjustment is done the motor can rotate in the reverse direction to decouple from the mass adjuster.

While for the BRS the horizontal center of mass (COM) was designed to be tuned by hand, the cBRS is designed to operate within the LIGO vacuum chambers. Thus any mass adjustment must be done remotely and in an automated fashion. A mass adjuster, shown in Figure 3.9, was designed to achieve this requirement. The adjuster consists of a small brass mass on a fine pitched threaded rod attached to the beam-balance. This device allows the

mass to be shifted by rotating the threaded rod.

The motor which turns this screw is held on an independent support to avoid mechanically shorting the beam balance with wires. The couplers between the motor and the screw are intentionally over-sized to allow the motor to decouple by rotating in-reverse once the actuation is complete. A small shim of beryllium copper is held tightly against the opposite end of the screw to provide spring loading. The spring restricts the threaded rod's horizontal motion while allowing for rotation.
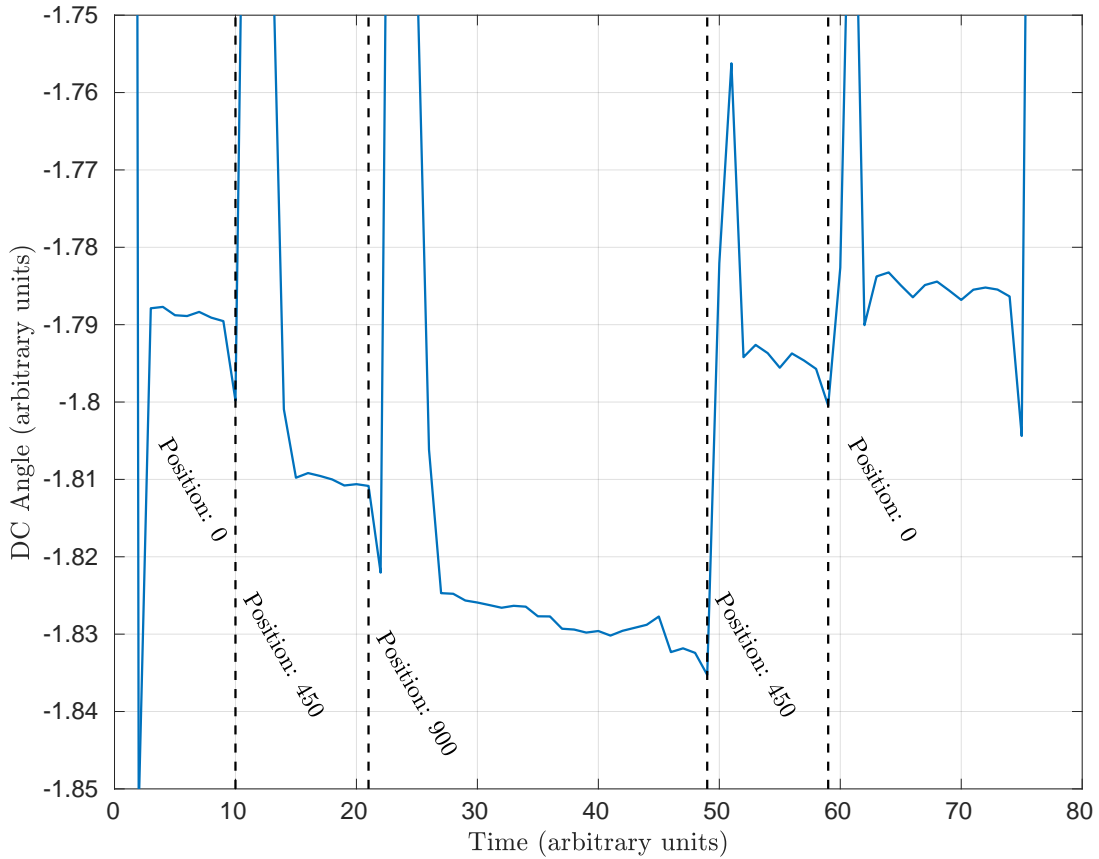
Figure 3.10: Demonstration of the effect of actuating the remote mass adjuster. The DC angle was measured by taking the mean of period long chunks of shadow sensor data while the mass adjuster was shifted to a collection of positions.

A temporary, uncalibrated shadow sensor was installed which measured the motion of the cBRS to test whether this design was capable of shifting the horizontal COM accurately. Figure 3.10 shows the average of period long cuts of the cBRS's resonant motion during the actuation of the mass adjuster. There is clear hysteresis due to nonuniform friction along the length of the adjuster. However, this did not affect the ability to center the cBRS.

3.2.6 Controls

The cBRS can be rung up by environmental transients that cause resonant motion in excess of the readout's dynamic range. These amplitudes are decreased by two capacitive actuators placed under the end masses of the beam. The angular-readout, band-passed around the resonant frequency, is fed back to these actuators with low gain. This feedback decreases the observed quality factor[2], $Q_{\rm obs}$, of the beam-balance and can be toggled off when high $Q_{\rm obs}$ motion is desired.

3.2.7 Noise Performance

The performance of the cBRS prototype is shown in Figure 3.11 along with its measured readout noise and design sensitivity.

The readout noise was measured with the proof mass lifted off of the kinematic seat and mechanically locked in place. These measurements yield a noise floor of 70 $\mathrm{prad}/\sqrt{\mathrm{Hz}}$ at 5 Hz and 30 $\mathrm{prad}/\sqrt{\mathrm{Hz}}$ at 25 Hz. This noise rises at low frequencies to 2 $\mathrm{nrad}/\sqrt{\mathrm{Hz}}$ at 0.1 Hz. This rise is suspected to be due to mechanical stressing of the optical fibers sourced by temperature variations.

The design sensitivity was determined by extrapolating the angular-equivalent noise achieved by a prototype readout. This noise gives a raw angular readout noise of 50 $\mathrm{prad}/\sqrt{f}$ which was multiplied by the $\tilde{\theta}_s$ to $\tilde{\theta}_p$ transfer function, Equation 2.10, to yield an inertial-equivalent sensitivity.

---

[2]The observed quality factor was obtained by measuring the ring down of excited resonant motion. This quality factor is due to the combination of intrinsic and external losses.
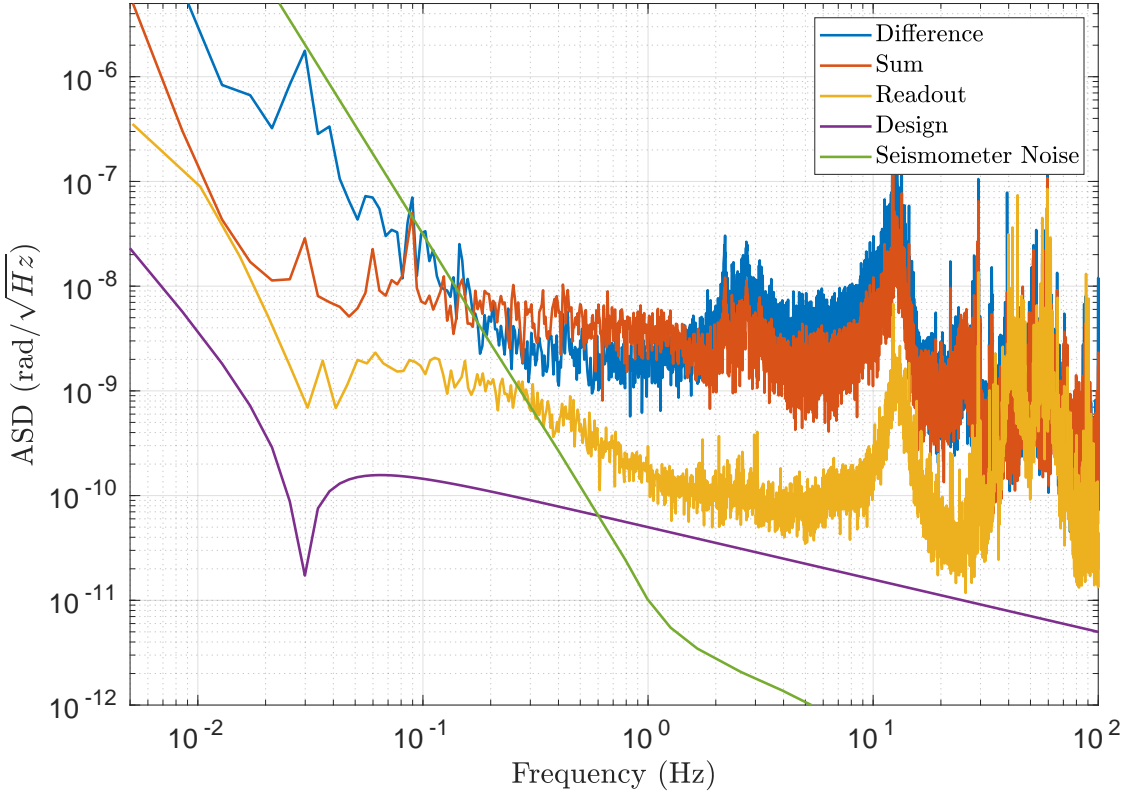
Figure 3.11: Prototype cBRS noise performance showing the sum and difference of the two readouts. Additionally shown are the readout noise measured while the beam balance was mechanically locked, the design sensitivity, and the sensitivity of the current Stage 2 rotational sensors.

Comparison of the sum and difference spectra show a factor of ∼2 suppression of common noise between 0.3-1.5 Hz. Below 0.1 Hz, the device senses angular motion ∼100 larger than the sum of noises. This angular motion could be due to either external torques acting on the balance or angular motion of the bench on which it sat. The peak at ∼12 Hz is due to the resonant mode of the experimental bench and the collection of peaks between 20-100 Hz are suspected to be acoustic pick up of the instrument.

Further identification and elimination of noise sources was halted due to the onset of

the coronavirus pandemic. However, improvements are expected with the future addition of thermal insulation, mitigation of electrostatic torques, and improvements to the read-head translation stages.

3.3 Projected Improvements

3.3.1 Isolation Scheme

As described in Section 1.3, each stage and degree of freedom of the seismic isolation system utilizes a blend of multiple sensors as its feedback signal. These consist of two types of sensors: position sensors which sense differential motion between two stages and inertial sensors which sense the motion relative to an inertial frame. We constructed a simplified two stage, two degree of freedom model of the seismic isolation to assess the performance improvements that could be achieved with the addition of a cBRS.

This model assumes both infinite control authority and no dynamics of the isolation platforms. Additionally, purely theoretical models are used for the input motion and the sensor noises. Although a model which accounts for all six degrees of freedom is required to accurately predict the isolation performance, this simplified model is instructive for comparisons of the performance with and without the cBRS. Similar models [31] have been found to match measurements to within a factor of $\sim$2-3.

Throughout this model second-order binomial filters are used as the blend filters. In addition, for each stage the inertial sensor noise is taken to be the minimum of the collection of inertial sensors. Realistically these sensors also require precise blending but the details of this blending is negligible below $\sim$0.5 Hz. Figure 3.12 shows the noise curves for each sensor used in this model.

Stage 2 Rotational

We choose to model a cBRS on the second stage of the isolation as this placement minimizes the suspension point motion. Logistically, this location also has enough space to install a
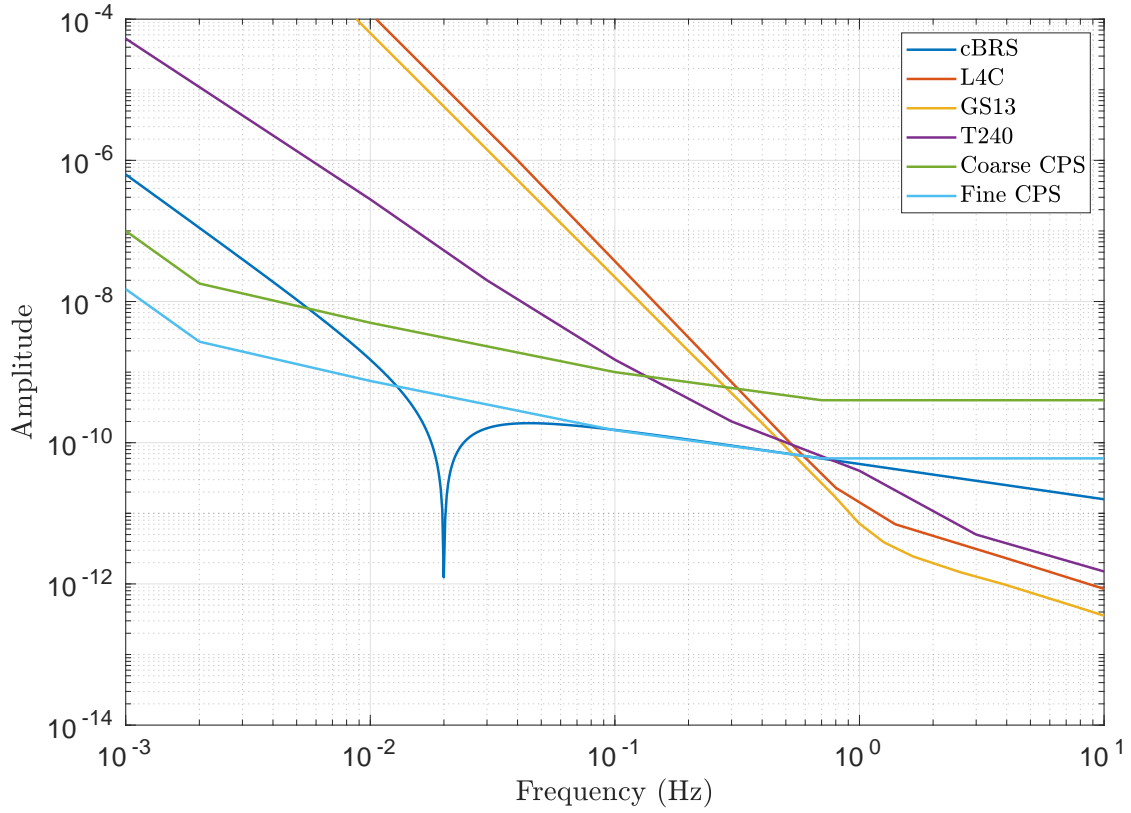
Figure 3.12: Noise models for the cBRS, a collection of seismometers: L4C, GS13, T240, and two types of CPS: Fine, used between Stage 1 and Stage 2, and Course, used between Stage 0 and Stage 1. Each sensor is in its native units, seismometers and CPS in meters and cBRS in radian. Note that a pair of translational sensors located 1 m apart has roughly the same noise level in either meters or radians.

device without modifying the current ISI platform. Due to the rising low frequency noise in the cBRS, placement of the blend frequency becomes a balance of increasing motion at low frequencies and decreasing motion at high, and visa versa. The blend frequency was chosen to give a low frequency RMS motion of $\sim$10 nrad/$\sqrt{\text{Hz}}$ which matches the performance without the cBRS, see Figure 3.17. This criterion called for a blend frequency of 12 mHz.

The residual tilt for Stage 2 can be approximated by:

$$\tilde{\theta}_2(\omega) \approx \hat{F}_{LP2}\left(\tilde{\theta}_1(\omega) + \hat{n}_{\text{CPS-F}}(\omega)\right) + \hat{F}_{HP2} \min\left[\hat{n}_{\text{cBRS}}(\omega),\ \hat{n}_{\text{GS13}}(\omega)\right] \tag{3.7}$$

where $\tilde{\theta}_1$ is the tilt of Stage 1, $\hat{F}_{LP2}$ and $\hat{F}_{HP2}$ are respectively the Stage 2 rotational low-pass and high-pass blend filters, $\hat{n}_{\text{CPS-F}}$, $\hat{n}_{\text{cBRS}}$, and $\hat{n}_{\text{GS13}}$ are the rotational sensor noise for the Fine CPS, cBRS, and GS13, respectively. The performance with this loop can be seen in Figure 3.13. Above ~500 mHz, the performance is dominated by the GS13 noise and from 80 mHz to 500 mHz it is dominated by cBRS noise. Below 80 mHz, the position sensor contributions become dominant which makes the Stage 2 motion almost equal to the Stage 1 motion. The only deviation from Stage 1 motion is near the blend frequency, 12 mHz, where gain peaking added a factor of ~ 3.

Stage 1 Rotational

With Stage 2 inertially isolated in the rotation degree of freedom above ~80 mHz, Stage 1 can achieve superior performance if its control is a combination of the position sensor between Stage 1 and Stage 2 (Fine CPS) at high frequencies, and the position sensor between Stage 1 and Stage 0 (Course CPS) at low. This method is effectively using the Stage 2 platform as an inertial proof mass with the Fine CPS as a readout. The past scheme was to use a seismometer pair as an inertial rotation sensor for high frequencies and the Course CPS at low. Applying the same criterion as Stage 2 of requiring low frequency RMS motion of ~10 nrad/$\sqrt{\text{Hz}}$ yields a blend frequency of 3 mHz around which the motion is amplified by a factor of ~ 3 because of gain peaking.

The residual tilt for Stage 1 can be approximated by:

$$\tilde{\theta}_1(\omega) \approx \hat{F}_{LP1}\left(\tilde{\theta}_g(\omega) + \hat{n}_{\text{CPS-C}}(\omega)\right) + \hat{F}_{HP1} \min\left[(\hat{n}_{\text{cBRS}}(\omega) + \hat{n}_{\text{CPS-F}}(\omega)),\ \hat{n}_{\text{T240}}(\omega)\right] \tag{3.8}$$
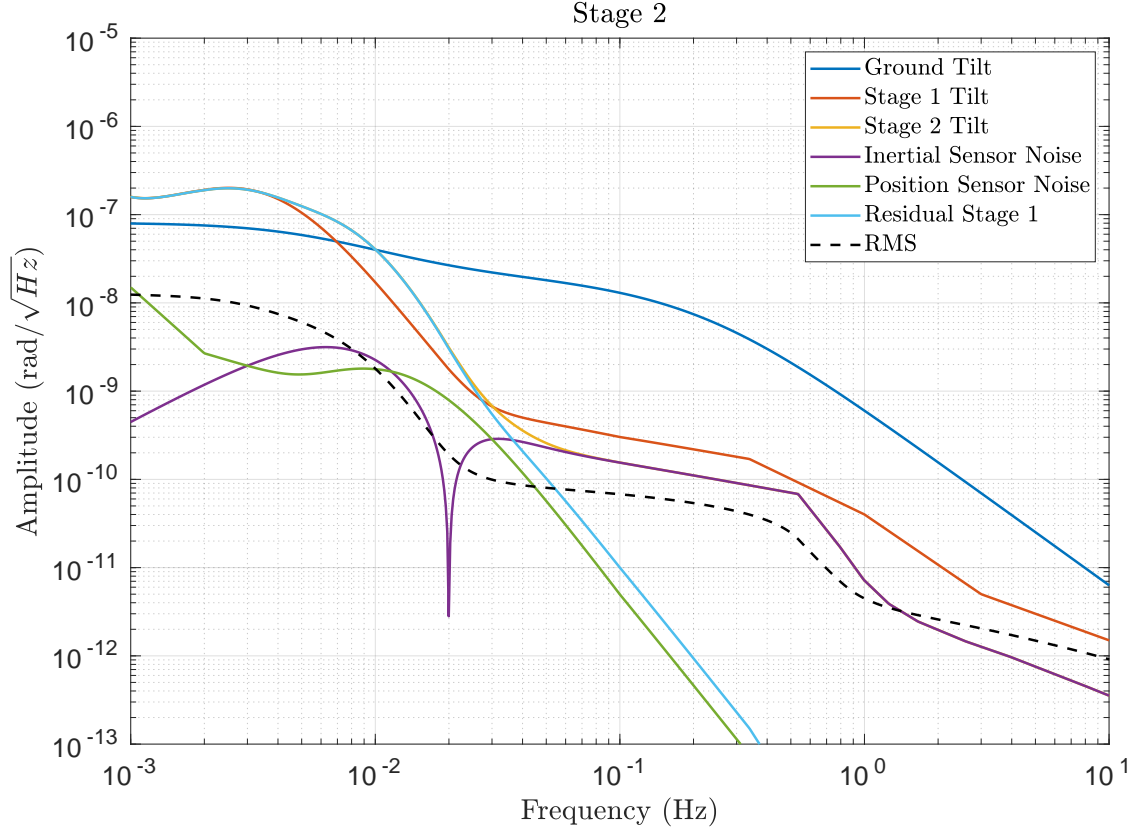
Figure 3.13: Projected rotational performance of Stage 2 along with contributions from residual Stage 1 tilt and sensor noises. Also shown is the input ground tilt model which represents the observed tilt during windy times and the rotational performance of Stage 1.

where $\tilde{\theta}_g$ is the ground tilt, $\hat{F}_{LP1}$ and $\hat{F}_{HP1}$ are respectively the Stage 1 rotational low-pass and high-pass blend filters, $\hat{n}_{\text{CPS-C}}$, $\hat{n}_{\text{CPS-F}}$, $\hat{n}_{\text{cBRS}}$, and $\hat{n}_{\text{T240}}$ are the rotational sensor noise for the Course CPS, Fine CPS, cBRS, and T240, respectively.

The performance of this design can be seen in Figure 3.14. Below 1 mHz, it is expected that the platform motion follows the ground. However, this is omitted as both the ground rotation and sensor noise are not well constrained below 1 mHz. Above ~30 mHz, the residual is dominated by the combination of the sensor noises from the Fine CPS, from 30 mHz to 350 mHz, and the T240 pair, above 350 mHz.
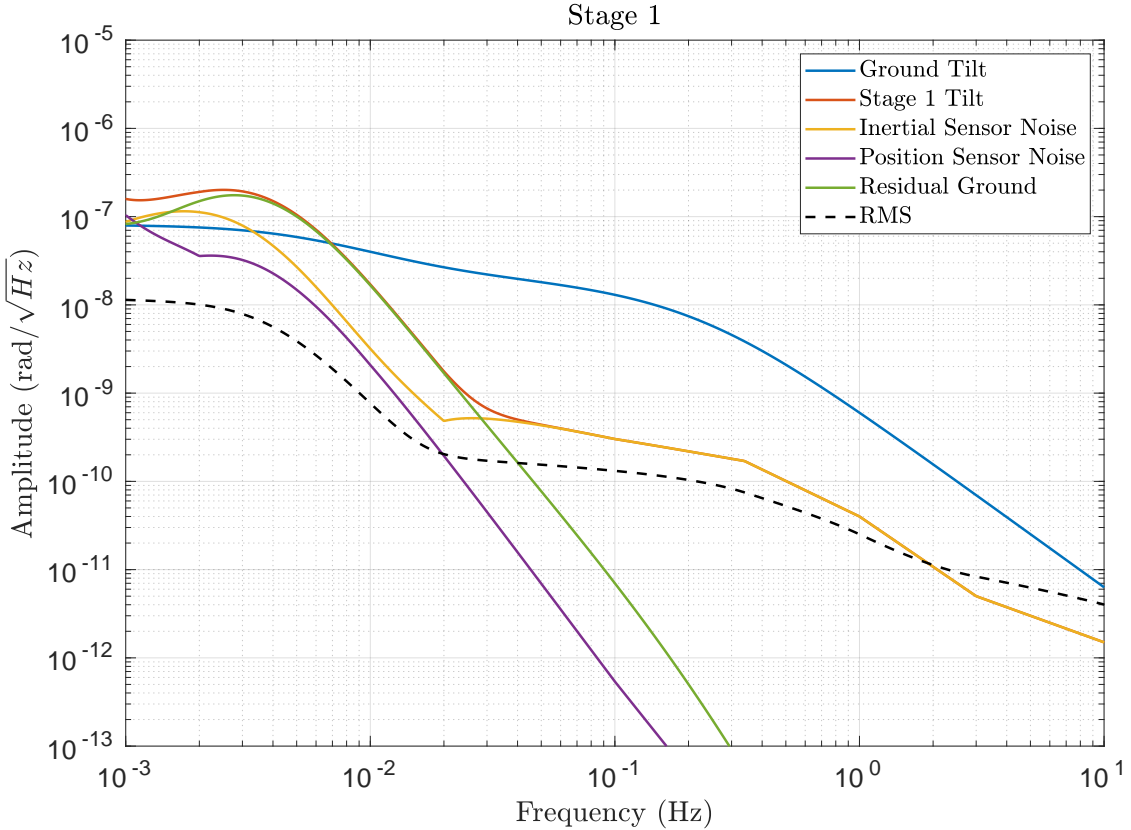
Figure 3.14: Projected rotational performance of Stage 1 along with contributions from sensor noises and residual ground tilt. Also shown is the input ground tilt model which represents the observed tilt during windy times.

A subtlety arises from using both the Fine CPS and Course CPS as the control for Stage 1. If the Stage 2 blend frequency is placed below the Stage 1 blend frequency then in between these two frequencies both stages are using the Fine CPS as their control. Since the Fine CPS measures the motion between the two stages, this effectively makes both stages uncontrolled as they are not referenced to any independent frame. In our model this is avoided by placing the Stage 1 blend frequency a decade lower than the Stage 2 blend.

Figure 3.15: Projected translational performance of Stage 1 along with contributions from residual ground motion, residual Stage 1 tilt, and sensor noise. The control loops here can be tuned to decrease motion at ∼100 mHz, the microseism frequencies, by increasing motion at ∼10 mHz, and vice versa.

Stage 1 Translational

Once the rotational degrees of freedom are controlled, the translational loops can be tuned. The translational isolation is dependent on the rotational performance due to tilt contamination of the seismometers, described in Section 2.1.1. Again, the choice of blend frequency is a trade off between increasing low frequency motion and decreasing motion at high frequency. We choose to require low frequency RMS performance of < 100 nm/s/$\sqrt{\text{Hz}}$. This requirement is approximately the performance of the current seismic isolation system. A

blend frequency of 15 mHz was found to exceed this requirement.

The residual motion for Stage 1 can be approximated by:

$$\tilde{x}_1(\omega) \approx F_{LP1}\left(\tilde{x}_g(\omega) + \tilde{n}_{\text{CPS-C}}(\omega)\right) + F_{HP1}\left(g/\omega^2\,\tilde{\theta}_1(\omega) + \tilde{n}_{\text{T240}}(\omega)\right) \qquad (3.9)$$

where $\tilde{x}_g$ is the ground motion, F_{LP1} and F_{HP1} are respectively the Stage 1 translational low and high-pass blend filters, and $\tilde{n}_{\text{CPS-C}}$ and $\tilde{n}_{\text{T240}}$ are the translational sensor noise for the Course CPS and T240, respectively.

The performance of the Stage 1 translational isolation is shown in Figure 3.15. Above 500 mHz, the performance is limited by the T240 noise. Between 25-500 mHz, residual ground motion dominates and between 1-25 mHz residual tilt coupled is the primary contribution.

Stage 2 Translational

The Stage 2 translational loops were tuned in a similar manner as Stage 1: requiring that the RMS motion at 1 mHz to be < 100 nm/s/$\sqrt{\text{Hz}}$. This yielded a blend frequency of 45 mHz. The residual motion for Stage 2 can be approximated by:

$$\tilde{x}_2(\omega) \approx F_{LP2}\left(\tilde{x}_1(\omega) + \tilde{n}_{\text{CPS-F}}(\omega)\right) + F_{HP2}\left(g/\omega^2\,\tilde{\theta}_2(\omega) + \tilde{n}_{\text{GS13}}(\omega)\right) \qquad (3.10)$$

where F_{LP2} and F_{HP2} are respectively the Stage 2 translational low-pass and high-pass blend filters, and $\tilde{n}_{\text{CPS-F}}$ and $\tilde{n}_{\text{GS13}}$ are the translational sensor noise for the Fine CPS and GS13, respectively.

The performance of this loop is shown in Figure 3.16. This choice of blend frequency effectively flattens the residual spectrum between $\sim$5-60 mHz to an amplitude of 2-3 $\times 10^{-7}$ m/s/$\sqrt{\text{Hz}}$ while decreasing the microseism at 150 mHz by a factor of $\sim$100.

The limiting term of the Stage 2 translational performance in these models is the noise due to the on-platform inertial sensors whereas previous performance was dominated by the tilt contamination term. [31] This expresses the need for low-noise inertial translation sensors for future systems which is an active area of research with many promising candidate

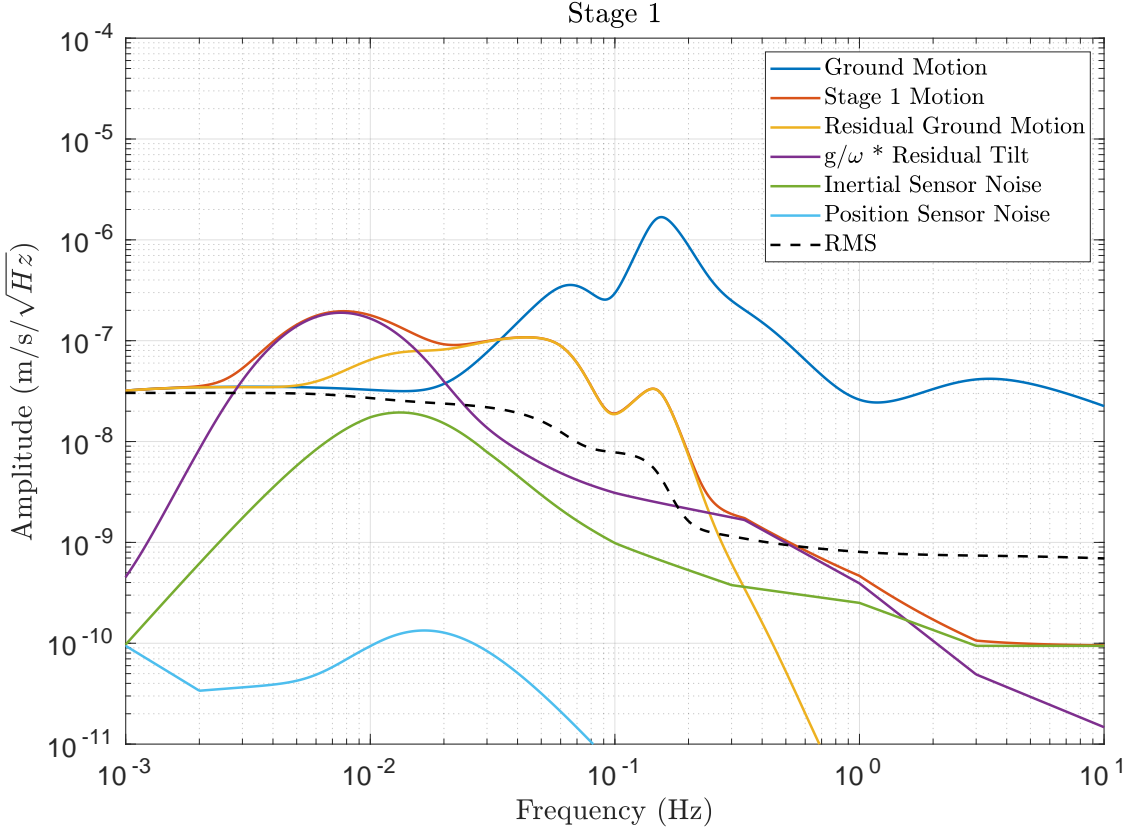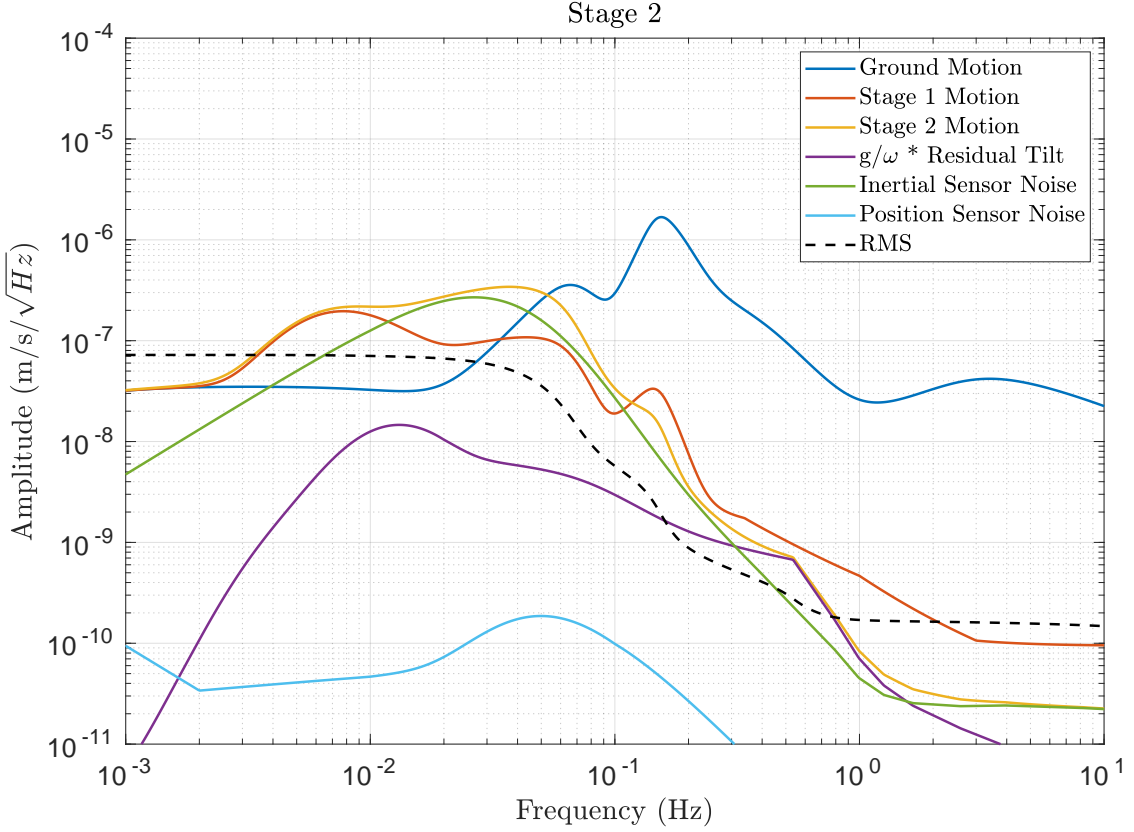Figure 3.16: Projected translational performance of Stage 2 along with contributions from residual Stage 1 motion, residual Stage 2 tilt, and sensor noise. The control loops here can be tuned to decrease motion at ~100 mHz, the microseism frequencies, by increasing motion at ~10 mHz, and vice versa.

sensors [38, 39].

Comparison with past performance

The performance of the past isolation system was modeled using the same techniques as described in Section 3.3.1 to compare with the proposed configuration. The filters used in the past model were those that were deployed for O2. These are expertly tuned to account for the true performance of the instruments and thus have complex shapes. However, they

follow the same general outline as the filters used in the proposed scheme.
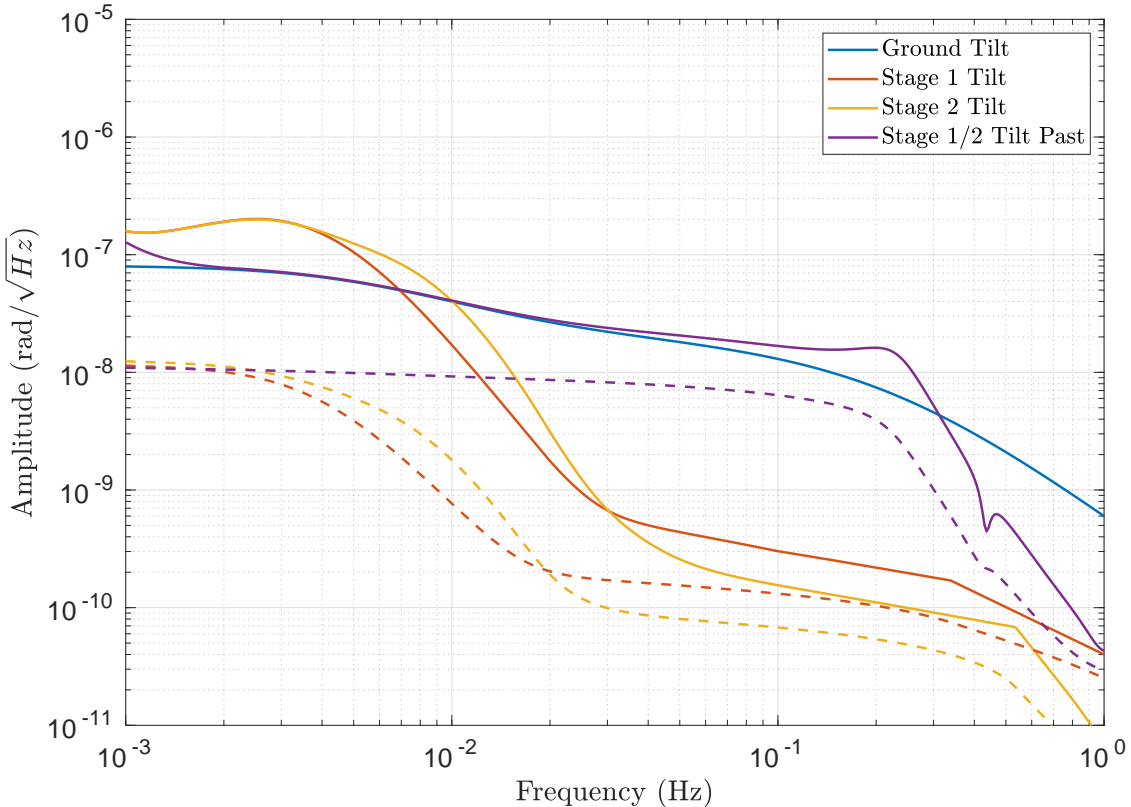
Figure 3.17: Comparison of the rotational isolation performance of Stage 2 during O2 and the projected performance with the inclusion of the cBRS. The dashed lines indicate the RMS of each curve. During O2, the rotational performance of the two stages was identical since they were locked together using the position sensors.

A comparison of the rotational performance is shown in Figure 3.17. During O2, Stage 2 was locked to Stage 1 using the position sensors in the rotational degree of freedom across the entire band of interest. Thus the performance of the two stages was identical. With the addition of the cBRS the residual tilt is decreased by a factor of ∼50 and ∼100 respectively for Stage 1 and Stage 2 between 50-250 mHz. Between 1-10 mHz the residual tilt is increased by a factor of ∼3. Below 1 mHz it is expected that the two schemes have identical performance.

However, this is omitted from the model as the ground tilt is not well known below 1 mHz due to the lack of sub-mHz rotation sensors.
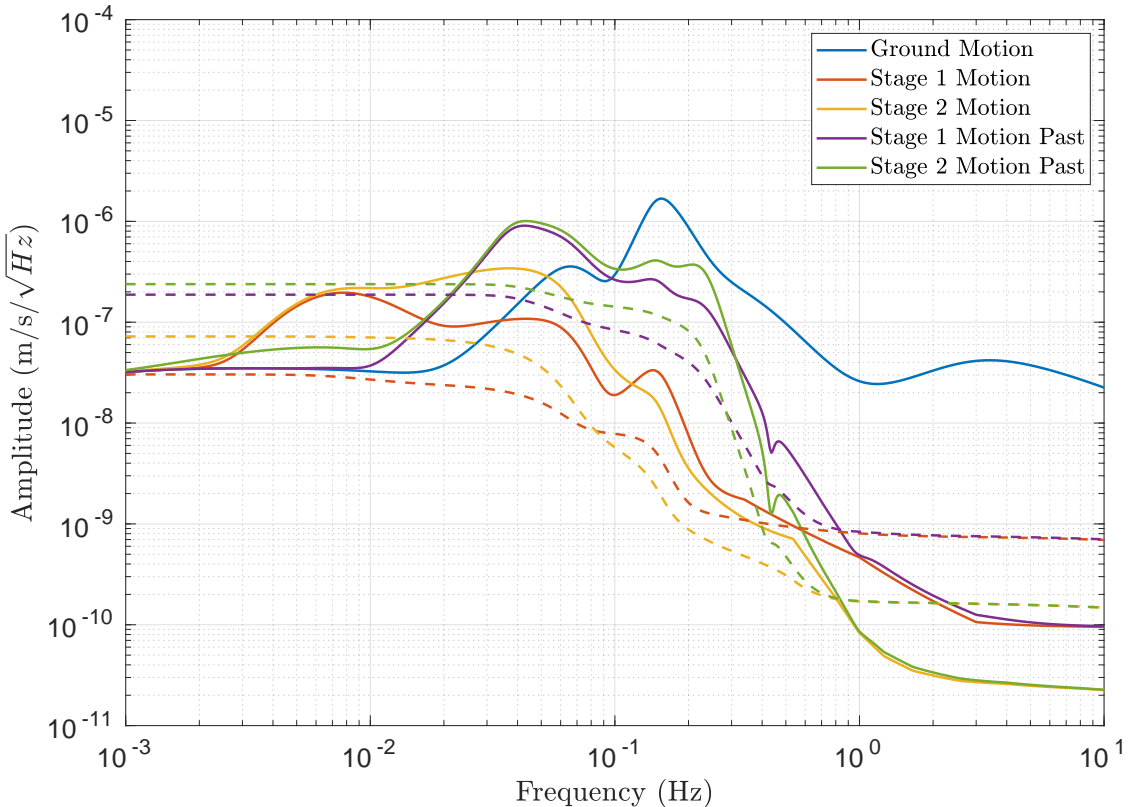
Figure 3.18: Comparison of the translational isolation performance during O2 and the projected performance with the inclusion of the cBRS. The dashed lines indicate the RMS of each curve.

The performance comparison of the translational isolation is shown in Figure 3.18. Above 1 Hz, the performance of the two schemes are similar as lowest noise sensors at those frequencies have not changed. At the secondary microseism, 100-500 mHz, the inclusion of the cBRS yields a factor of ~20 improvement of the residual motion while at the primary microseism, 50-100 mHz, it yields a factor of ~3. With the cBRS, the residual motion between 3-30 mHz is increased by a factor of ten. However, the RMS motion at those frequencies is still below

the previous performance. It is expected that the control loops downstream will be able to compensate for this increase in motion without any decrease in performance. Below 2 mHz, both schemes follow the ground since the the position sensors dominate at those frequencies.

Although in reality the control loop for each isolation platform will have to be tuned individually, these models show that one can expect a significant decrease in residual motion with the deployment of the cBRS.

3.3.2 Angular Control Performance
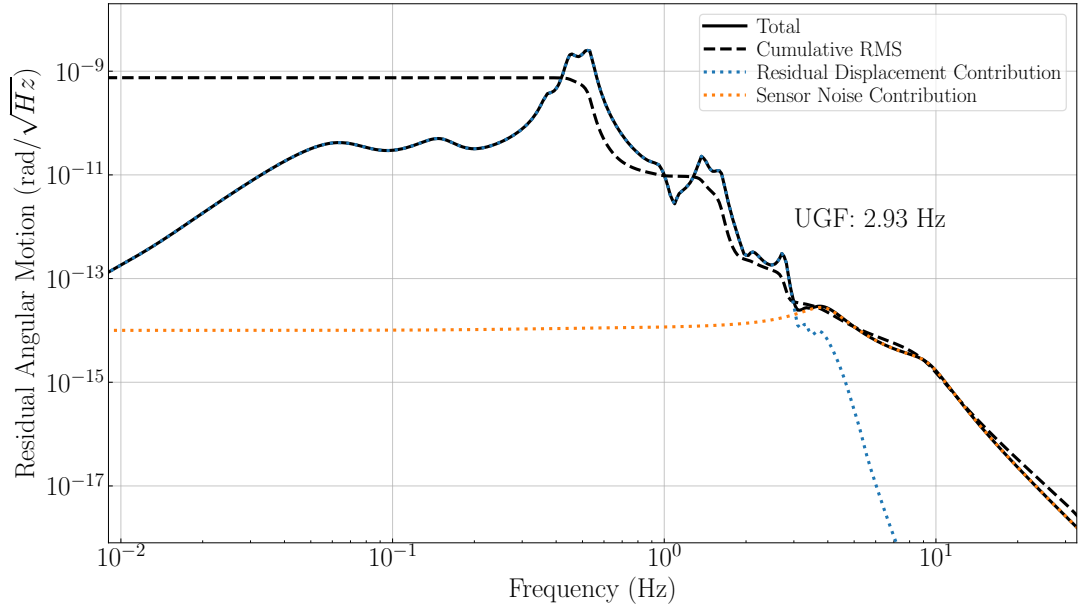
Figure 3.19: A model of the performance of the angular sensing and control system retuned for the the seismic isolation performance with the cBRS. This model optimizes the unity gain frequency (UGF) of the ASC loop to maximize performance above $\sim$10 Hz while maintaining the low frequency RMS at 1 nrad/$\sqrt{\text{Hz}}$.

As mentioned in Section 3.1, the improved seismic isolation provided by the cBRS allows one to retune the angular sensing and control (ASC) loops. In order to estimate the possible

ASC performance for a given seismic performance, a simplified model was constructed[3] [37] which takes the motion of the suspension point as an input, optimizes a theoretical control loop, and outputs the expected residual angular motion of the test mass. The control loop is optimized to give the best performance at high frequencies while maintaining a low frequency RMS residual of 1 nrad/$\sqrt{\text{Hz}}$.
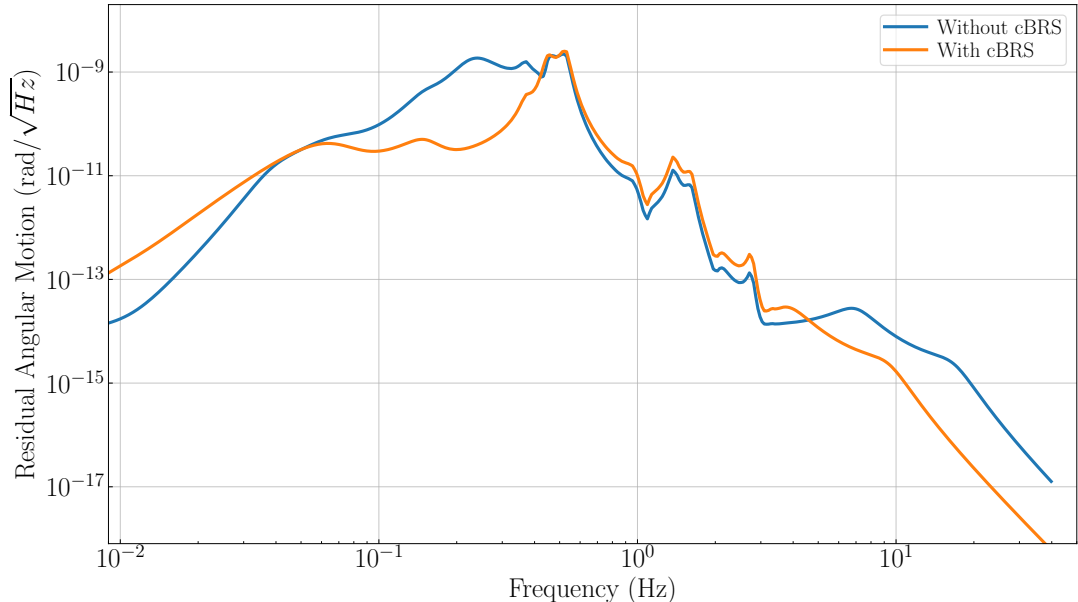
Figure 3.20: Comparison of the ASC performance with and without the cBRS. The decrease motion at ~30 mHz allows the UGF to be moved to from 5.23 Hz to 2.93 Hz. This shift decreases the rolled-off sensor noise that leaks into the GW band above 5 Hz.

This model used a handful of approximations that do not necessarily hold in reality. First off, it only modeled the performance of a single test mass. To predict the effect on the differential strain, all four test masses would need to be modeled. Additionally, it ignores the effects of radiation pressure which become important at high laser powers. [36] However, the

---

[3]Model originally developed by Hang Yu. [37]

limiting factor in the current observatories is believed to be the seismic isolation performance at low frequencies. Thus improvements due to increased seismic isolation are captured by this model.

The performance of the ASC system was modeled for the seismic performance with the cBRS installed, Figure 3.19, and without, Figure 3.1. In both situations, the high frequency performance is limited by sensor noise which leaks into the gravitational wave band. The primary retuning that can be made with the inclusion of the cBRS is a decrease in the ASC UGF from 5.23 Hz to 2.93 Hz. Above this the residual falls off as $1/f^5$.

Figure 3.20 compares the modeled residual for a system with and without the cBRS. As expected, adding the cBRS reduces the residual between ∼50-500 mHz due to the increased performance of the seismic isolation system. This allows a shift in the UGF to lower frequencies which reduces the residual above ∼5 Hz.
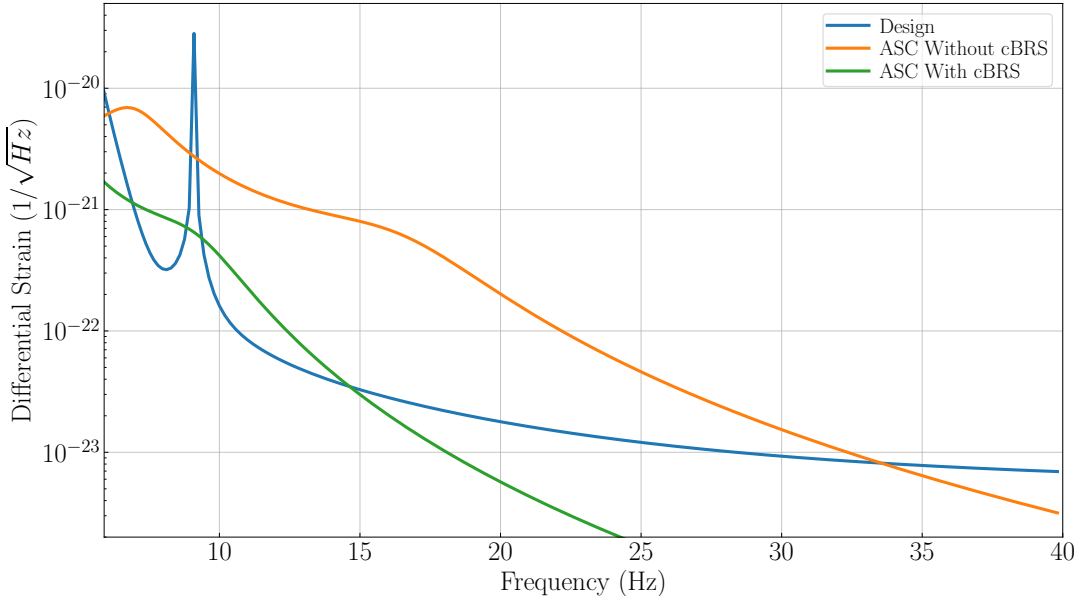
Figure 3.21: Projected low frequency strain noise with and without the cBRS along with aLIGO design sensitivity. [16]

This decrease in residual motion above $\sim$5 Hz would directly decrease noise in the differential strain readout of the observatory as shown in Figure 3.21. It should be stressed that for an accurate prediction of the strain noise, one would need to include the contributions from all four test masses and their couplings due to radiation pressure. However, this model suggests that with the future installation of the cBRS one would expect roughly an order of magnitude reduction in the low frequency noise in the gravitational wave channel bringing the noise closer to the aLIGO design sensitivity.

Chapter 4

AUXILIARY APPLICATIONS

With every novel sensor comes novel science. The development of the precision rotation sensors described in Chapters 2 and 3 has opened up a collection of novel scientific avenues.

4.1 Geophysics

Seismic waves have six components, three translations and three rotations. Seismology has long neglected the rotational components due the lack of sensitive rotation sensors. Recent developments, such as the advent of seismically relevant ring laser gyros [40], have alleviated this issue. The rotation sensors described in Chapter 2 and 3 join a small class of low-frequency ground-rotation sensors with low translational coupling. These attributes allow these sensors to be applied to seismology.

4.1.1 Rayleigh Wave Theory

Seismic waves can be broken into two classes: body waves and surface waves. Surface waves have two polarizations: Love waves and Rayleigh waves. The motion caused by a Love wave is constrained to the plane parallel with the surface of the medium while Rayleigh waves are constrained to a plane perpendicular to the surface.

The plane wave solution of a Rayleigh wave has six components $(u_x, u_y, u_z, \theta_x, \theta_y, \theta_z)$ where u_i designates the translational motion in the ith direction while θ_i is the rotation

about the ith axis. These can be described as with the following [41]

$$u_x(\mathbf{r}, t) = \alpha \sin(\zeta) \cos(\phi) \cos(\omega t - \mathbf{k} \cdot \mathbf{r}) \tag{4.1}$$

$$u_y(\mathbf{r}, t) = \alpha \sin(\zeta) \sin(\phi) \cos(\omega t - \mathbf{k} \cdot \mathbf{r}) \tag{4.2}$$

$$u_z(\mathbf{r}, t) = \alpha \cos(\zeta) \cos(\omega t - \mathbf{k} \cdot \mathbf{r} + \pi/2) \tag{4.3}$$

$$\theta_x(\mathbf{r}, t) = \frac{\partial u_z}{\partial y} = \alpha \kappa \cos(\zeta) \sin(\phi) \cos(\omega t - \mathbf{k} \cdot \mathbf{r}) \tag{4.4}$$

$$\theta_y(\mathbf{r}, t) = -\frac{\partial u_z}{\partial x} = -\alpha \kappa \cos(\zeta) \cos(\phi) \cos(\omega t - \mathbf{k} \cdot \mathbf{r}) \tag{4.5}$$

$$\theta_z(\mathbf{r}, t) = \frac{1}{2}\left(\frac{\partial u_y}{\partial x} - \frac{\partial u_x}{\partial y}\right) = 0 \tag{4.6}$$

where α is the amplitude, ζ is the ellipticity angle, ϕ is the angle of incidence in the horizontal plane, ω is the angular frequency, and $\mathbf{k} = \kappa(\cos(\phi), \sin(\phi), 0)$ is the wavevector.

These components can be seen in Figure 4.1 which shows measurements of the seismic waves sourced by a M 7.9 earthquake in Papua New Guinea as seen by instruments installed at the End-Y station of the LIGO Hanford Observatory (LHO). The translations were measured by a broadband three-axis seismometer while the rotation was sensed by a Beam Rotation Sensor (BRS), described in Chapter 2. As one would expect from Equations 4.3 and 4.4, the vertical velocity and the rotation differ only by a constant factor related to the phase velocity and the angle of incidence. Additionally, a large amplitude Love wave is apparent starting at ~1200 seconds which neither the vertical seismometer or the BRS experiences due to the waves' lack of vertical component.

From Equations 4.1-4.3 it can be seen that with only a traditional 3-axis seismometer, it is impossible to measure all five parameters that define the wave-field.[1] Additionally, the horizontal components, u_x and u_y can contain contributions from co-propagating Love waves which further muddles ones ability to extract parameters.

---

[1] With an array of vertical seismometer four parameters can be readily measured: frequency, angle of incidence, wavenumber, and amplitude.
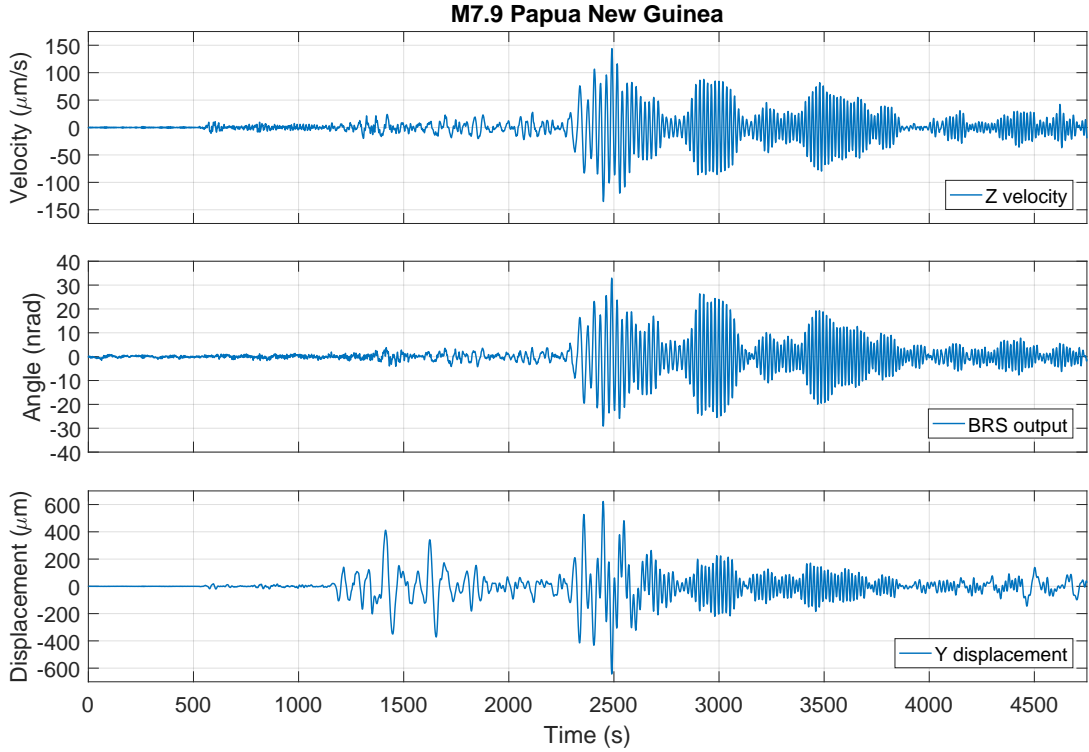
Figure 4.1: Observations of the seismic waves emanated from a M7.9 earthquake in Papua New Guinea as seen by instruments installed at the End-Y Station of LHO. Both the Z-velocity and Y-displacement were measured by a broadband three-axis seismometer while the rotation was measured by a BRS described in Chapter 2. Reprinted from [42].

4.1.2 Wave-Field Parameter Extraction

With the combined measurements of the translational and rotational components at a single station, one can extract wavefield parameters that would otherwise be difficult to obtain, namely the phase velocity and angle of incidence.

Seismic wave phase velocities are common observables which not only allow for understanding of Rayleigh wave propagation but can be inverted to yield tomographical structure profiles of the interior of the earth. [43] The traditional method of extracting these is by exploiting the time of arrival of a wave as it passes through an array of many seismometers. The analysis can be constrained to only the vertical channel as this axis is insensitive

to Love waves which could contaminate the measurements. However, this method requires many devices and effectively averages over the size of the array.

Alternatively, with measurements of the rotational components a point-like measurement of the phase velocity can be made with three devices, a 3-component seismometer and two horizontal rotation sensors. This can be shown in the following equations:

$$v \equiv \frac{\omega}{\kappa} = \frac{\dot{u}_z}{\theta_x} \sin(\phi) \tag{4.7}$$

$$v = \frac{\dot{u}_z}{\theta_y} \cos(\phi) \tag{4.8}$$

$$v = \frac{\dot{u}_z}{\sqrt{\theta_x^2 + \theta_y^2}} \tag{4.9}$$

where the dot represents the temporal derivative. Equations 4.7 and 4.8 can be utilized if a station has only one horizontal rotation sensor but requires independent determination of ϕ, the angle of incidence. In contrast, Equation 4.9 contains only information from a single station.

In addition to the phase velocity, the angle of incidence can be determined with the following:

$$\phi = \arctan\left(\frac{\theta_x}{\theta_y}\right) \tag{4.10}$$

Although in theory this can be measured using a single seismometer, Love wave contamination of the horizontal translational channels distort most measurements. As the horizontal rotational channels are insensitive to Love waves, they allow for the extraction of ϕ without such contamination.

4.1.3 Single Station Dispersion Measurements

As described in Section 2.3.1, two BRSs were installed at LHO, one at each end station located 5.66 meters apart. The End-X BRS was found to have a $\delta = 30$ μm leading to a

translational coupling of 2×10^{-4} rad/m while the End-Y BRS was found to have a coupling of 1×10^{-6} rad/m with a $\delta < 0.5~\mu$m. This limited any seismology studies to only the End-Y BRS as the End-X BRS was contaminated with translational motion.
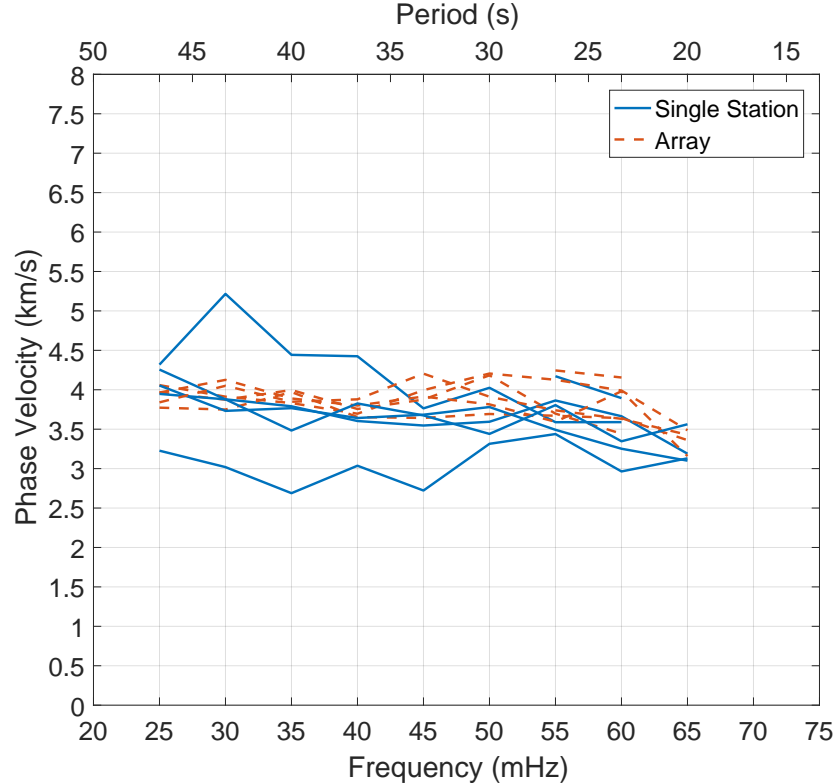
Figure 4.2: Rayleigh wave phase velocity measurements made by instruments located at the End-Y station of LHO and the same measurements achieved by the array of seismometers deployed at LHO. Each line represent the measurements achieved by different earthquakes. The angle of incidence of each wave was measured independent of the single station and used within the analysis. Reprinted from [42]

Between April, 2016 and January, 2017, six earthquakes were measured during environmentally quite times. [42] With application of Equation 4.7 the phase dispersion curve at the End-Y Station was measured with instruments installed at a single station. Corrections of the angle of incidence were determined by an array of seismometers installed at LHO and

were verified via great circle calculations. Additionally, the phase velocity was estimated in a more traditional manor using the signal delay between the array of seismometer at LHO. The measured phase dispersion curves are shown in Figure 4.2 which shows agreement between the two methods. For more detail see Reference [42]

These measurements display the utility of including rotation sensors in seismic instruments. If a seismic station was constructed with two orthogonally oriented horizontal rotation sensors and a vertical seismometer, the phase velocity could be measured independent of angle of incidence by utilizing Equation 4.9. Neglecting the logistical difficulty, one could imagine constructing arrays of station with both translational and rotational sensors. This array would allow mapping of the phase dispersion curves, and thus tomography, with spatial resolution limited only by the size of the instruments. Such stations could also be installed within traditional arrays to yield independent, point-like measurements to further constrain tomographic studies.

4.2 Newtonian Noise

4.2.1 Theory

The gravitational coupling between the environment and an interferometer's test masses, so called Newtonian noise, is expected to limit the performance of terrestrial gravitational wave observatories in the near future [44]. Sources of the gravitational field variations can range from atmospheric density changes to vibrations of the laboratory structures [45]. This coupling is unique in the fact that it can not be shielded or trivially engineered away. One can move an observatory underground to decrease the strength of the atmospherically driven fluctuations and those caused by seismic surface waves. However, this process is both expensive and does not remove the sources which come from operating an instrument such as the vibrations of the vacuum structure or seismic motion sourced by laboratory equipment.

For the current surface-level interferometric observatories, the seismic motion due to Rayleigh waves is thought to be the dominant contributor to the Newtonian noise and will

be the limiting noise source between 8-20 Hz [46]. The motion due to a plane Rayleigh wave follows:

$$u_z(\mathbf{r}, t) = u_z \cos(\omega t - \mathbf{k} \cdot \mathbf{r} + \pi/2) \tag{4.11}$$

where $u_z = \alpha \cos(\zeta)$, α is the amplitude, ζ is the ellipticity angle, ϕ is the angle of incidence in the horizontal plane, ω is the angular frequency, and $\mathbf{k} = \kappa(\cos(\phi), \sin(\phi), 0)$ is the wavevector. The corresponding test mass acceleration in the x-direction follows [47]:

$$a_x(\mathbf{r}, t) = 2\pi u_z \gamma G \rho_0 e^{-h\kappa} \cos(\phi) \cos(\omega t - \mathbf{k} \cdot \mathbf{r}) \tag{4.12}$$

where G is the gravitational constant, ρ_0 is the density of the ground, h is the height of the test mass from the ground, and $\gamma \approx 0.8$ is a factor which accounts for the counter-action of the change of density due to the seismic wave and the vertical motion of the ground.

At first glance, these equations appear to suggest that one could predict the test mass acceleration for a given vertical seismometer signal. Such a prediction would allow for high quality subtraction of the Newtonian Noise from an observatory's data stream. However, true seismic wave-fields are not composed of stationary Rayleigh waves but instead are comprised of the sum of many desperate sources which may change their amplitude and phase in time. With this consideration, the phase difference between Equations 4.11 and 4.12 and the lack of angle of incidence dependence in Equation 4.11 destroy the ability to use a single vertical seismometer as a reliable sensor for Newtonian noise subtraction.

On the other hand, a horizontal seismometer described by Equation 4.1 is both in-phase with the Newtonian noise signal and has the same angular dependence. However, seismic wave-fields also include Love waves which have horizontal components but not vertical. This contaminates the horizontal channels and thus decreases the correlation between the horizontal seismometer and the Newtonian noise.

Finally, the tilt, being the rotation about the y-axis, due to a Rayleigh wave is described

by the following:

$$\theta_y(\mathbf{r}, t) = \frac{\partial u_z}{\partial x} = u_z \kappa \cos(\phi) \cos(\omega t - \mathbf{k} \cdot \mathbf{r}) \qquad (4.13)$$

The tilt is both in-phase, has the same angular dependence, and does not include Love waves. The lack of Love waves can be seen in Figure 4.1 when the horizontal seismometer experiences a large Love wave at around 1200 s while the rotation sensor sees no such signal. The tilt signal and the Newtonian noise are thus related by a handful of parameters which can be measured independently or determined empirically and are not expected to vary in time. This points to the conclusion that a tiltmeter is the ideal sensor for Newtonian noise subtraction.

4.2.2 Observations

During LIGO's second observing run (O2), a prototype cBRS, described in Chapter 3, was installed at the corner station of the LIGO Hanford Observatory along with an array of vertical seismometers. The aim of this deployment was to investigate the Newtonian noise coupling and to test subtraction schemes. Ideally, one would place a rotation sensor directly below one of the test masses as the Newtonian noise acting on the mirror is dominated by the ground just beneath it. However, the cBRS was too large to be placed underneath the vacuum chamber which holds the test mass so it was placed next to the vacuum chamber as can be seen in Figure 4.3.

The first goal of this instrumentation deployment was to assess the ability to combine an array of vertical seismometers to significantly subtract Newtonian noise. Unfortunately, the observatory was not sensitive enough to observe Newtonian noise with high signal-to-noise. Thus the cBRS was used as a proxy for the signal that would be seen by a future observatory. A Weiner filter was constructed using seismometers as the references and the cBRS as the target. This combined the 30 seismometer signals to optimally approximate the cBRS signal.

The results of this subtraction can be seen in Figure 4.4 [48] which shows that a single
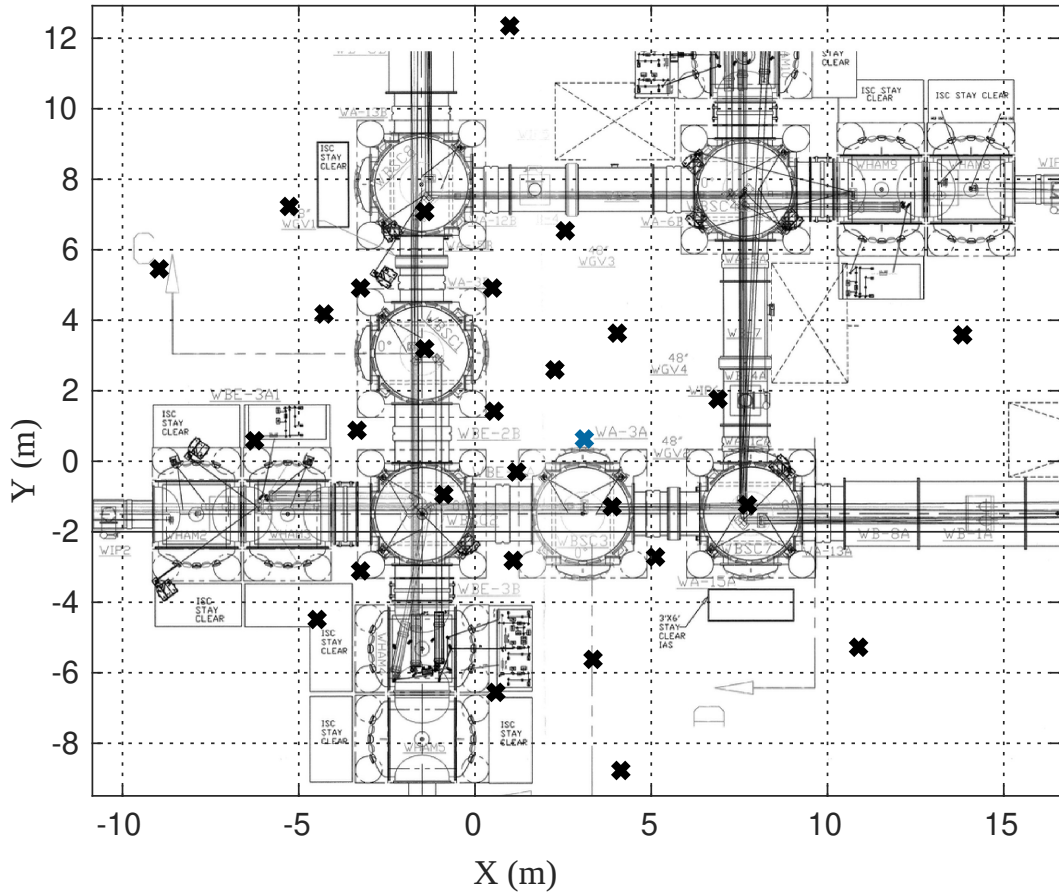
Figure 4.3: The location of the cBRS , marked by the blue ×, during O2 alongside the array of seismometers, marked by the black ×s, overlaid on a schematic of the LHO corner station vacuum chambers. Adapted from [48].
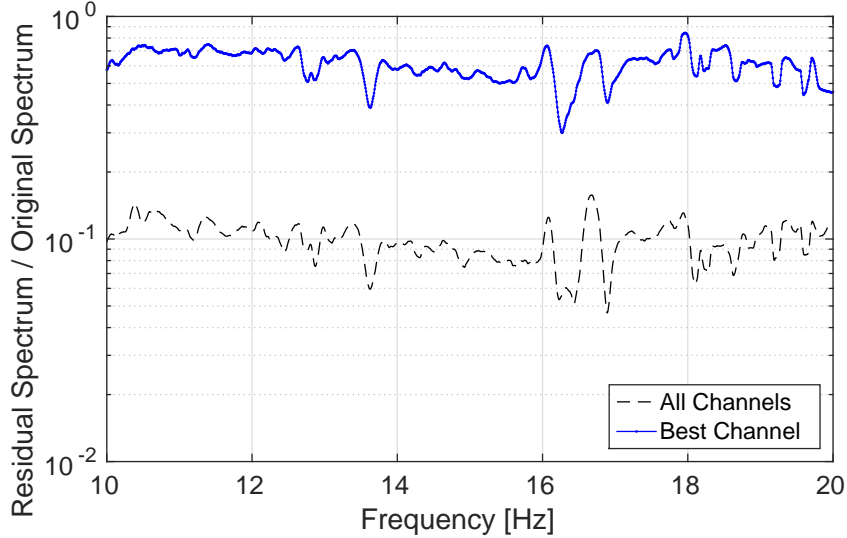
Figure 4.4: Projected Newtonian noise subtraction with the array of seismometers using the cBRS as a proxy for the noise that would be seen by a future observatory. Reprinted from [48].

seismometer can achieve a factor of ∼1.5 reduction while the combination of all 30 seismometers achieves a reduction of ∼10. This can be understood with Equations 4.11-4.13. The signal from a single vertical seismometer will not have the same angular dependence or phase as the tilt. However, the collection of seismometers can simulate the tilt by combining pairs of seismometers to act as effective rotation sensors.

These observations have shown that an array of 30 vertical seismometers can be expected to yield Newtonian noise reduction for future observatories of at least an order of magnitude. Indeed, similar subtraction was achieved when only the best five seismometers were included as reference channels. [48] This points to the possibility of smaller well placed arrays also achieving similar reduction.

The second goal of this array was to investigate the coupling between ground tilt and strain for the observatory during O2. This was achieved by calculating the transfer function between the cBRS output and strain using a month of data. The resultant transfer function

is shown in Figure 4.5 where it is apparent coupling is observed across many frequencies with a single-to-noise of ∼10-30. The noise was estimated by recalculating the transfer function with the two data streams shifted relative to one another by 1000 seconds.
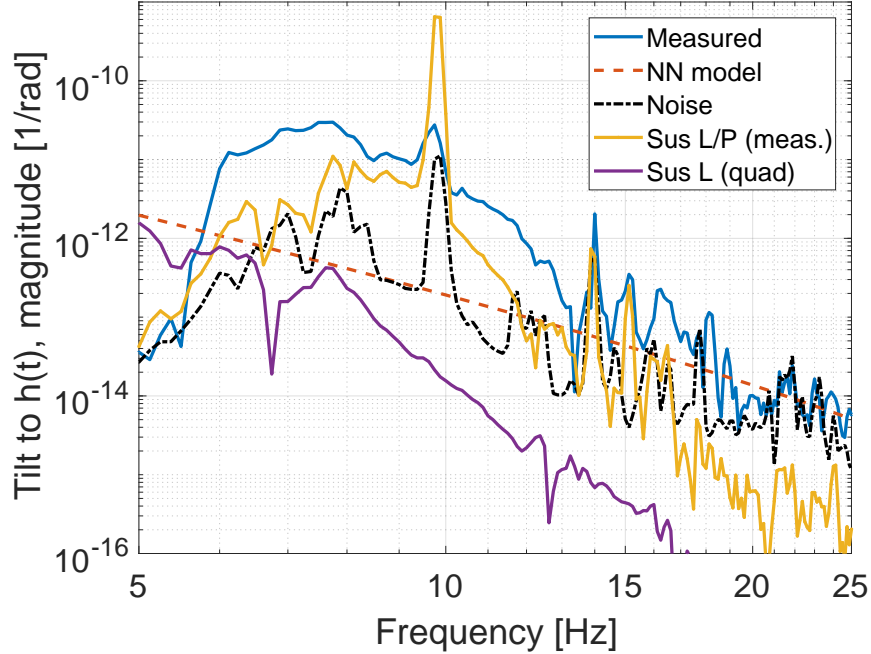
Figure 4.5: Transfer function between the cBRS and the strain output of the interferometer alongside various non-gravitational coupling mechanisms and a model for the Newtonian noise caused by an isotropic, homogeneous Rayleigh wave-field. Reprinted from [48].

This coupling can not be known to be of gravitational nature a piori. Thus a collection of possible non-gravitational coupling mechanisms were investigated. [48] Namely, seismic coupling through the seismic isolation system. This path follows from ground tilt to suspension point motion which propagates to the test mass. The transfer function from the ground tilt to suspension point motion can be readily measured using the sensors on the isolation platforms. This was then propagated to test mass motion using an analytical model of the suspension, Sus L, and a previously measured transfer function from suspension point to test mass, Sus L/P, which includes both the length and pitch couplings.

These first observations pointed to the possibility that the current observatories are already being affected by Newtonian noise. However, further modeling and investigation [46] found that the distinction between gravitational and non-gravitational coupling is still ambiguous. Deployment of future instruments, including a rotation sensor designed specifically to observe Newtonian noise, should disentangle these couplings and may allow for the first subtraction of Newtonian noise from strain output of the interferometer.

BIBLIOGRAPHY

[1] Albert Einstein. The foundation of the general theory of relativity. *Annalen Phys.*, 354:769–822, 1916.

[2] Michele Maggiore. *Gravitational waves: Volume 1: Theory and experiments*, volume 1. Oxford university press, 2008.

[3] The LIGO Scientific Collaboration and the Virgo Collaboration, B.P. Abbott, et al. Observation of gravitational waves from a binary black hole merger. *Phys. Rev. Lett.*, 116:061102, Feb 2016.

[4] A. Einstein and N. Rosen. On gravitational waves. *Journal of the Franklin Institute*, 223(1):43 – 54, 1937.

[5] The LIGO Scientific Collaboration and the Virgo Collaboration, B. P. Abbott, et al. Tests of general relativity with the binary black hole signals from the LIGO-Virgo catalog GWTC-1. *Phys. Rev. D*, 100:104036, Nov 2019.

[6] The LIGO Scientific Collaboration and the Virgo Collaboration, R. Abbott, et al. GW190412: Observation of a Binary-Black-Hole Coalescence with Asymmetric Masses, 2020.

[7] J. M. Weisberg and Y. Huang. Relativistic measurements from timing the binary pulsar PSR B1913+16. *The Astrophysical Journal*, 829(1):55, Sep 2016.

[8] The LIGO Scientific Collaboration and the Virgo Collaboration, B.P. Abbott, et al. GW170817: Observation of gravitational waves from a binary neutron star inspiral. *Phys. Rev. Lett.*, 119:161101, Oct 2017.

[9] The LIGO Scientific Collaboration and the Virgo Collaboration, B.P. Abbott, et al. GW190425: Observation of a Compact Binary Coalescence with Total Mass $\sim 3.4 M_\odot$. *arXiv preprint arXiv:2001.01761*, 2020.

[10] The LIGO Scientific Collaboration and the Virgo Collaboration, B.P. Abbott, et al. GWTC-1: A gravitational-wave transient catalog of compact binary mergers observed by LIGO and Virgo during the first and second observing runs. *Phys. Rev. X*, 9:031040, Sep 2019.

[11] Bernd Brügmann. Fundamentals of numerical relativity for gravitational wave sources. *Science*, 361(6400):366–371, 2018.

[12] The LIGO Scientific Collaboration and the Virgo Collaboration, B. P. Abbott, et al. All-sky search for continuous gravitational waves from isolated neutron stars using advanced LIGO O2 data. *Phys. Rev. D*, 100:024004, Jul 2019.

[13] The LIGO Scientific Collaboration and the Virgo Collaboration and BP Abbott. An optically targeted search for gravitational waves emitted by core-collapse supernovae during the first and second observing runs of advanced LIGO and advanced Virgo. *arXiv preprint arXiv:1908.03584*, 2019.

[14] Thibault Damour and Alexander Vilenkin. Gravitational radiation from cosmic (super)strings: Bursts, stochastic background, and observational windows. *Phys. Rev. D*, 71:063510, Mar 2005.

[15] Richard Easther and Eugene A Lim. Stochastic gravitational wave production after inflation. *Journal of Cosmology and Astroparticle Physics*, 2006(04):010–010, Apr 2006.

[16] The LIGO Scientific Collaboration, J. Aasi, et al. Advanced LIGO. *Classical and Quantum Gravity*, 32(7):074001, Mar 2015.

[17] D. V. Martynov et al. Sensitivity of the advanced ligo detectors at the beginning of gravitational wave astronomy. *Phys. Rev. D*, 93:112004, Jun 2016.

[18] The LIGO Scientific Collaboration and the Virgo Collaboration, R. Abbott, et al. Open data from the first and second observing runs of advanced LIGO and advanced Virgo, 2019.

[19] F Acernese et al. Advanced Virgo: a second-generation interferometric gravitational wave detector. *Classical and Quantum Gravity*, 32(2):024001, Dec 2014.

[20] C Affeldt, K Danzmann, K L Dooley, H Grote, M Hewitson, S Hild, J Hough, J Leong, H Lück, M Prijatelj, S Rowan, A Rüdiger, R Schilling, R Schnabel, E Schreiber, B Sorazu, K A Strain, H Vahlbruch, B Willke, W Winkler, and H Wittel. Advanced techniques in GEO 600. *Classical and Quantum Gravity*, 31(22):224002, Nov 2014.

[21] M. Tse et al. Quantum-enhanced advanced ligo detectors in the era of gravitational-wave astronomy. *Phys. Rev. Lett.*, 123:231107, Dec 2019.

[22] LIGO-Virgo Cumulative Event/Candidate Rate Plot O1-O3: https://dcc.ligo.org/LIGO-G1901322/public.

[23] The LIGO Scientific Collaboration and the Virgo Collaboration, B.P. Abbott, et al. GW170817: Measurements of neutron star radii and equation of state. *Physical review letters*, 121(16):161101, 2018.

[24] Darach Watson, Camilla J Hansen, Jonatan Selsing, Andreas Koch, Daniele B Malesani, Anja C Andersen, Johan PU Fynbo, Almudena Arcones, Andreas Bauswein, Stefano Covino, et al. Identification of strontium in the merger of two neutron stars. *Nature*, 574(7779):497–500, 2019.

[25] LIGO Scientific Collaboration, Virgo Collaboration, 1M2H Collaboration, Dark Energy Camera GW-EM Collaboration, DES Collaboration, DLT40 Collaboration, Las Cumbres Observatory Collaboration, VINROUGE Collaboration, MASTER Collaboration, et al. A gravitational-wave standard siren measurement of the Hubble constant. *Nature*, 551(7678):85–88, 2017.

[26] The LIGO Scientific Collaboration and the Virgo Collaboration, BP Abbott, et al. A gravitational-wave measurement of the Hubble constant following the second observing run of Advanced LIGO and Virgo. *arXiv preprint arXiv:1908.06060*, 2019.

[27] The LIGO Scientific Collaboration and the Virgo Collaboration, B. P. Abbott, et al. Gravitational waves and gamma-rays from a binary neutron star merger: GW170817 and GRB170817a. *The Astrophysical Journal*, 848(2):L13, Oct 2017.

[28] Robert K. Cessaro. Sources of primary and secondary microseisms. *Bulletin of the Seismological Society of America*, 84(1):142–148, 02 1994.

[29] F. Matichard et al. Seismic isolation of advanced LIGO: Review of strategy, instrumentation and performance. *Classical and Quantum Gravity*, 32(18):185003, 2015© IOP Publishing. Reproduced with permission. All rights reserved.

[30] Fabrice Matichard and Matthew Evans. Tilt-free low-noise seismometry. *Bulletin of the seismological society of America*, 105(2A):497–510, 2015.

[31] Krishna Venkateswara, Michael P Ross, Jim Warner, Conor Mow-Lowry, Brian Lantz, Jeffrey Kissel, Hugh Radkins, Thomas Shaffer, Richard Mittleman, Sam Cooper, et al. Towards windproofing LIGO: Reducing the effect of wind-driven floor tilt by using rotation sensors in active seismic isolation. *arXiv preprint arXiv:2003.06447*, 2020.

[32] Krishna Venkateswara, Charles A. Hagedorn, Matthew D. Turner, Trevor Arp, and Jens H. Gundlach. A high-precision mechanical absolute-rotation sensor. *Review of Scientific Instruments*, 85(1), 2014.

[33] T B Arp, C A Hagedorn, Stephan Schlamminger, and J H Gundlach. A reference-beam autocollimator with nanoradian sensitivity from mHz to kHz and dynamic range of 10^7. *The Review of scientific instruments*, 84:095007, 09 2013.

[34] www.github.com/mpross/brsreadout.

[35] Peter R. Saulson. Thermal noise in mechanical experiments. *Phys. Rev. D*, 42:2437–2445, Oct 1990.

[36] L Barsotti, M Evans, and P Fritschel. Alignment sensing and control in advanced LIGO. *Classical and Quantum Gravity*, 27(8):084026, Apr 2010.

[37] Hang Yu. personal communication, Nov 2019.

[38] C M Mow-Lowry and D Martynov. A 6D interferometric inertial isolation system. *Classical and Quantum Gravity*, 36(24):245006, Nov 2019.

[39] S J Cooper, C J Collins, A C Green, D Hoyland, C C Speake, A Freise, and C M Mow-Lowry. A compact, large-range interferometer for precision measurement and inertial sensing. *Classical and Quantum Gravity*, 35(9):095007, Mar 2018.

[40] Simonelli et. al. First deep underground observation of rotational signals from an earthquake at teleseismic distance using a large ring laser gyroscope. *arXiv*, 2016.

[41] Stefano Maranó and Donat Fäh. Processing of translational and rotational motions of surface waves: Performance analysis and applications to single sensor and to array measurements. *Geophysical Journal International*, 196:317–339, 2014.

[42] M. P. Ross, K. Venkateswara, C. A. Hagedorn, J. H. Gundlach, J. S. Kissel, J. Warner, H. Radkins, T. J. Shaffer, M. W. Coughlin, and P. Bodin. Low-Frequency Tilt Seismology with a Precision Ground-Rotation Sensor. *Seismological Research Letters*, 89(1):67–76, 11 2017.

[43] Jordyn C. Babikoff and Colleen A. Dalton. Long-period rayleigh wave phase velocity tomography using usarray. *Geochemistry, Geophysics, Geosystems*, 20(4):1990–2006, 2019.

[44] Peter R. Saulson. Terrestrial gravitational noise on a gravitational wave antenna. *Phys. Rev. D*, 30:732–736, Aug 1984.

[45] Jan Harms. Terrestrial gravity fluctuations. *Living reviews in relativity*, 18(1):3, 2015.

[46] J. Harms, E. L. Bonilla, M. W. Coughlin, J. Driggers, S. E. Dwyer, D. J. McManus, M. P. Ross, B. J. J. Slagmolen, and K. Venkateswara. Observation of a potential future sensitivity limitation from ground motion at ligo hanford. *Phys. Rev. D*, 101:102002, May 2020.

[47] Jan Harms and Krishna Venkateswara. Newtonian-noise cancellation in large-scale interferometric GW detectors using seismic tiltmeters. *Classical and Quantum Gravity*, 33(23):234001, Oct 2016.

[48] M. W. Coughlin, J. Harms, J. Driggers, D. J. McManus, N. Mukund, M. P. Ross, B. J. J. Slagmolen, and K. Venkateswara. Implications of dedicated seismometer measurements on newtonian-noise cancellation for advanced LIGO. *Phys. Rev. Lett.*, 121:221104, Nov 2018.

[49] Katherine L Dooley, Lisa Barsotti, Rana X Adhikari, Matthew Evans, Tobin T Fricke, Peter Fritschel, Valera Frolov, Keita Kawabe, and Nicolás Smith-Lefebvre. Angular control of optical cavities in a radiation-pressure-dominated regime: the enhanced LIGO case. *JOSA A*, 30(12):2618–2626, 2013.

[50] W. H. K Lee, M. Celebi, M. I. Todorovska, and H. Igel. Introduction to the special issue on rotational seismology and engineering applications. *Bulletin of the Seismological Society of America*, 99(2B):945–957, 2009.

[51] Chin-Jen Lin, Han-Pang Huang, Nguyen Dinh Pham, Chun-Chi Liu, Wu-Cheng Chi, and William H. K. Lee. Rotational motions for teleseismic surface waves. *Geophysical Research Letters*, 38(15), 2011. L15301.

[52] M. Reinwald, M. Bernauer, H. Igel, and S. Donner. Improved finite-source inversion through joint measurements of rotational and translational ground motions: a numerical study. *Solid Earth*, 7(5):1467–1477, 2016.

[53] A. Pancha, T. H. Webb, G. E. Stedman, D. P. McLeod, and K. U. Schreiber. Ring laser detection of rotations from teleseismic waves. *Geophysical Research Letters*, 27(21):3553–3556, 2000.

[54] Jacopo Belfi, Nicolò Beverini, Giorgio Carelli, Angela Di Virgilio, Enrico Maccioni, Gilberto Saccorotti, Fabio Stefani, and Alexander Velikoseltsev. Horizontal rotation signals detected by "G-Pisa" ring laser for the Mw = 9.0, march 2011, japan earthquake. *Journal of Seismology*, 16(4):767–776, 2012.

[55] Krishna Venkateswara, Charles A. Hagedorn, Jens H. Gundlach, Jeffery Kissel, Jim Warner, Hugh Radkins, Thomas Shaffer, Brian Lantz, Richard Mittleman, Fabrice Matichard, and Robert Schofield. Subtracting tilt from a horizontal seismometer using a ground rotation sensor. *Bulletin of the Seismological Society of America*, 107(2):709–717, 2017.

[56] Brian Lantz, R Schofield, B. O'Reilly, D. E. Clark, and D DeBra. Review: Requirements for a ground rotation sensor to improve advanced LIGO. *Bulletin of the Seismological Society of America*, 99(2B):980–989, 2009.

[57] Norman A Haskell. The dispersion of surface waves on multilayered media. *Bulletin of the Seismological Society of America*, 43(1):17–34, 1953.

[58] Fan-Chi Lin, Morgan P. Moschetti, and Michael H. Ritzwoller. Surface wave tomography of the western united states from ambient seismic noise: Rayleigh and love wave phase velocity maps. *Geophysical Journal International*, 173(1):281, 2008.

[59] T. Meier, K. Dietrich, B. Stöckhert, and H.P. Harjes. One-dimensional models of shear wave velocity for the eastern mediterranean obtained from the inversion of rayleigh wave phase velocities and tectonic implications. *Geophysical Journal International*, 156(1):45–58, 1 2004.

[60] Cédric P. Legendre, Li Zhao, Win-Gee Huang, and Bor-Shouh Huang. Anisotropic rayleigh-wave phase velocities beneath northern vietnam. *Earth, Planets and Space*, 67(1):28, 2015.

[61] Rainer Weiss. Electromagnetically coupled broadband gravitational antenna. In *K.S. Thorne, "Gravitational radiation", 300 Years of Gravitation, S W Hawking and W Israel, pp 330–458*. University Press, 1972.